

POLITECNICO DI TORINO

Corso di Laurea Magistrale in Ingegneria Meccanica

Tesi di Laurea Magistrale

**Study of the Behaviour of AHSS in Forming Design  
Phase with the aim of Predicting and Reducing the  
Springback Defects**



**Relatore**

Prof. Ing. Raffaella Sesana

**Correlatore**

Roberto Maiorano

**Candidato**

Davide Nastasi

Matricola: 264536

ANNO ACCADEMICO 2020/2021



## ABSTRACT

Sheet metal forming is widely used in many applications but, among others, it is mainly utilized in the automotive and aerospace industries. It is a very popular manufacturing technique due to the high precision, mass production and short processing time that can be provided in production line.

In the last decade, to improve crash worthiness and fuel economy, the automotive industry is increasingly, using Advanced High Strength Steel (AHSS) and aluminum alloys. The main reason to utilize AHSS is their better performance in crash energy management.

However, the improved capabilities these engineered AHSS bring to the automotive industry accentuate forming problems already existing in normal mild steels. These concerns including higher loads on presses and tools, greater energy requirements, and increased need for springback compensation and control. In fact, springback is one of the leading roadblocks hindering auto stamping productivity.

This paper aims at presenting the origin of springback, providing fundamentals, terms, and definitions to deeply understand the phenomenon and to characterize what causes it; to elaborate ways to rectify the springback angles by characterizing the material in FE simulations and by implementing compensation techniques in real stamping operations.



## ACKNOWLEDGMENTS

First and foremost, I would like to show my appreciation to my supervisor, Prof. Ing. Raffaella Sesana for always being available to clarify any questions arose during this work. Thank you for your guidance, transmitted knowledge, inspiration, and for all the valuable advices on academic and professional matters.

It was a true pleasure have worked under your supervision.

I would like to thank my advisor Roberto Maiorano for the welcome in the company and for giving me the opportunity to undertake this research study and to persevere and complete it satisfactorily. Thanks also to Grazio e Marco for the continuous support received during all the practical work and experimental tests carried out, together with all the members of Costat S.r.l.

To all the Professors of the Mechanical Engineering Department of Politecnico di Torino for their contribution in my academic education.

A special note of heartfelt gratitude to all my family who always supported me during my entire academic career and whose love and guidance are with me in whatever I pursue.

Finally, to my colleagues and friends, whose companionship and support was crucial during these past five years.



# TABLE OF CONTENTS

ABSTRACT.....	2
ACKNOWLEDGMENTS.....	4
CHAPTER 1: INTRODUCTION .....	8
1.1 Motivation.....	8
1.2 Thesis Outline.....	10
1.3 Material Property Definitions .....	11
1.4 Springback.....	18
1.5 Rectifying Springback .....	24
1.6 Fundamentals of Bending .....	25
CHAPTER 2: LITERATURE REVIEW – AHSS .....	29
2.1 Advanced High Strength Steel.....	29
2.2 Metallurgy of AHSS.....	31
2.3 Applications of AHSS .....	40
CHAPTER 3: DETERMINATION OF MATERIAL PROPERTIES AND FORMABILITY .....	42
3.1 Tensile Test.....	42
3.2 Cyclic Loading-Unloading Tensile Test .....	44
3.3 Biaxial Bulge Test.....	46
3.4 Combined – Tensile and Bulge Test – Method.....	47
3.5 Formability and Drawability .....	48
3.6 Tension-Compression Test .....	50
CHAPTER 4: CONSTITUTIVE MODELS .....	53
4.1 AutoForm Forming Solver .....	54
4.2 Fundamentals of Constitutive Models .....	60
4.3 Hardening Curve available in AutoForm .....	65
4.4 Yield Surface available in AutoForm.....	68
4.5 Forming Limit Curve available in AutoForm.....	75
CHAPTER 5: EXPERIMENTAL ACTIVITY – MATERIAL CHARACTERIZATION OF DUAL PHASE 1000	77
5.1 Material Composition.....	77
5.2 Uniaxial Tensile Test.....	77
5.3 Cyclic Loading-Unloading Tensile Test .....	82
5.4 Nakajima Test.....	84
5.4 Tension - Compression Test .....	88
CHAPTER 6: EXPERIMENTAL ACTIVITY – FEA OF U-SHAPED BEND TEST ON DUAL PHASE 1000	92

6.1	CAD Design by CATIA V5.....	93
6.2	Simulation Setup and Evaluation of Forming Process.....	96
6.3	Simulation Results of Different Constitutive Models.....	97
6.4	Simulation Results considering Young’s Modulus Reduction. ....	105
6.5	Simulation Results with Post Stretching Method (Lock Beads) .....	108
CHAPTER 7: CASE STUDY OF A JOB ORDER IN DUAL PHASE 1000 .....		120
7.1	Simulation Forming Process .....	122
7.2	Analysis Results .....	124
References.....		132

# CHAPTER 1:

## INTRODUCTION

### 1.1 Motivation

Sheet metal forming is a manufacturing process used to make a wide range of products, such as door panels, structural beams, and hoods. It is most popular for the manifold technical feasibilities in manufacturing, high precision, mass production, and short processing time. Thus, large number of companies, especially the automotive companies, are interested in the developments of this industry.

Over the last decade, the Advanced High Strength Steels (AHSS) and high strength aluminum alloys are increasingly used in automotive industry to satisfy the demands for improved safety, stricter fuel efficiency standards and lower emissions. Replacing the conventional steel components with AHSS can help to achieve the earlier mentioned goals by reducing the structural weight of the automotive body. Higher strength of the material makes use of thinner sheets possible while increasing the crashworthiness. In general, the formability of high strength steels and aluminum alloys is lower than milder grade steel. In addition, springback and die wear is more severe in forming high strength materials since the forming stresses and contact pressure is higher. GEN3 materials are the latest class of steels to be developed by the steel industry.

Figure 1 illustrates general information about the strength and formability of sheet materials used in automotive industry.

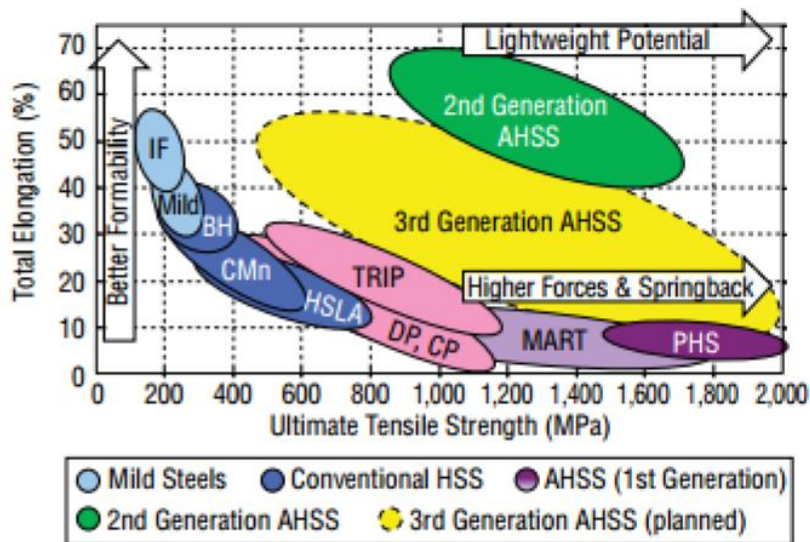


Figure 1: Types of Advanced High Strength Steels (AHSS) (16)

Among all potential defects which can affect the part geometry, springback affects most the dimensional accuracy and the final shape of stamped parts. Thus, it is very important improve the accuracy of springback prediction to reduce the die development time and cost for springback compensation.

Springback occurs after stamping and ejection of the part because the state of the stresses and strains in the deformed material has changed. Nowadays, numerical simulation of springback prediction through finite element methods is helping the die makers to reduce the extensive trial-and-error method for final die modification. Several parameters affect the prediction of springback. In general, accuracy of springback calculation depends on the accuracy of stress distribution prediction in the part. (1) (2) (3)

Furthermore, springback is affected by a combination of several factors such as material properties, tool geometry, process parameters and geometry of the blank.

## 1.2 Thesis Outline

The thesis is made up of 7 chapters so hereafter discussed. Chapter 1 provides a general introduction which explains the motivation that led to study the behaviour of AHSS, and the main problems related to the manufacturing of these materials. Chapter 2 reports a literature review of AHSS including the main designations and covering the range of application of these materials. Chapter 3 explains the available experimental tests to fully characterize a material for setting up a detailed constitutive model. Chapter 4 defines and explains the fundamentals of constitutive models that are present in literature and describes the three main sections of AutoForm forming solver illustrating for each one the equations and the available models. After providing an overview of the knowledge needed to study these AHSS, Chapter 5, 6, and 7 validate the constitutive models to reduce the springback defect in Dual Phase 1000 material with sheet thickness 1.2 mm after having conducted a series of experimental tests. Particularly, different constitutive yield surface models will be analysed, the influence of the Young's modulus reduction will be discussed, and a post stretch method will be implemented to reduce and solve the springback defect. A proof of the effectiveness of these concepts is also applied in a study case of a job order with the successful result in reducing the springback and saving money for the company.

### 1.3 Material Property Definitions

Accurate determination of material properties (i.e., the flow stress data,  $E$ -modulus, and uniform elongation etc.) is crucial for designing the sheet forming process. This section provides the definitions required to define the properties of sheet metals, bending and springback.

#### Stiffness and $E$ -modulus

Stiffness ([N/m] or [Nm/rad]) is defined as the resistance of a component to elastic deformation. It depends on the component shape, loading conditions and elastic modulus. If referring to the specific properties of the material, the parameters describing the resistance to elastic deformation are the  $E$ -modulus (or elastic modulus [MPa]) and the shear elastic modulus ([MPa]), obtained experimentally by the slope of the elastic portion of the stress-strain curve for a material. The  $E$ -modulus decreases with increasing plastic strain. (4)

#### Strength

The maximum strength of a material is experimentally obtained by Ultimate Tensile Strength where flow stress (as obtained from tensile test) is maximum. Plastic flow or deformation occurs due to movement of dislocations present in the crystal structures. Impeding the movement of dislocations increases the strength and decreases ductility. Different mechanisms such as solid solution strengthening (alloying), mechanical working (strain hardening), dispersion and precipitation

hardening, etc. are used to increase the strength of metals. (5)

### **Yield strength**

The value of stress at the point on the engineering stress-strain curve at which the plastic deformation begins. For some materials, the yield point is not clearly defined. In such cases a line parallel to the linear elastic region is drawn at an offset of 0.2% strain. The yield strength is defined as the stress value corresponding to the point of intersection of this line with the stress-strain curve.

### **Elastic-plastic properties of materials**

The flow stress or true stress-strain curve for a material reflects the elastic-plastic properties of a material. This curve is one of the most important variables for calculating input data for finite element (FE) and analytical methods used to predict metal flow and defects. (6)

### **Necking, Uniform Elongation and Formability**

In a tensile test, necking is the localization of strains which occurs towards the end of the test. At this stage, strains and stresses are no longer uniform over the length of measurement or gage length. Formability is the limit of uniform elongation after which necking begins.

Figure 2 shows the main parameters that are possible to calculate from a uniaxial tensile test.

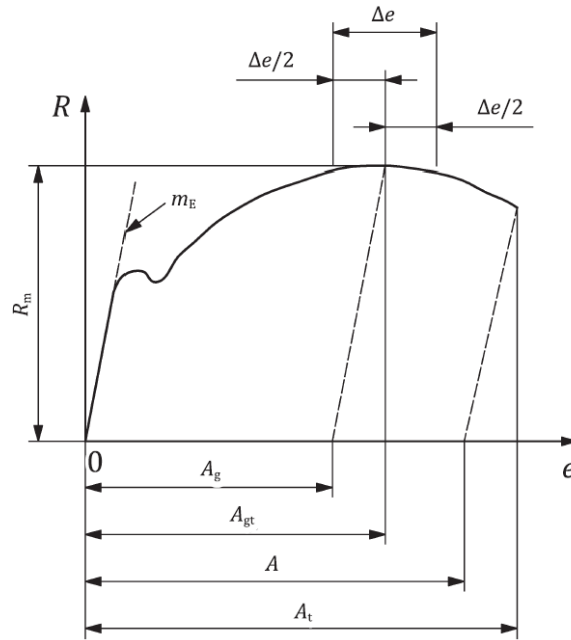


Figure 2: Schematic definition of extension.

$A$	Percentage elongation after fracture
$A_g$	Percentage plastic extension at maximum force
$A_{gt}$	Percentage total extension at maximum force
$A_t$	Percentage total extension at maximum fracture
$e$	Percentage extension
$m_E$	Slope of the elastic part of the stress-percentage extension curve
$R$	Stress
$R_m$	Tensile strength
$\Delta e$	Plateau extent

Table 1: Uniaxial tension test notation

## Hardening rules

As the material is loaded beyond the yield point, it deforms plastically, and it is often essential to predict the behaviour of plastic deformation. Its yield surface changes in size, shape, and position. The variation of yield surface with plastic deformation is given by hardening rules. Various models were developed for evaluating the influence of strain hardening and other factors of deformation.

The different types of models are:

1. Linear elastic model (Figure a.)
2. Ideal rigid plastic material model (Figure b.)
3. Elastic – perfectly plastic model (Figure c.)
4. Hardening material models under monotonic loading (minimal fluctuations)
5. Hardening models under cyclic loading

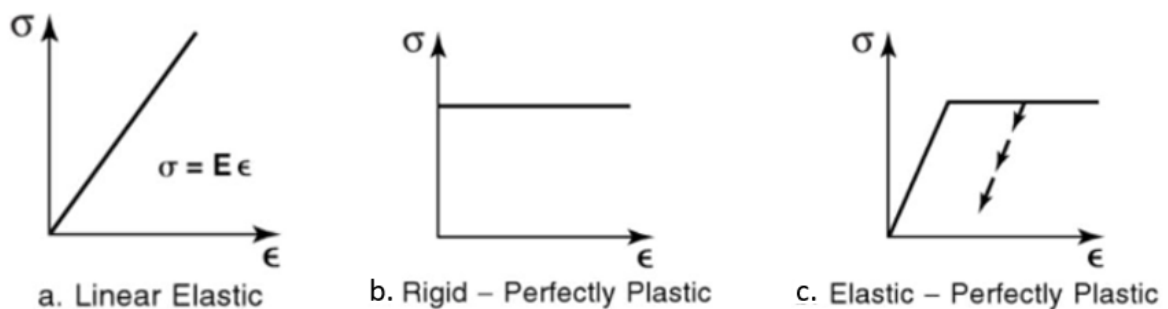


Figure 3: Schematic of basic hardening models

### Linear Elastic Model

The material behaviour in the first stage of deformation is approximately elastic. i.e., the material returns to its initial stage after the external cause (force) is removed.

The perfectly elastic material which significantly obeys Hooke's law follows the law  $\sigma = E\varepsilon$ . Brittle materials like glass, ceramics and some other cast irons can be modelled with this model. They have short rupture elongation (up to 2%) and go to rupture immediately after yield point is reached. This model is only suitable where the deformation is within the elastic deformation and is not suitable for sheet metal forming in which plastic deformation is essentially bringing permanent deformation.

## **Rigid Plastic Model**

The deformation should at least partially permanent. For metals, this pattern of permanent deformation is known as plasticity. A rigidly plastic material does not have any elastic nature of deformation and it is rigid up to yield point. Once the applied stress reaches the yield limit, the material is subjected to 100% plastic deformation and this deformation continues further without any increment of the stress applied. In this rigidly plastic material model the specimen exhibits no deformation until the applied stress reaches the critical value i.e., the yield point. As soon as the applied stress in the specimen reaches the yield limit the deformation takes place uninterruptedly as long as the applied stress is maintained at yield stress. If the stress lessened due to unloading the deformation ceases.

## **Elastic – Perfectly Plastic Model**

An elastic – perfectly plastic material model is one which considers the elastic nature of the material and does not account for strain hardening of the material. While using this model, the stress increment is linear until the yield point, and beyond the yield point the material offers no resistance to deformation as well as no strain hardening of the material and hence uninterrupted deformation takes place as long as the stress applied is maintained at yield point. Perfectly elasto–plastic material can yield a constant stress state that exhibits no hardening and essentially the yield surface remains constant.

Hardening material models under monotonic loading (minimal fluctuations) are:

- a. Rigid linear hardening model
- b. Elastic linear hardening model
- c. Ludwig power law

### **Rigid Linear Hardening Model**

In such a material deformation is not observed until tensile stress reaches to yield point. When tensile stress reaches the yield point, plastic deformation starts, and to increase deformation the stress should increase as well. In this model stress varies linearly with plastic strain (linear work hardening). As in rigid perfectly plastic model elastic deformation is neglected in this model. This model is applied to plastic bending analysis of beams.

### **Elastic Linear Hardening Model**

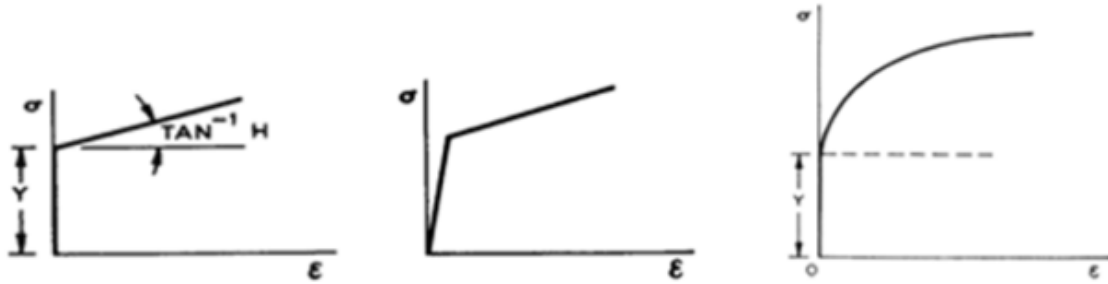
This model shows elastic linear hardening behaviour.

### **Ludwig Power Law**

Some empirical equations that fit to the experimentally obtained true stress-true strain curves have been developed. One of them is developed by Ludwig and valid in constant temperature and strain rate situations.

$$\sigma = Y + H\varepsilon^n$$

Where  $Y$ : Yield strength,  $H$ : Material dependent strength coefficient,  $n$ : Work hardening power.



(a) Rigid linear hardening model    (b) Elastic linear hardening model    (c) Ludvig power law

Figure 4: Hardening material models under monotonic loading

### Swift Law

The work hardening law recommended by Swift depicted by the following relation  $\bar{\sigma} = A(B + \bar{\epsilon})^n$  where  $B$ : pre - strain coefficient,  $n$ : work hardening power,  $A$ : coefficient function of direction of stress.

In the operations where the large deformations take place the Swift law yields results closer to the real deformation process. However, the Swift law is more complex than other models. The effective stress:  $\bar{\sigma}$  is a vector made of three components  $(\sigma_x, \sigma_y, \sigma_z)$  as the effective strain:  $\bar{\epsilon}$   $(\epsilon_x, \epsilon_y, \epsilon_z)$ .

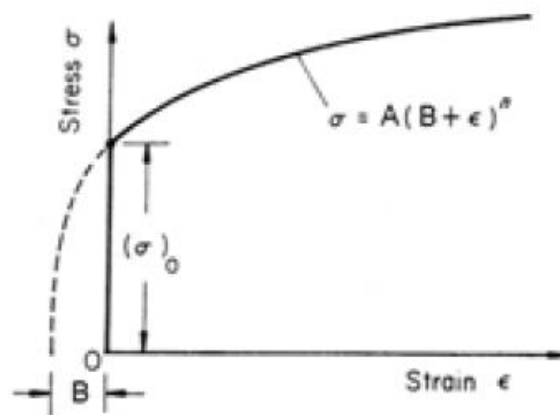


Figure 5: Swift law

Hardening models under cyclic loading are:

- a) Isotropic hardening model
- b) Kinematic hardening model
- c) Mixed hardening model

Hardening models under cyclic loading conditions will be extensively discussed in the next section as they are the most adequate to predict material behaviour in stamping operations and since they are used for computational simulation. (7)

## 1.4 Springback

Springback is generally defined as the elastic recovery of material after unloading and tools removals. It is stress driven and therefore becomes more critical in forming high strength materials. High strength materials experience higher springback than traditional steels under the same forming conditions (10).

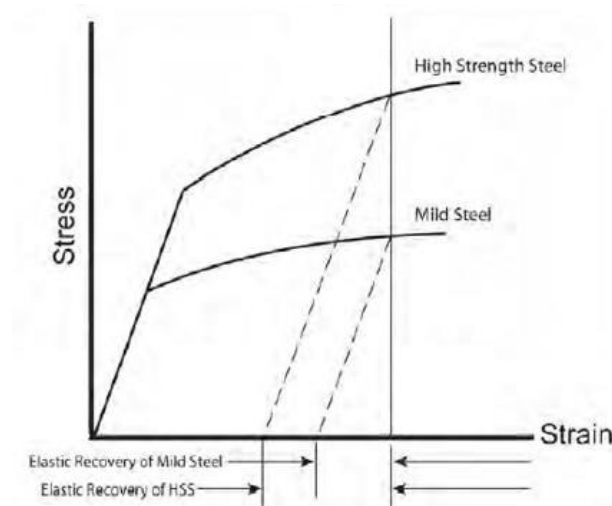


Figure 6: Schematic showing amount of springback is proportional to stress. (11)

Indeed, the elastic recovery of AHSS is different from the elastic recovery of HSLA (High Strength Low Alloy) steels. Figure 7 very well illustrates the difference in springback defect for the two distinct materials, DP350/600 and HSLA 350/450. The two samples were formed to have the same geometry. Hence both samples were subjected to identical strain distribution. However, the stress distribution was very different because of the steel property differences between the materials.



Figure 7: Comparison of two channels obtained with different materials, made sequentially in the same die.

The magnitude of springback is governed by the tooling and component geometry. When part geometry prevents complete unloading (relaxing) of the elastic stresses, the elastic stresses remaining in the part are called residual stresses. The part then will assume whatever shape it can to minimize the total remaining residual stresses. If all elastic stresses cannot be relieved, then creating a uniformly distributed residual stress pattern across the sheet and through the thickness will help eliminating or at least to reduced springback problems. (11)

### **Types of Springback**

Three modes of springback commonly found in channels and under body

components are: Angular change, Sidewall curl, and Twist.

### Angular change

Angular change sometimes called springback, is the angle created when the bending edge line (the part) deviates from the line of the tool (ideal geometry),

Figure 8. If there is no sidewall curl, the angle is constant up the wall of the channel.

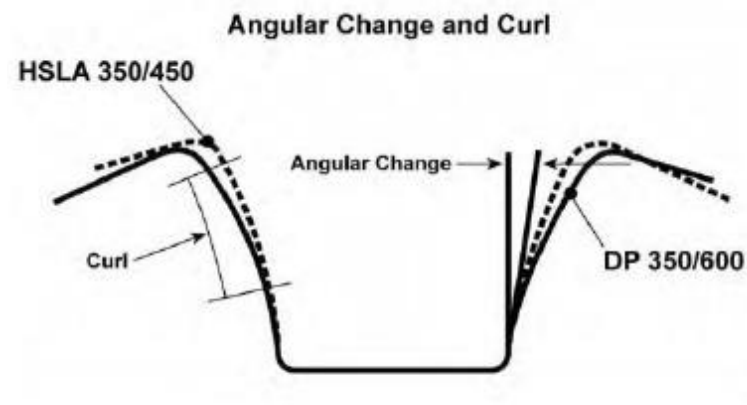


Figure 8: Schematic showing difference between angular change and sidewall curl.

Angular change is caused by stress difference in the sheet thickness direction when a sheet metal bends over a die radius. This stress difference in the sheet thickness direction creates a bending moment at the bending radius after dies are released, which results in the angular change. The key to eliminating or minimizing the angular change is to eliminate or minimize this bending moment.

### Sidewall curl

Side wall curl is the curvature created in the side wall of a channel, Figure 8. This curvature occurs when a sheet of metal is drawn over a die/punch radius or through

a draw bead. The primary cause is uneven stress distribution or stress gradient through the thickness of the sheet metal. This stress is generated during the bending and unbending process.

During the bending and unbending sequence, the deformation histories for both sides of the sheet are unlikely to be identical. This usually manifests itself by flaring the flanges, which is an important area for joining to other parts. The resulting sidewall curl can cause assembly difficulties for rail or channel sections that require tight tolerance of mating faces during assembly. In the worst case, a gap resulting from the sidewall curl can be so large that welding is not possible.

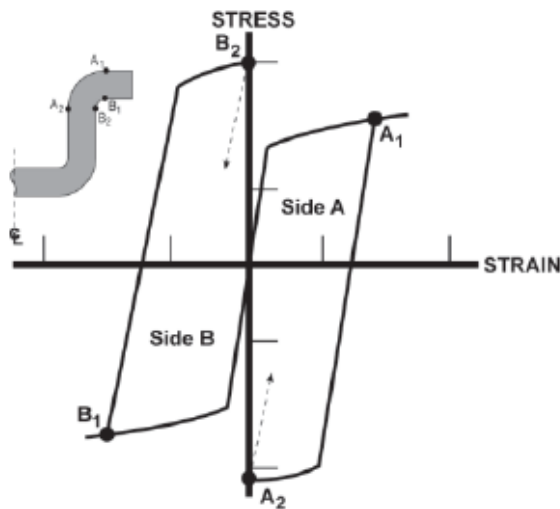


Figure 9: Origin and mechanism of sidewall curl.

Figure 9 illustrates in detail what happens when sheet metal is drawn over the die radius (bending and unbending process). The deformation in the side A changes from tension (A1) during bending to compression (A2) during unbending; in contrast, the deformation in the side B changes from compression (B1) to tension (B2) during bending and unbending.

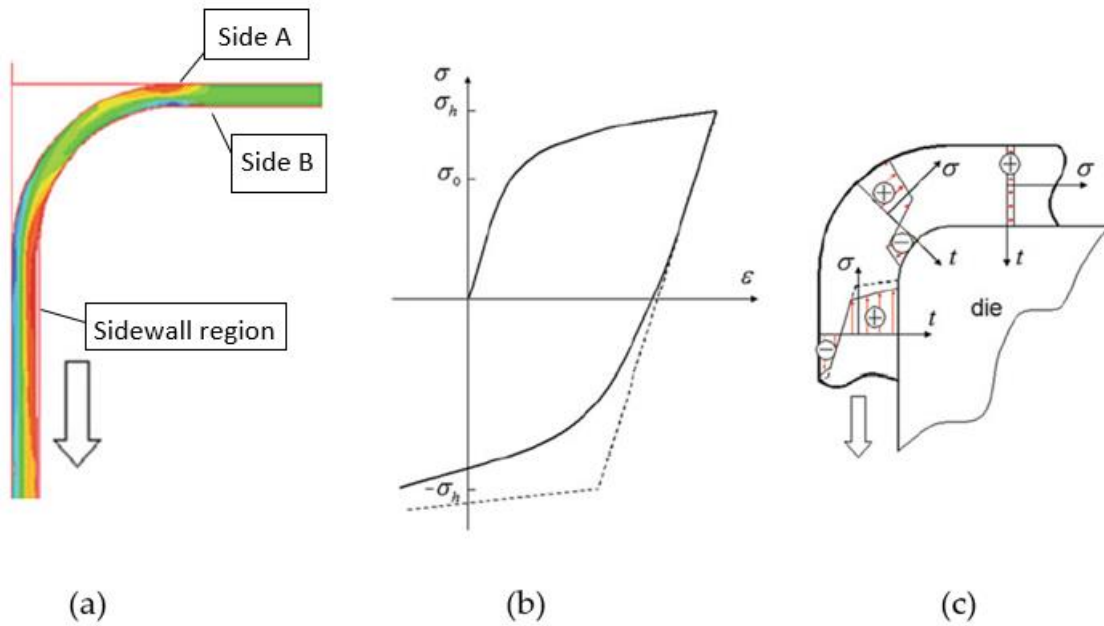


Figure 10: (a) reversal tension/compression loading (red for the tension stress) during passing over a tool radius, arrow shows the direction of drawing. (b) schematic of the Bauschinger effect and (c) Bauschinger influence on the stress evolution during passing.

By referring to Figure 10(a), as the sheet enters the sidewall region, side A is in compression and side B is in tension, although both sides may have similar amounts of strain. Once the punch is removed from the die cavity (unloading), side A tends to elongate in the flange region and side B to contract due to elastic recovery causing a curl angle in the sidewall of the part.

This difference in elastic recovery in the side A and side B is the main source of variation in sidewall curl along the wall. The higher the strength of the deformed metal, the greater the magnitude and difference in elastic recovery between sides A and sides B and the increase in sidewall curl. The strength of the deformed metal depends not only on the yield strength, but also on the work hardening capacity. This is one of the key differences between conventional HSS and AHSS.

Clearly, the rule for minimizing the sidewall curl is to minimize the stress gradient through the sheet thickness.

## Twist

Twist is defined as two cross-sections rotating differently along their axis. Twist is caused by torsion moments in the cross-section of the part. The torsional displacement (twist) develops because of unbalanced springback and residual stresses acting in the part to create a force couple, which tends to rotate one end of the part relative to another. As shown in Figure 11 the torsional moment can come from the in-plane residual stresses in the flange, the sidewall, or both.

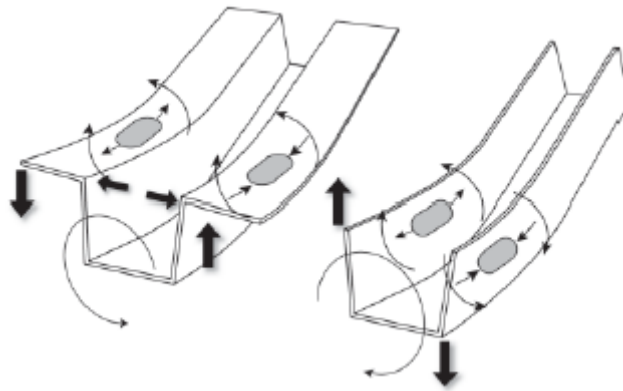


Figure 11: Torsion moment created flange or sidewall residual stresses.

The actual magnitude of twist in a part will be determined by the relationship between unbalanced stresses on the part and the stiffness of the part in the direction of the twist. Parts that are long and thin with low torsional stiffness values experiences higher tendencies to twist. Also, unsymmetrical parts which have unequal flange lengths or non-symmetric cut outs or sudden changes in cross section are more likely to experience unbalanced springback forces generated by

these non-symmetrical features. The tendency for parts to twist can be overcome by reducing the imbalance in the residual stresses forming the force couple that creates the torsional movement. (11).

## **1.5 Rectifying Springback**

Forming of a part creates elastic stresses unless the forming is performed at a higher temperature range where stress relief is accomplished before the part leaves the die. An example of the latter condition is HF (Hot Formed) steels. However, in CF (Cold Forming), some form of springback correction is required for bringing the part back to part print. This springback correction can take many forms.

The first approach is to apply an additional process that changes undesirable elastic stresses to less damaging elastic stresses. One example is a post-stretch operation that reduces sidewall curl by changing the tensile-compressive elastic stress gradient through the thickness of the sidewall to all tensile elastic stresses throughout the thickness. A second approach is to modify the process and/or tooling to reduce the level of elastic stresses imparted to the part during the forming operation. An example would be to reduce sidewall curl by replacing sheet metal flowing through draw beads and over a die radius with a simple 90 degree bending (11).

## 1.6 Fundamentals of Bending

Bending operation defined as a sheet forming operation to produce angled parts, is widely used in sheet metal forming where parts require simple or complex bent profile. A sheet material is bent by an imposed moment, by stretching over a cylindrical form, or by combination of both moment and tension.

In bending of a sheet material, area around the bending radius experiences simultaneous tension-compression loading state, Figure 12.

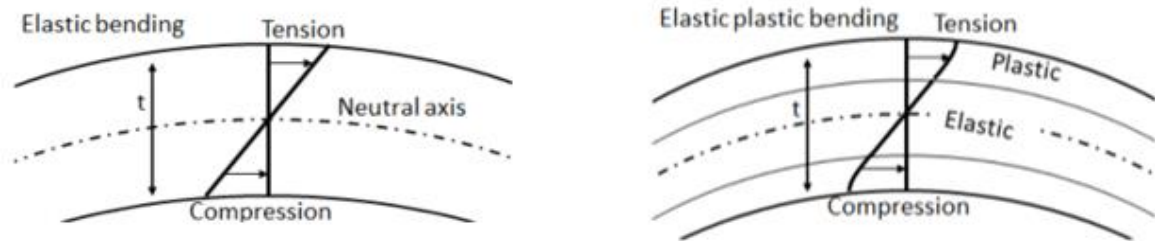


Figure 12: Stress distribution in bending theory.

In plane strain bending, a nonlinear strain distribution across the sheet thickness is introduced as (8):

$$\varepsilon_X^{true} = \ln \frac{r}{R_n} = \ln \left( 1 \pm \frac{y}{R_n} \right)$$

Where  $R_n$  is the radius of the neutral axis and  $y$  is the distance from the neutral axis.

The amount of the stresses developed on the sheet during the forming process determines whether the area is in pure elastic or elastoplastic strain state, Figure 12.

Under plane strain conditions, using Hooke's law, **the elastic component** can be calculated as:

$$\sigma_x = \frac{E}{(1-\nu^2)} \varepsilon_x = \frac{E}{(1-\nu^2)} \frac{y}{R_n}$$

Where  $E$  is Young's modulus and  $\nu$  is Poisson's ratio. At low strains, i.e., in elastic region, the differences between the engineering stress/strain and the true stress/strain are negligible.

**The stress component for plastic deformation** depends on the complexity of the material hardening model. The effective stress:  $\bar{\sigma}$  is a vector made of three components ( $\sigma_x, \sigma_y, \sigma_z$ ) as the effective strain:  $\bar{\varepsilon}$  ( $\varepsilon_x, \varepsilon_y, \varepsilon_z$ ).

The strain hardening is described by Swift's equation:

$$\bar{\sigma} = K(\varepsilon_0 + \bar{\varepsilon})^n$$

where  $\varepsilon_0$  is the pre-strain coefficient,  $n$  is the work hardening power,  $K$  is a coefficient function of direction of stress.

The plastic yielding behaviour of normal anisotropic materials is defined by Hill's non-quadratic yield criterion (38). For plane-strain deformation, this criterion has the form:

$$\bar{\varepsilon} = F \varepsilon_1 = F \varepsilon_x$$

where  $F$  is an index to account for anisotropy and the strain/stress state, given by

$$F = 1 \quad \text{isotropy and uniaxial stress}$$

$$F = 2/\sqrt{3} \quad \text{isotropy and plane strain}$$

$$F = \frac{1+R}{\sqrt{1+2R}} \quad \text{normal anisotropy and plane strain (37)}$$

Where  $R$  is the normal (transverse) anisotropy

$$R = \frac{r_0 + r_{90} + 2r_{45}}{4}$$

Thus,  $\sigma_x = F\bar{\sigma}$  the bending stress can be described as:

$$\sigma_x = F\bar{\sigma} = FK(\varepsilon_0 + \bar{\varepsilon})^n = FK(\varepsilon_0 + F\varepsilon_x)^n = KF^{n+1}\left[\frac{\varepsilon_0 - \varepsilon_0^e}{F} + \varepsilon_x\right]^n$$

For elastoplastic bending, the internal bending moment for a bending element includes the elastic moment ( $M_e$ ) in the elastic core, and the plastic moment ( $M_p$ ) in the plastic zone of the sheet. The integration of the bending stresses through the sheet thickness provides the internal bending moment per width. This bending moment can be calculated as:

$$M = M_e + M_p = \int_0^t \sigma_x y dy$$

$$M_e = \int_{-\varepsilon_e}^{\varepsilon_e} \sigma_x y dy$$

$$M_p = \int_{\varepsilon_{min}}^{-\varepsilon_e} \sigma_x y dy + \int_{\varepsilon_e}^{\varepsilon_{max}} \sigma_x y dy$$

Based on the classic elastic bending theory, the unloading moment can be expressed as:

$$M = \left(\frac{1}{r} - \frac{1}{r'}\right) E'I$$

The product  $E'I$  describes the stiffness of the bent sheet.

Where  $E' = E/(1 - \nu^2)$  is the plane strain modulus,  $I$  is the second moment of area about the middle axis ( $I = \frac{wt^3}{12}$ ),  $r$  and  $r'$  are the radius of curvature of the sheet metal before and after springback.

If it is assumed that the unloading moment has the same magnitude but opposite sign to the applied bending moment, the change in curvature due to springback is:

$$\left(\frac{1}{r} - \frac{1}{r'}\right) = \frac{M_{unloading}}{E'I} = \frac{12(1 - \nu^2)}{wt^3 E} (M_e + M_p)$$

Substituting equation into the above relations, the springback is a function of material properties, sheet thickness, bend radius, and the stress-strain state at the part. It should be noted that all the equations above, correspond to specific sections of the sheet. Therefore, the total springback is calculated as the summation of all the incremental springback angles of each individual section. (9)

## **CHAPTER 2:**

### **LITERATURE REVIEW – AHSS**

As referred to the introduction, the increasing requirements for passenger safety and fuel consumption have made the automotive industry to look for lighter and stronger materials such as Advanced High Strength Steels.

#### **2.1 Advanced High Strength Steel**

AHSS are complex, sophisticated materials, with carefully selected chemical compositions and multiphase microstructures resulting from precisely controlled heating and cooling processes. Various strengthening mechanisms are employed to achieve a range of strength, ductility, toughness, and fatigue properties.

The AHSS family includes Dual Phase (DP), Complex-Phase (CP), Ferritic-Bainitic (FB), Martensitic (MS), Transformation-Induced Plasticity (TRIP), Hot-Formed (HF), and Twinning-Induced Plasticity (TWIP). These 1st and 2nd Generation AHSS grades are uniquely qualified to meet the functional performance demands of certain parts. For example, DP and TRIP steels are excellent in the crash zones of the car for their high energy absorption. For structural elements of the passenger compartment, extremely high-strength steels, such as Martensitic and boron-based Press Hardened Steels (PHS) result in improved safety performance. (12)

Recently there has been increased funding and research for the development of the “3rd Generation” of AHSS. These are steels with special alloying and thermo-

mechanical processing to achieve improved strength-ductility combinations compared to present grades, with potential for more efficient joining capabilities, at lower costs. The broad range of properties is best illustrated by the famous Steel Strength Ductility Diagram, captured in Figure 13.

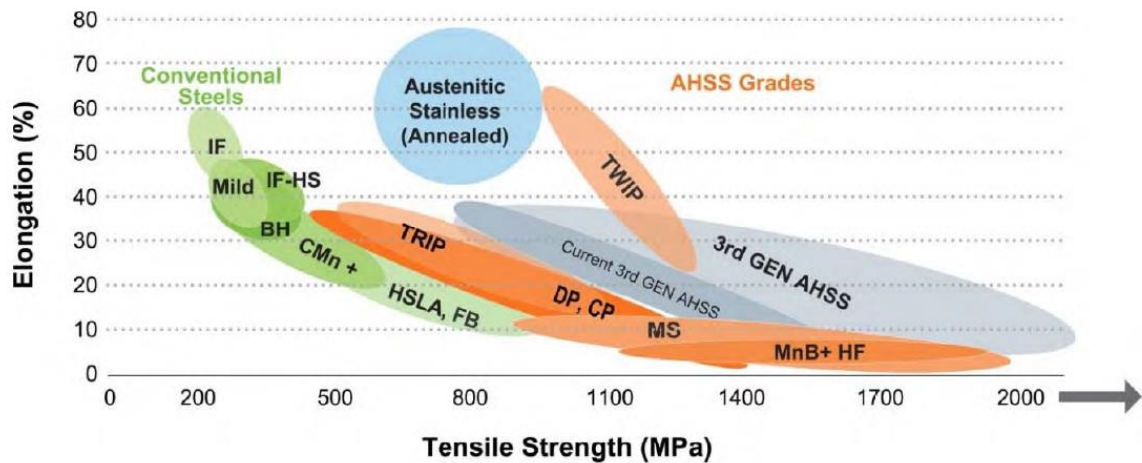


Figure 13: Steel Strength Ductility Diagram, illustrating the range of properties. (12)

Advanced high-strength steel (AHSS) grades contain significant alloying and two or more phases. The multiple phases provide increased strength and ductility not attainable with single-phase steels, such as high strength low alloy (HSLA) grades. HSLA materials achieve their strength through alloying and solid solution hardening, whereas AHSS are produced by using specific alloys and precise thermomechanical processing. Austenitic Stainless Steel have excellent strength combined with excellent ductility, and thus meet many vehicle functional requirements. Third Generation AHSS seeks to offer comparable or improved capabilities at significantly lower cost.

These various steel product families are shown in Table 2, in accordance with this

nomenclature.

<b>XX</b>	<b>Type of steel</b>	<b>XX</b>	<b>Type of steel</b>
HSLA	High Strength Low Alloy	TRIP	Transformation Induced Plasticity
DP	Dual Phase	MS	Martensitic (MART)
CP	Complex Phase	TWIP	Twinning-Induced Plasticity
FB	Ferritic Bainitic	HF	Hot Formed (and quenched)
Q&P	Quenching & Partitioning	TPN	Three Phase Nano-Precipitation

Table 2: Steel type designations

## 2.2 Metallurgy of AHSS

Automotive steels can be classified in several different ways. One is a metallurgical designation providing some process information. Common designations include low-strength steels (interstitial-free and mild steels); conventional high-strength steel, or HSS, such as bake hardenable and high-strength low-alloy steels (HSLA); and advanced high-strength steels, or AHSS (for example, dual phase and transformation-induced plasticity steels). Additional higher strength steels for the automotive market include hot-formed, post forming heat-treated steels, and steels designed for unique applications that have improved edge stretch and stretch bending characteristics.

### Dual Phase (DP) Steel

The Dual-Phase term is referred to AHSS steel grades that are composed by two distinct phases. The DP steels microstructure is based on a soft ferrite matrix filled with martensite islands (typically from 10 to 40 percent). Increasing the volume fraction of hard second phases generally increase the strength. This type of microstructure allows the steel to hold a UTS between 500 and 1200 MPa. (13)

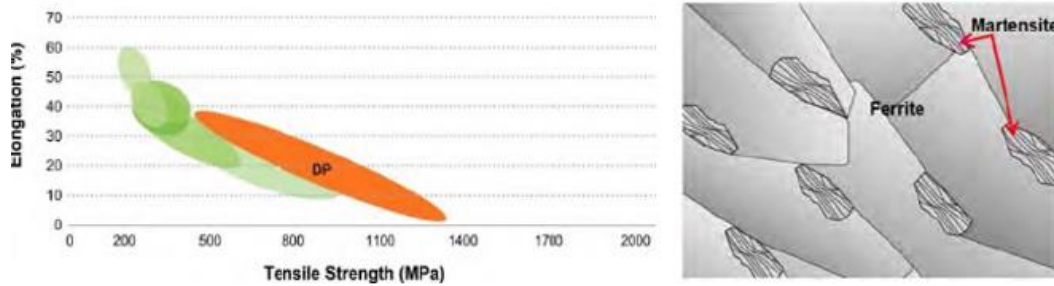


Figure 14: Schematic shows islands of martensite in a matrix of ferrite. (12)

Using the two phases, one can obtain a good balance between high strength and ductility. The martensitic phase is responsible for the material strength, due to the martensite islands acting as an obstacle to the material dislocations (during deformation). The martensitic phase can also be an important factor when it comes to the material durability since the martensite islands can delay a possible crack propagation. The ferritic phase isolates the martensitic islands, being responsible for the material ductility and formability (14).

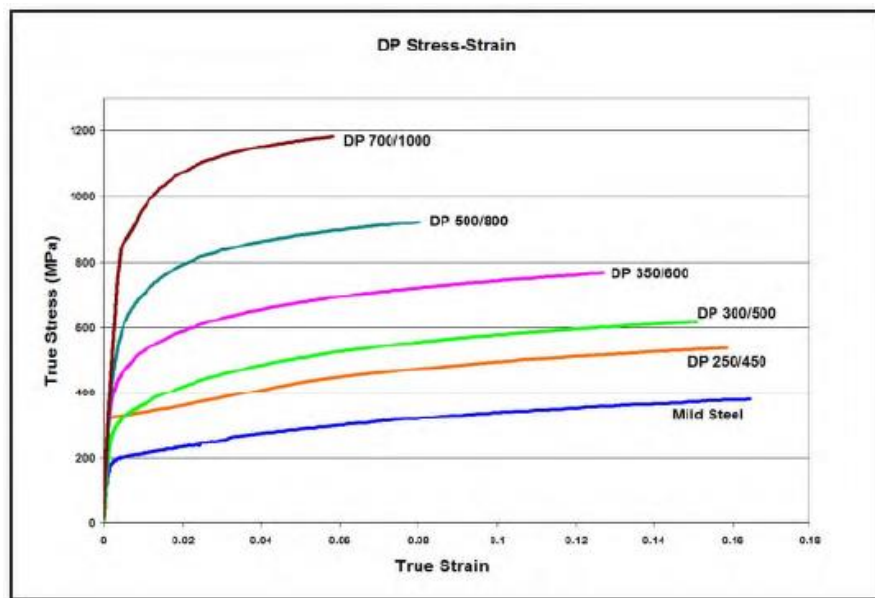


Figure 15: True stress-strain curves for a series of DP steel grades. Sheet thicknesses: DP 250/450 and DP500/800 = 1.0 mm. All other steels were 1.8-2.0 mm. (12)

As the percentage of martensite increases in the ferrite matrix, the steel achieves higher UTS, as illustrated in Figure 15. Compared to mild steel, DP steels exhibit a high initial strain hardening and an absence of an exact yield tensile strength. A justification for the continuous yielding behaviour could be the presence of induced mobile dislocations in the ferritic matrix that result in the elimination of yield point elongation. These mobile dislocations can also be the reason for the high work hardening rate. The finely dispersed martensite grains interact with these dislocations, resulting in high strain hardening, meaning that the plastic deformation and the hardening phenomenon occur around the martensitic islands (15).

Mild steel exhibits a constant strain hardening rate that can be described by the very popular Ludwik-Hollomon hardening rule, represented by equation (2.1).

DP steels do not exhibit this behaviour, instead, when plastic deformation occurs, the material presents a high initial hardening rate that, after a certain amount of plastic strain, starts to decrease to a constant value.

$$\sigma = K \varepsilon^n$$

where  $K$  [MPa] is the strength coefficient and  $n$  is the hardening exponent, known as the  $n$ -value. Ludwik-Hollomon model considers the  $n$ -value as a constant, but in AHSS steels there is variation in the strain hardening behaviour. This is mainly due to the multi-phase microstructure and the phase transformations during

deformation. Since  $n$  is not constant, the Ludwik Hollomon rule may not be valid for simulation purposes, regarding AHSS steels behaviour. Figure 16 illustrates the  $n$ -value evolution through engineering strain for a DP, TRIP and HSLA steels. It can be noticed the characteristic behaviour of the DP steel (16).

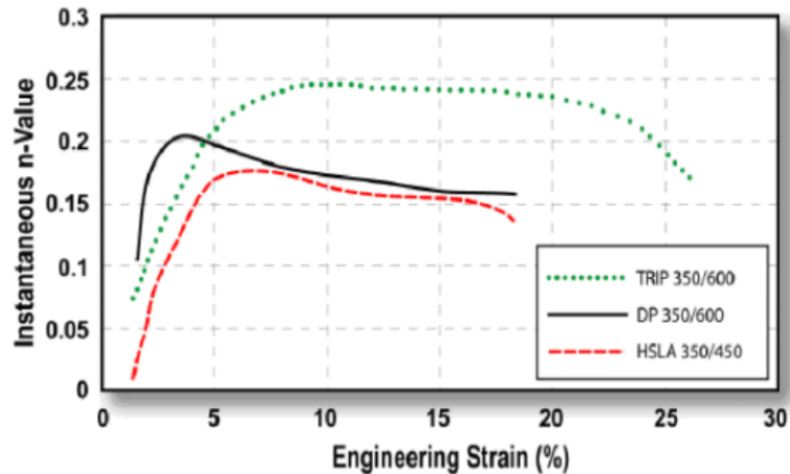


Figure 16: Instantaneous  $n$ -value vs engineering strain comparison between TRIP, DP and HSLA steel grades.

When it comes to DP steels manufacturing, an important aspect that must be considered is the transformation of austenite into martensite. The addition of alloying elements like Carbon (C), Manganese (Mn), Silicon (Si), etc. helps stabilizing this process (13).

DP steel sheets are produced by annealing low carbon steels into the inter-critical temperature range to form a mixed ferrite-martensite microstructure, followed by a rapid cooling to transform austenite into martensite (17). This microstructure can be developed through a hot rolling process or in a cold rolled sheet material (13).

The DP microstructure obtained by cold rolling is starting with a continuous

annealing process, where the sheet is heated up to a temperature between 730°C and 760°C. At this point, 15% of the microstructure, that is composed of ferrite and perlite, transforms into austenite. After this, the sheet is quenched and the austenite transform in martensite resulting, in a ferritic-martensitic microstructure (13).

The use of rolling processes induces crystallographic structure orientations, leading to a sheet steel with anisotropic behaviour. This means that the sheet steel will exhibit a different tensile strength when subjected to loads in different directions.

After plastic deformation, DP steels exhibit a reduction of the elastic modulus. This decrement has shown to be greater for small plastic strains and tends to an asymptotic value. DP steels that show a greater UTS (more martensite percentage) show a greater decrease in Young's modulus. The work of Hyunjin Kim et. al (18) shows some interesting conclusions and interpretations for the elastic modulus degradation. The authors state that the residual stress increases with deformation, disturbing elastic recovery causing a decrease in the elastic modulus. Another conclusion is that the accumulation of dislocations that move along the slip plane, while the front dislocations are stopped by grain boundaries. Many of these dislocations are repulsive to each other and are kept together by the applied stress. When the stress drops, the dislocations re-establish their previous equilibrium spacing with associated strain and an apparent degradation on elastic modulus (17) (18).

## Transformation-Induced Plasticity (TRIP) Steel

TRIP (Transformation-Induced Plasticity) steels have a dispersed multi-phase microstructure composed by a ferrite matrix, bainite, retained austenite (at least 5 percent) and martensite. As can be seen in Figure 17, the range covered by TRIP steels of strength and ductility is very similar to DP and CP (Complex Phase) steels, although TRIP steels endure higher values of elongation. This is due to the presence of retained austenite in the microstructure.

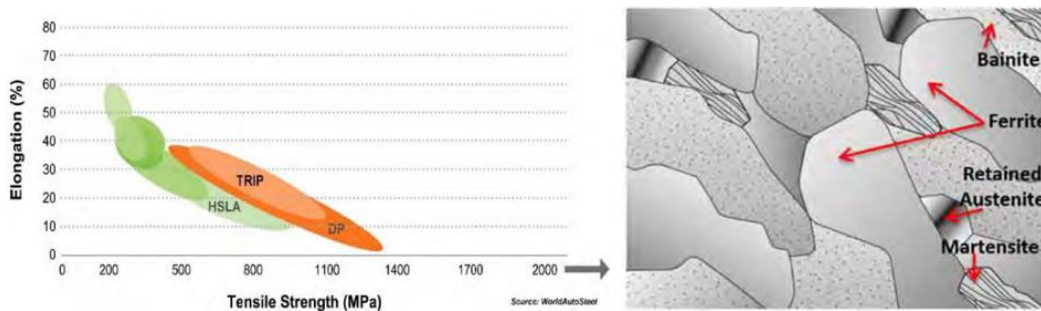


Figure 17: Schematic shows Bainite and retained austenite in TRIP steels.

During plastic deformation, austenite turns into hard martensite which allows a high hardening rate causing the resultant microstructure to be toughened by the hard martensite. Due to this transformation, the steel is capable of enduring high strain levels, and therefore reaches higher values of elongation (12) (13).

The high work hardening rate make these steels good for stamping applications, high energy absorption under strain results in a high level of crash energy absorption and excellent durability is suitable for parts that are subjected to high load cycles. Figure 14 illustrates the engineering stress-strain behaviour of HSLA, DP and TRIP steels of approximately similar yield strengths.

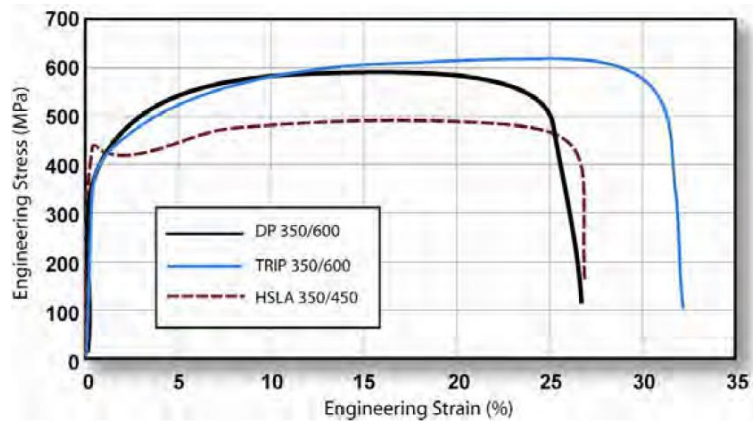


Figure 18: TRIP350/600 with a greater total elongation than DP 350/600 and HSLA 350/450

### Complex Phase (CP) Steel

Like TRIP steels, CP steels have a multi-phase microstructure. The microstructure of CP steels contains small amounts of martensite, retained austenite and pearlite within the ferrite/bainite matrix. An extreme grain refinement is created by retarded recrystallization or precipitation of microalloying elements like Ti or Nb.

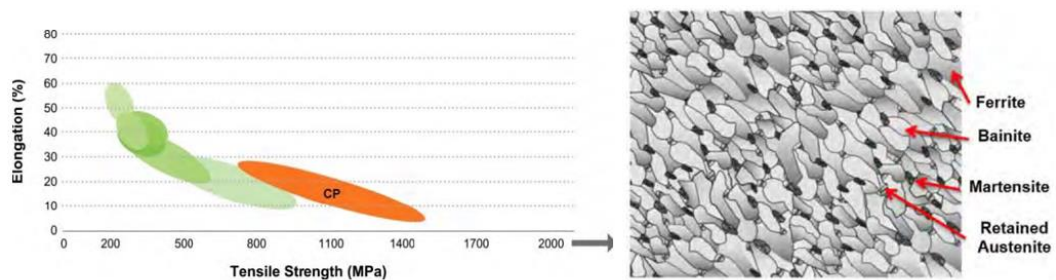


Figure 19: Schematic of CP steel microstructure.

The reason why CP steels have high yield strength and high elongation at tensile strengths (like DP steels), is the fine microstructure that characterizes this steel grade. The small grains in the microstructure cause a good edge stretchability, the high ultimate tensile strength and residual deformation capability result in a high

energy absorption and resistance to deformation which is good for car safety parts.

(12)

### Martensitic (MS) Steel

The steel that provides the highest UTS, in the first generation of AHSS, is the MS steel with values between 900 to 1700 MPa. This extremely high strength is due to a quenching process after hot rolling (or annealing), where almost all austenite is transformed into martensite. The resulting microstructure is composed by a martensite matrix with a small amount of ferrite and bainite phases.

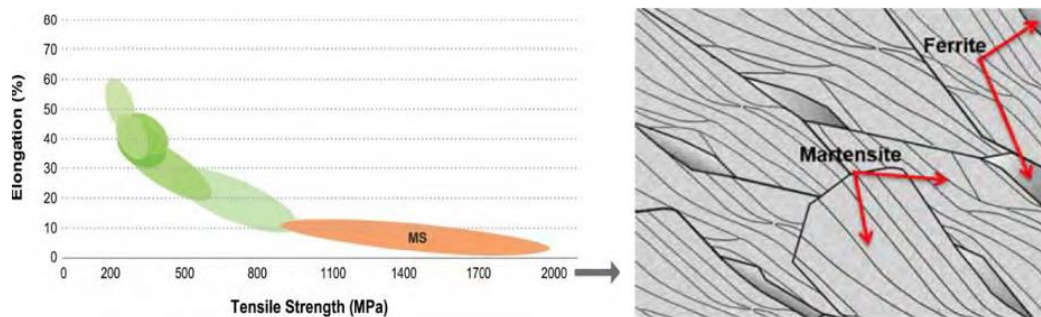


Figure 20: Schematic of Martensitic steel microstructure.

Despite the highest UTS, MS steels exhibit the lowest elongation. So, MS steels are often subjected to post-quenching tempering with the aim of improving ductility and formability. Due to the high UTS, these steels allow the production of strong and light-weight components but with the limitations of low elongation and high springback effects (13).

### Ferritic-Bainitic (FB) Steel

FB steels sometimes are utilized for improved edge stretch capability. Ferritic-

Bainitic steels have a microstructure of fine ferrite and bainite. Strengthening is obtained by both grain refinement and second phase hardening with bainite.

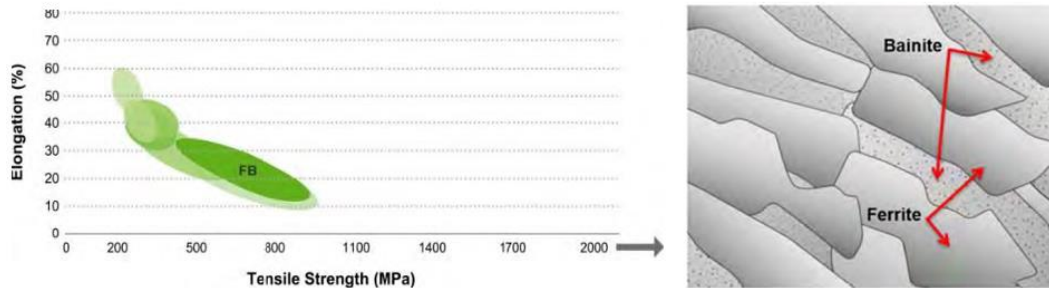


Figure 21: Schematic of Ferritic-Bainitic steel microstructure.

The primary advantage of FB steels over HSLA and DP steels is the improved stretchability. FB steels are also considered for tailored blank applications. These steels are characterized by both good crash performances and good fatigue properties. (12)

### Twinning-Induced Plasticity (TWIP) Steel

TWIP steels have a high manganese content (17-24%) that causes the steel to be fully austenitic at room temperatures.

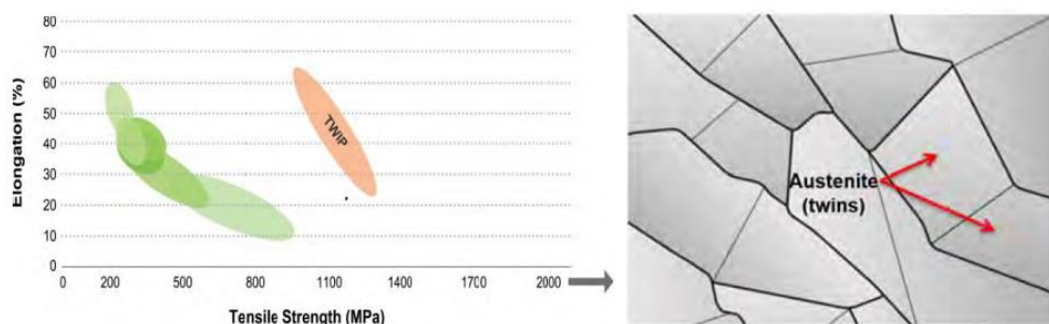


Figure 22: Schematic of TWIP steel.

A large amount of deformation is driven by the formation of deformation twins.

This deformation mode leads to the naming of this steel class. The twinning causes the microstructure becomes finer and finer. The resultant twin boundaries act like grain boundaries and strengthen the steel. TWIP steels combine extremely high strength with extremely high stretchability (12).

### **2.3 Applications of AHSS**

Several key considerations drive material selection for automotive applications. AHSS uniquely satisfy efficiency, emissions, manufacturability, durability, and cost requirements.

Key reason to utilize AHSS are (1) better performance in crash energy management, and (2) superior strength allowing this performance to be achieved with thinner materials, translating into lower vehicle weight. It is important to note that the auto industry has adopted light-weighting as a greenhouse gas reduction strategy because of the environmental and climate change concerns are escalating and becoming day by day more important.

Consumers are demanding safe cars, and governments are responding with new tests and standards that influence auto body structures, design, and materials.

The ability to carry the required static and dynamic loads, particularly in a crash event, is one of the key design considerations for vehicle structures. The passenger compartment, enclosed in a rigid “safety cage”, is designed to protect the passengers in the event of a low or high-speed crash; the structure should prevent

any deformation or intrusions that would compromise the integrity of the cage structure and impinge on the space around the passengers. The so-called “crumple zones”, located at the front and rear of the vehicle, are designed to absorb as much energy as possible in the event of a front or rear collision. By absorbing the energy over a distance, the crumple zone will cushion the impact and help preserve the structure of the passenger compartment. Clearly, the choice of steel properties, such as those shown in Figure 23, guides steel-types selections for specific applications. The components are designed so that together they form a structure that meets all requirements, particularly all crash cases, both those enforced by regional regulatory bodies and those set internally by car companies (12).

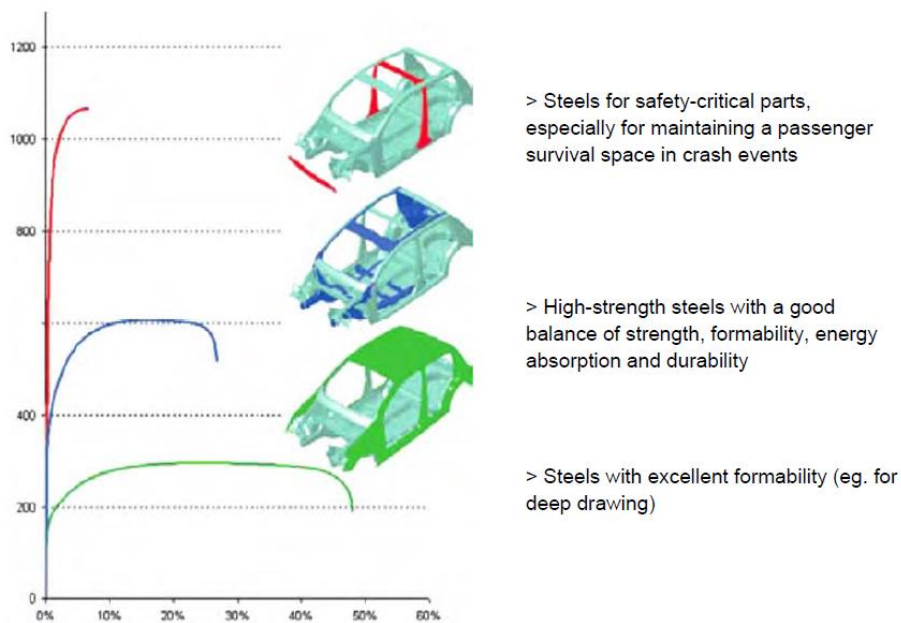


Figure 23: Stress (in MPa) vs. percent elongation for different steel types and their applications in body structure.

## CHAPTER 3:

# DETERMINATION OF MATERIAL PROPERTIES AND FORMABILITY

This chapter contains a review of the typical material characterization tests performed to understand the different materials behaviour and to define the Hardening Curve, and the Forming Limit Curve.

### 3.1 Tensile Test

The uniaxial tensile test, industry standard (EN ISO 6892-1), is the most common and cost-effective test method for determination of mechanical properties of a material. It provides information on the strength and ductility of materials under uniaxial tensile stresses. The results of tension tests of specimens machined to standardized dimensions from selected portions of a part or material may not totally represent the strength and ductility properties of the entire product or its in-service behaviour in different environments.

For testing metallic materials in the form of sheet, plate, flat wire, and strip ranging in nominal thickness from 0.13 to 19 mm the standard "Sheet-Type Specimen" is used where the ends are gripped, and the specimen is pulled at a constant rate until fracture occurs.

During the test, the load and elongation is measured, and several mechanical properties as listed below can be obtained:

- 1) Engineering stress-strain
- 2) Young's modulus
- 3) Total and uniform elongation
- 4) Yield and ultimate tensile strength
- 5) Plastic strain ratio ( $R$ -values)

The true stress-true strain data that is used to describe the flow stress data of the material can be calculated using the equations:

$$\varepsilon_{true} = \int_{L_0}^L \frac{dl}{l} = \ln\left(\frac{L}{L_0}\right) = \ln(1 + \varepsilon_{eng})$$

$$\sigma_{true} = \sigma_{eng}(1 + \varepsilon_{eng})$$

The engineering stress-strain curve as shown in Figure 20 is obtained from the load extension curve by using equations:

$$\varepsilon_{eng} = \frac{\Delta l}{l_0}$$

$$\sigma_{eng} = \frac{F}{A_0}$$

Figure 24 shows typical engineering stress-strain curve obtained from the tensile test. Since the specimen is under in-plane uniaxial strain state, the formability of the material is limited, and the material data can only be obtained up to a small strain value compared to the strains observed in industrial stamping operations where the strain state may not be linear uniaxial and can cover different linear or non-linear strain path from pure shear to balanced biaxial.

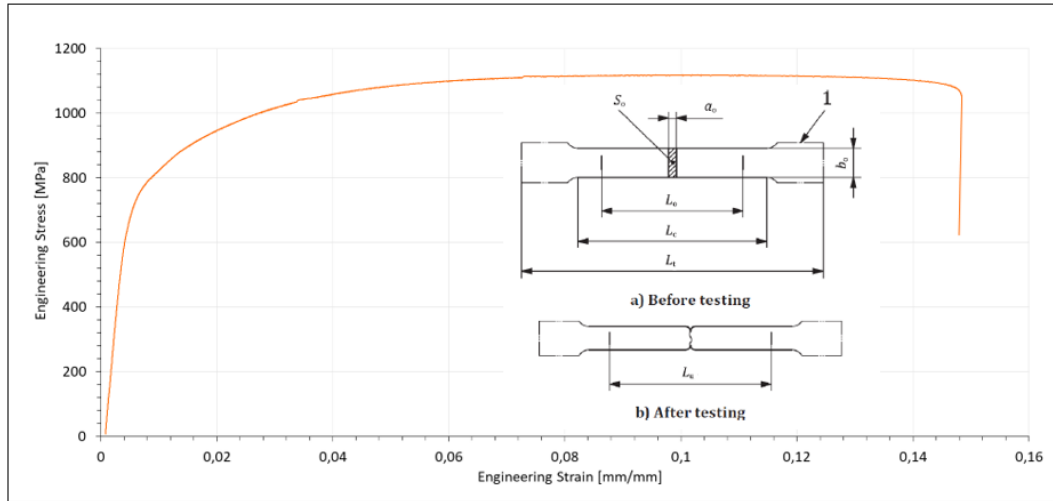


Figure 24: Engineering stress-strain curve, DP1000 - thickness 1.2 mm.

$a_0$	Original thickness of a flat test piece or wall thickness of a tube
$b_0$	Original width of the parallel length of a flat test piece
$L_c$	Parallel length
$L_0$	Original gauge length
$L_t$	Total length of test piece
$L_u$	Final gauge length after fracture
$S_0$	Original cross-sectional area of the parallel length
1	Gripped ends

Table 3: Tensile test specimen parameters.

### 3.2 Cyclic Loading-Unloading Tensile Test

With increasing plastic strain, the AHSS steel Young's modulus decreases. To observe this phenomenon, one must perform a cyclic load-unload tensile test.

This test consists in loading the specimen to a certain amount of plastic strain followed by an unloading until zero stress (LU test). The process is repeated the desired number of times, as shown in Figure 25. When it comes to DP steels, the elastic modulus degradation follows a saturation curve with increasing LU cycles. Therefore, when a certain value is reached the elastic modulus stops decreasing and becomes constant.

As depicted in Figure 25, the DP1000 – 1.2mm thickness, virgin Young’s modulus was 195526 MPa and the following Young’s modulus after LUL tests were 198097 MPa, 182786 MPa, 163495 MPa respectively.

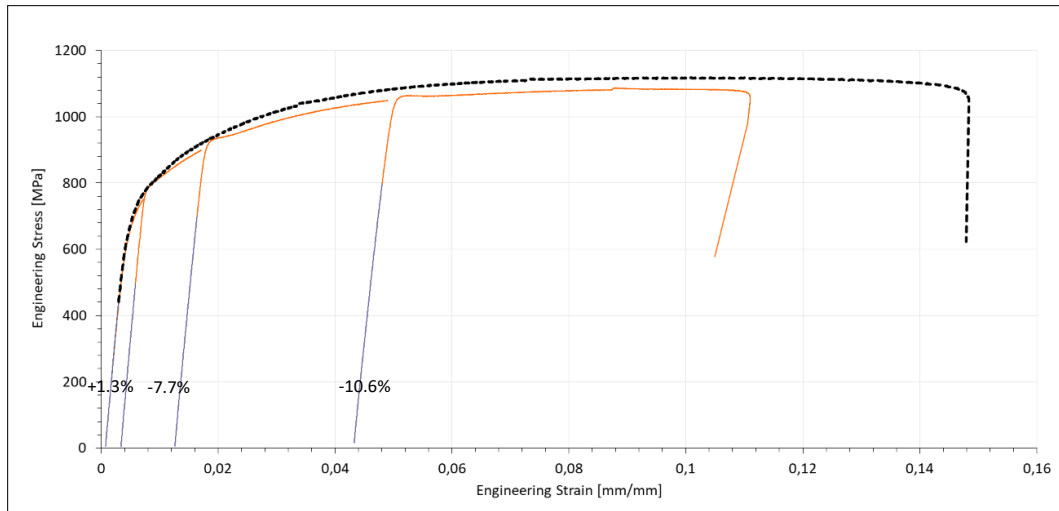


Figure 25: DP1000 engineering stress-strain LUL test – thickness 1.2 mm

The change of elastic modulus with the increase of plastic strain was first investigated by Lems (19) and he stated that the point defects and dislocations are the main cause of this change. More recently Morestin et al. (4) used a uniaxial tensile test during the loading process for the investigation and they stated that the work hardening is a possible cause of appreciable decrease in the Young’s modulus and this property diminishes with increase of plastic strain. It was observed that this diminution can reach more than 10 % of the initial value after only 0.05 plastic strain as we can observe in Figure 25.

DP1000 could be pre-strained only to 0.1 and the higher pre-strain is not achievable due to the strong tendency of buckling of the specimen.

The degradation in the apparent Young's modulus for DP1000 is 26% from the initial state to pre-strain of 0.09 with the saturated value of the Young's modulus being 156 GPa according to the study carried out by Hamad ul Hassan et al. (20).

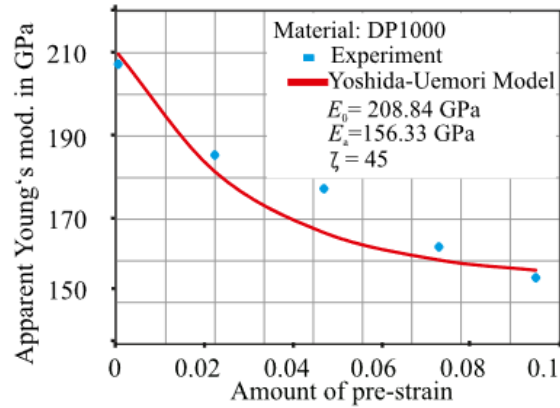


Figure 26: Apparent Young's modulus degradation with pre-strain DP1000

### 3.3 Biaxial Bulge Test

Hydraulic Bulge (HB) test and Viscous Pressure Bulge (VPB) test are other test methods for determination of flow stress data. In these tests, a sheet is clamped around its edge and stretched against a circular die using hydraulic fluid or a viscous material as a pressure medium. The sheet material is deformed under balanced biaxial tension until it bursts. Compared to uniaxial tensile test, higher range of strain can be obtained under biaxial tensile condition (21) (22). The higher strain range obtained from the biaxial test eliminates the need for extrapolating the flow stress data to predict the material behaviour in simulation of industrial stamping operation.

The bulge test can determine the formability of material in biaxial loading state. As it can be seen in the Figure 27, the Uniaxial tension test can reach plastic strain up

to 0.1 while for the Bulge test values around 0.5 can be easily reached.

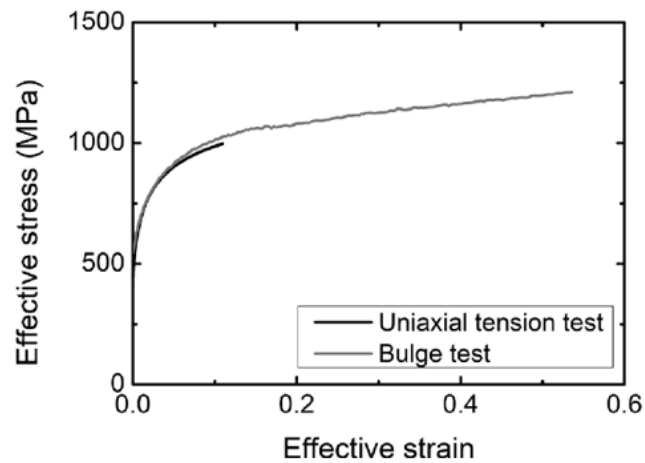


Figure 27: Schematic of comparison between Uniaxial tension test and Bulge test.

### 3.4 Combined – Tensile and Bulge Test – Method

For more accurate determination of flow stress data, i.e., instantaneous value of stress required to continue plastically deforming a material - to keep it flowing, a combined method is introduced.

In this method both the tensile test and the bulge test results are used to define the hardening behaviour of the material, Figure 28. The yield stress-strain of a selected material is determined through the tensile test. Then, a power law equation ( $\sigma = K\varepsilon^n$ ) is fitted to the strain-stress data obtained from the bulge test and the curve is extrapolated from left side until the yield stress is achieved, explicative Figure 29.

With this methodology, a reasonably reliable flow stress data can be determined from the yield point up to the maximum strain values obtained from the HB/VPB test.

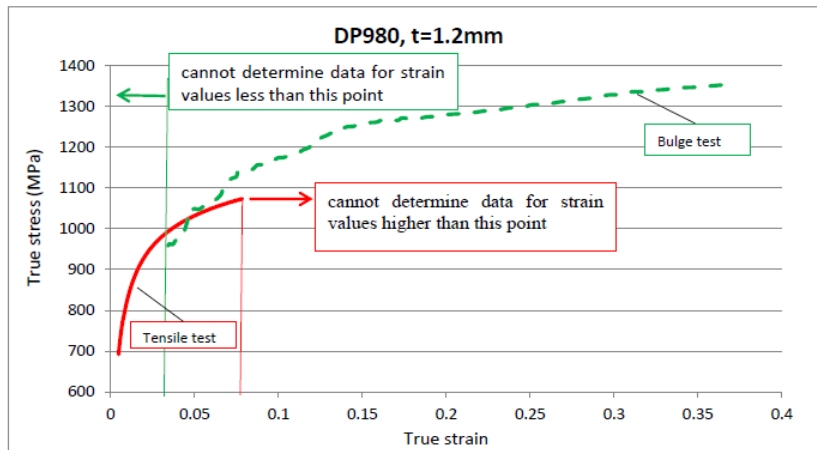


Figure 28: Flow stress data obtained from the tensile test and the bulge test.

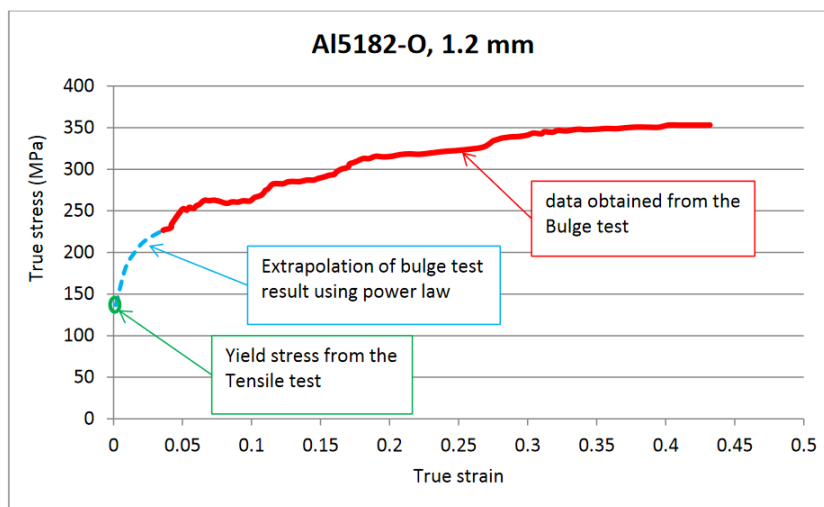


Figure 29: Flow stress data obtained from the combined method.

### 3.5 Formability and Drawability

In sheet metal forming, sometimes the formability and drawability terms are mistakenly used. The word “formability” refers to the ability of material to plastically deform before necking and failure occur. Formability is a material property independent on the process parameter. The word “drawability”, on the other hand, is the ability of the sheet material to deform into a specific part without failure. Not only the material properties, but also the process parameters such as

lubrication, tooling geometry, forming speed, blank size and geometry can affect the drawability of a material. (9)

In sheet metal forming, for a successful tool and process design, information about both the formability and the drawability of the selected material is crucial.

There are several test methods to evaluate the formability of a material. As far as we have seen, tensile test and biaxial bulge test are two test methods that can determine the formability of material in uniaxial and biaxial loading state.

Forming Limit Diagram (FLD) is another method to evaluate the formability of material. It is a graphical description of surface strain limits of a material and depicts the major strains and minor strains at the onset of localized necking. To develop a Forming Limit Curve (FLC), sheet metal specimens with different geometry, Figure 30, are formed using a hemispherical punch (Nakazima) or a cup test (Marciniak).

### **Nakazima Test**

The Nakazima test enables the material to experience various loading paths by varying the specimen width, allowing the material to flow in different strain paths.

According to ISO 12004 standard, a hemispherical punch is used to stretch the sheet material. The local major and minor strains close to the location of failure is measured using circle grid or digital image correlation (DIC) technique.

Sample preparation and experimental method for determination of FLC requires intensive effort and time. Some parameters such as the sheet thickness, specimen

edge quality, and the friction and lubrication between the sheet and tool interfaces can significantly affect the test result. Therefore, the FLC of a material is not only dependent to the material but the test condition also influences the result.

To predict failure in Finite Element (FE) stamping simulation a failure criterion is required. Even though the strain states in the sheet metal forming process is complex, the FLD is an important tool in practical press shop to predict the failure risk.

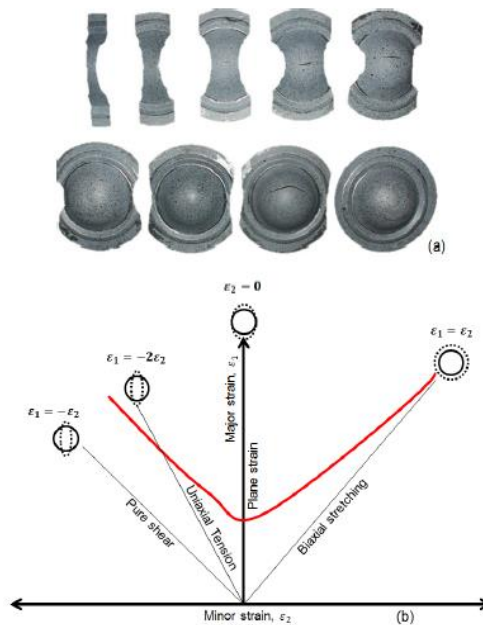


Figure 30: Example of specimen geometries required for developing the FLD, (b) schematic of a FLD.

### 3.6 Tension-Compression Test

There are many plastic deformation processes in the steel industry where the material is submitted to cyclic tension-compression loads. When a metal sheet is drawn over a die corner, or through a drawbead, the material is subjected to

bending, stretch unbending, and reverse bending. To perform an accurate simulation of such a sheet metal forming process, it is necessary to have an appropriate constitutive model, which can consider the phenomena that occurs during cyclic loading, such as the Bauschinger effect, the transient behaviour, the permanent softening, and the work-hardening stagnation, Figure 31. All these effects can be described by the so-called “hardening law” and can be observed with the cyclical uniaxial tension/compression test. In practice, however, such a test is very difficult to perform, due to the tendency of the strip to buckle in compression.

When a material is loaded (and plastically deformed) followed by an unloading, to zero stress, there will remain residual stresses between the material grains. If the same material is now loaded in the opposite direction, the entrance in plastic deformation will be influenced by the residual stresses leading to an early re-yielding. This is called the Bauschinger effect (23).

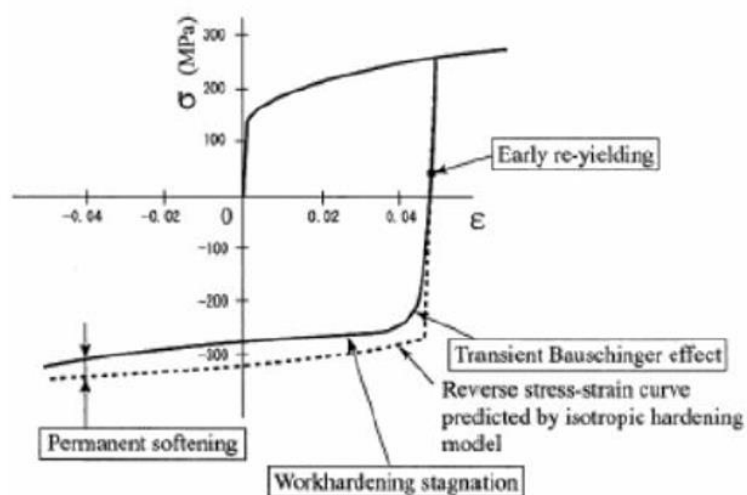


Figure 31: Schematic illustration of the effects occurring during a tension/compression loading cycle.

Many purely phenomenological hardening laws have been proposed in the literature with the purpose of describing the cyclic behaviour of metal sheets. The complexity of these models varies within a wide range with respect to number of material parameters and history variables.

## CHAPTER 4:

# CONSTITUTIVE MODELS

In today's industries, a major part of the quality assurance for products are made in an early stage using several different Finite Element Analysis (FEA) software's. This allows testing of the stamping procedure pre-production for analysing purposes.

The main purpose of constitutive models is to predict springback. Some models can accurately estimate the material behaviour, while others only provide a rough estimation. The aim of this chapter is to explain the fundamentals of constitutive models, and to provide an overview of the parameters required by each material model. Generally, the more advanced the material, the more complex the law required to accurately describe the yield surface, the more experimental information and more complex tests are necessary to define the yield surface.

As previously mentioned, DP steels present high springback after plastic deformation. One way of dealing with this problem is to vary the parameters that influence the springback (like punch and die radiuses, sheet thickness, etc.) and perform experimental test until the desired part geometry is obtained. This is a high-cost method since the new tools must be designed for new test setups. Also, it results in a great waste of raw material. The solution to face this issue is through simulation. With a constitutive material model which can describe the material behaviour accurately and describe the springback phenomenon, one can significantly reduce the tool adjustments and material waste.

## **4.1 AutoForm Forming Solver**

AutoForm is a finite element-based software that is commonly used by car manufacturers to define, run, and analyse sheet metal forming simulations. The finite element method used in the software is based on implicit incremental techniques which allow for accurate results for the numerical calculations. Advantages of using the implicit solution are that it allows for larger time steps than in the explicit method. Large and small elements can be combined without the calculation time being affected by the size of the smallest element. Another advantage of the implicit method is that it allows for shorter calculation times even in more complex material models. The software also uses an adaptive time step control which optimizes the time steps used in the simulation regarding accuracy and computing time. AutoForm also uses adaptive mesh which allows for a higher density in strongly curved geometries spots. This adaptive mesh allows for more accurate reading of the results but also leads to an increase in needed computational power (24) (25) (26).

### **Material input in AutoForm**

In AutoForm, the material constitutive model is a part of the material input which consists of three main groups: the hardening curve, the yield surface, and the curve/forming limit diagram; where all three has a huge role in the accuracy of the results for the simulation, Figure 32.

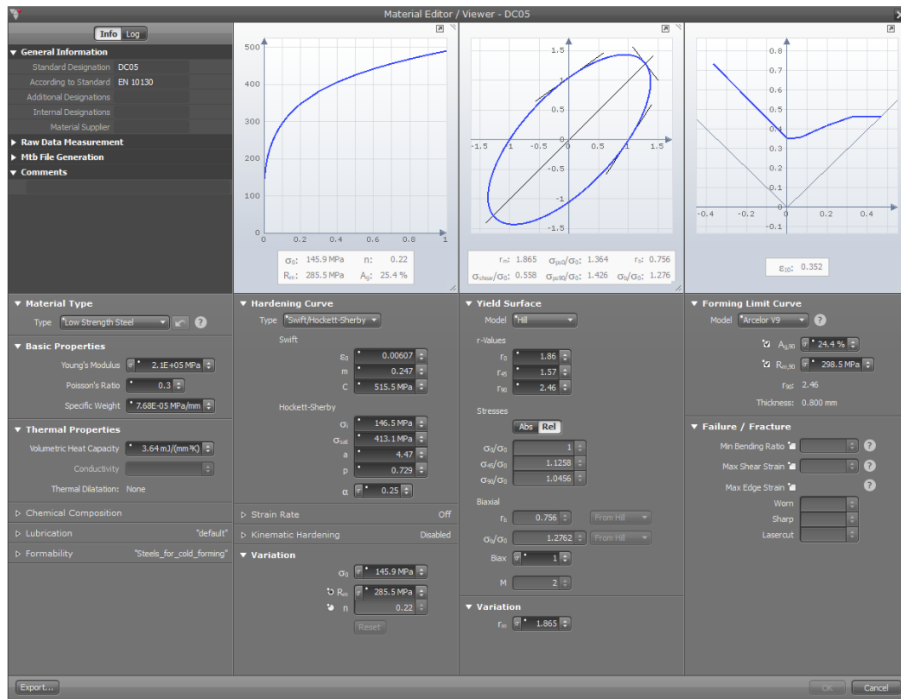


Figure 32: Example of a Material Card in AutoForm.

## Hardening curve

The hardening curve describes how the material gains strength as it deforms. This can be visualized using a strain/stress curve where both an elastic region and a plastic region can be observed. Any deformation within the elastic region will not cause any permanent deformation on the specimen after unloading. The important part of the stress/strain curve is the plastic region and can be obtained with uniaxial tension test. As the tensile test only provides usable results until 0.1 roughly plastic strain, the rest of the flow stress data up to 0.5 plastic strain can be obtained by means either a bulge test, extrapolation, or a compression test (28).

The advanced kinematic hardening model, available within AutoForm, describes the following phenomena observed in Kinematic Hardening: early re-plasticization,

non-linear elasticity, transient softening, work hardening stagnation.

### **Yield surface**

The yield surface is a visual representation of how the material will deform depending on what type of stress is affecting the system. It defines the transition from the elastic to the elastic-plastic region in multi-axial stress space. Any stress which does not exceed the boundaries of the yield surface will only result in an elastic deformation which means that the specimen will return to its original shape. Once a point reaches the yield surface the material begins to plastically deform.

In the case of isotropic hardening, the yield surface will grow accordingly with increased plastic deformation, the growth speed of the yield surface will be dependent on the hardening curve. This occurs as the material will need a higher strain for plastic deformation after hardening (28). However, if the point is subjected to a reversal in the stress direction, the yield surface may not expand but its center moves in stress space known as kinematic hardening.

Although typically drawn in three dimensions ( $\sigma_x, \sigma_y, \sigma_z$ ), in forming simulations it is generally assumed that the third component  $\sigma_z$  (through sheet thickness stress) is so small in comparison with the in-plane stresses, as to be safely ignored. For this reason, it is typical to see the yield surface drawn and defined in two dimensions.

The first implementation of yield surface is from Tresca in the 1870s and was later improved in 1913 by von Mises. The difference of these surfaces, Figure 33, is the

same as the difference of aluminium and steel as these shapes are generally how the material yield surface will look, Tresca for aluminium and von Mises for steel.

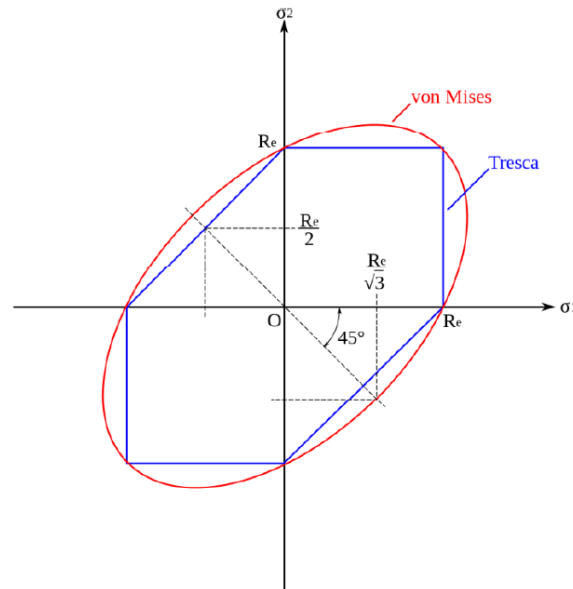


Figure 33: Tresca and von Mises yield criterion

The yield surface is directly affected by the material input as well as what material model is being used as this will calculate the surface using the different input parameters. The variance in parameters that are needed for the models is the main reason for the complexity variation for the user.

The yield surface consists of several different points that can be seen in Figure 34 which describes what type of strain will affect that area. These types of strains can be simplified to different types of load cases. This makes it possible for the simulation software to calculate a combination of these stresses and from that make a conclusion if the part will go over the elastic region and start plastic deformation.

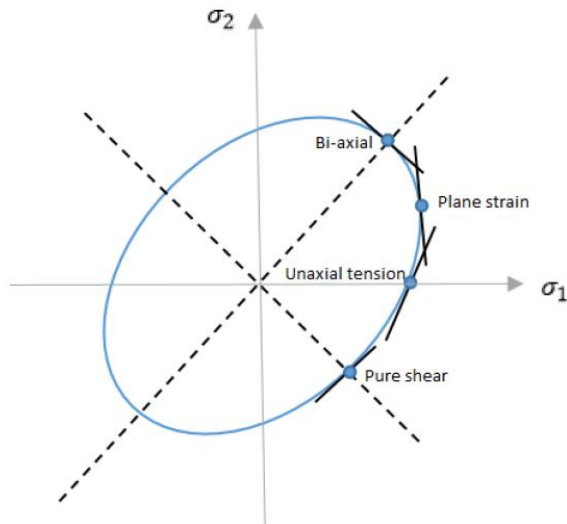


Figure 34: Yield surface, strain types.

The different load cases that are being used for the yield surface can be seen in Figure 35.

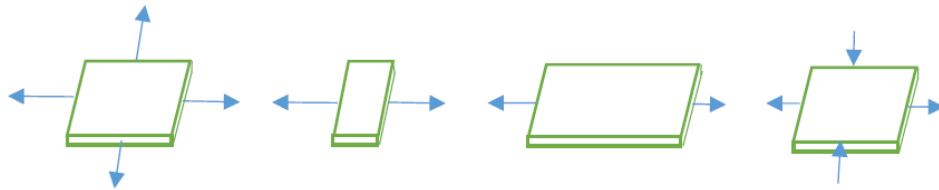


Figure 35: Load cases yield surface (in order: biaxial stress, plane strain, uniaxial tension, and pure shear)

This is the base for all material models as it uses some of these points to estimate the yield locus shape. The most important part of the yield locus is the plane strain points as materials will always fail in plane strain. This area of interest will focus on the first quadrant of the yield locus as it is where the most effects will occur.

### Forming Limit Curve (FLC) and Forming Limit Diagram (FLD)

Forming Limit Diagram is commonly used within sheet metal forming simulations to predict the forming behaviour of sheet metals. This information is achieved using

a predictive method of what combination of major and minor strain that is affecting the part and giving a visual representation of where the part will have defects such as the risk of splits, excess thinning, and splits. This is shown in Figure 36.

Usually, the formability limit is defined at necking onset, since in normal production conditions, the local necking cannot be allowed, neither from the aesthetic appearance point of view nor from the functional operation of the part. Other phenomenon is related with compressive stresses, which can also cause a local instability of the sheet. This phenomenon is regarded as wrinkling. It is also evident that, besides local necking and fracture, wrinkling should also be avoided (27).

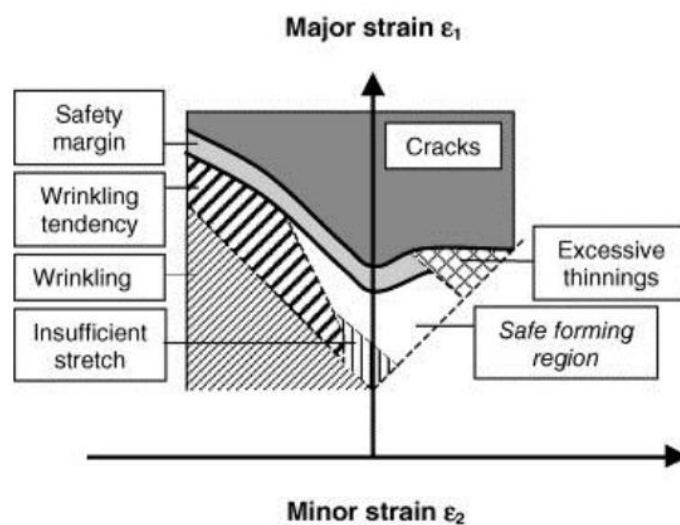


Figure 36: Characteristic limit curves and zones of the Forming Limit Diagram.

## 4.2 Fundamentals of Constitutive Models

As previously mentioned, DP steels present high springback after plastic deformation. Researchers have shown that the stress-strain response of sheet metal under cyclic tension and compression loading is complex and may not follow a linear isotropic hardening rule. The Bauschinger effect, transient behaviour, work hardening stagnation, and permanent softening, are the four main phenomena occurring during reverse loading, Figure 37.

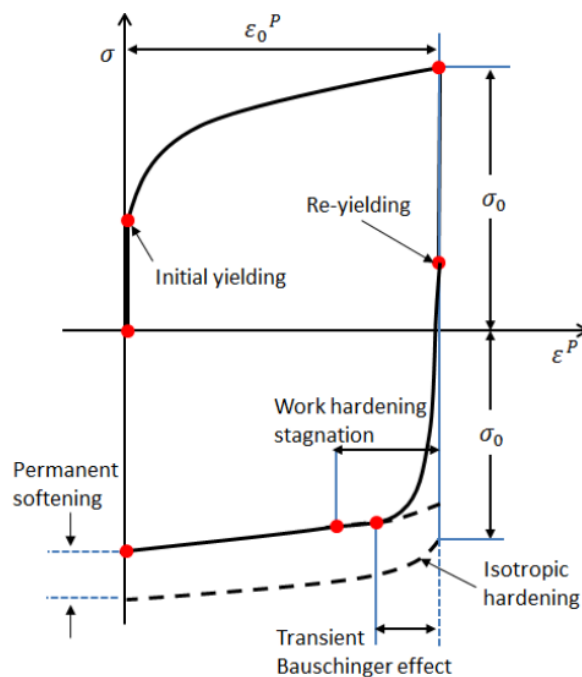


Figure 37: Schematic of stress-strain response of a sheet metal under tension-compression loading.

There are extensive research studies on developing material models able to capture the characteristics illustrated in Figure 37. The focus of these models is the yield function and hardening behaviour of the material.

In materials with work hardening characteristic, once yield occurs, the stress needs

to be continually increased to drive the plastic deformation. In multiaxial loading case, the initial yield surface is usually defined as:

$$f(\sigma_{ij}) = 0$$

However, in materials with strain hardening behaviour, the size, the shape, and the position of the yield surface can be changed during the plastic deformation.

Therefore, the yield surface can be described by:

$$f(\sigma_{ij}, K_i) = 0$$

Where,  $K_i$  represents one or more hardening parameters which determine the evolution of the yield surface.

Different hardening models are shortly discussed in the next sub-sections.

### **Isotropic Hardening (IH)**

Steels present a strain hardening phenomenon when the yield tensile strength is surpassed. If one only relies on yield surface (like von Mises criterion), the strain hardening cannot be represented. Meanwhile with IH model, when the plastic deformation begins, the yield surface expands with increasing stress without changing its shape, as illustrated in Figure 38. Because the yield surface expanded, after unloading, the material has a new yield tensile strength, considering the material hardening. If reloading occurs the material now has a new tensile strength, which is important for metal forming simulations (29).

Hence, in isotropic hardening model, the shape and position of the yield surface remains unchanged but expands with increasing stress. The yield function is described by the following equation:

$$f(\sigma_{ij}, K_i) = f_0(\sigma_{ij}) - K = 0$$

The initial shape and the size are specified by the initial yield function,  $f_0(\sigma_{ij})$ , and the hardening parameter  $K$  controls the expansion of the yield surface.

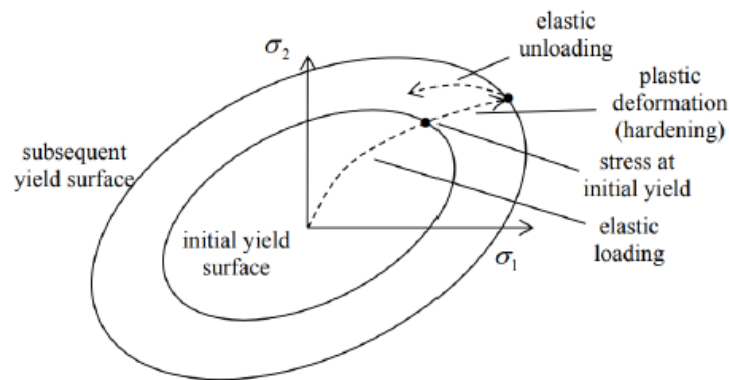


Figure 38: Isotropic Hardening scheme.

### **Kinematic Hardening (KH)**

Although the isotropic hardening model does capture the hardening behaviour, it implies the yield strength in tension and compression are the same and remain equal as the yield surface increases with plastic strain. As previously mentioned, this does not happen due to the Bauschinger effect and strain softening, in reverse stress. So, to model the Bauschinger effect which is important when considering springback for materials such as aluminum and high strength steels, one can use the kinematic hardening model. The yield surface remains the same size and shape but translates in the stress space (29).

The yield function takes the general form:

$$f(\sigma_{ij}, K_i) = f_0(\sigma_{ij} - \alpha_{ij}) = 0$$

The hardening parameter in this model,  $\alpha_{ij}$ , is known as the back-stress tensor. This parameter is responsible for the translation of the yield surface, Figure 39.

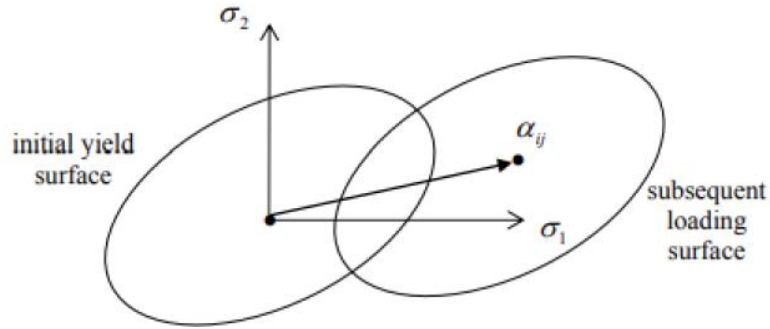


Figure 39: Schematic of kinematic hardening model.

### Combined Isotropic and Kinematic Hardening (IH+KH)

Neither the isotropic nor the kinematic hardening model can describe accurately the behaviour of sheet material in cyclic tension compression loading state. Therefore, more complex hardening rules such as combined isotropic-kinematic hardening (IH+KH) model are introduced (30) (31) (32) (33). The IH+KH model combines features of both the isotropic and kinematic hardening models and the yield function takes the general form:

$$f(\sigma_{ij}, K_i) = f_0(\sigma_{ij} - \alpha_{ij}) - K = 0$$

The yield function both translates and expands with plastic strain. Figure 40 demonstrates how the yield surface would behave in a combined hardening scenario (29).

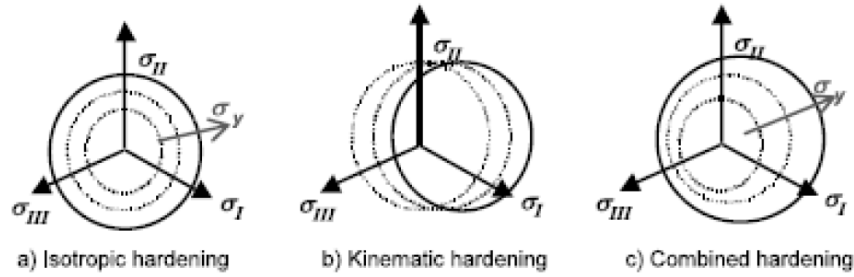


Figure 40: Yield surface modifications in principal stress plane.

### Multi Surface Hardening Models

Multi surface hardening models are the improved versions of the IH+KH models. In a multi surface hardening model, there are two surfaces: the yield surface and the bounding surface. The bounding surface expands and slightly moves with increasing plastic strain. The yield surface moves within the bounding surface. The Yoshida-Uemori (Y-U) model is one of the conventional two surface (yield surface and boundary surface) plasticity hardening models (32). In this model the relative kinematic motion of the two surfaces is a function of the difference between their sizes. Furthermore, the yield surface never crosses the bounding surface, Figure 41.

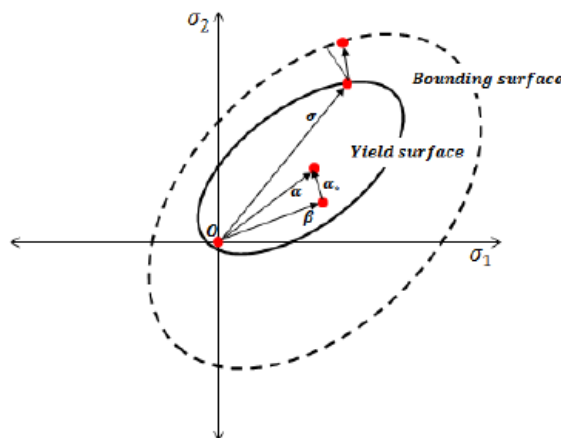


Figure 41: Yoshida-Uemori two surface model.  $\alpha$  is the center of the yield surface,  $\beta$  is the center of the bounding surface, and  $\alpha^*$  is the relative motion of the yield surface with respect to the bounding surface.

## **Anisotropic Yield Function**

Most sheet metals are anisotropic as the result of rolling process used in making the sheets. It means that the properties of the sheet material are dependent to the direction the properties are measured with respect to the rolling direction. Therefore, anisotropic yield surfaces are introduced to represent the plastic behaviour of the material more accurately. Hill's Quadratic Yield function (Hill, 1948) and Barlat Non-Quadratic Yld2000 (Barlat et al., 2005) are two conventional anisotropic yield functions used in simulation of sheet metal forming.

### **4.3 Hardening Curve available in AutoForm**

There are several predefined equations in the Material Generator for defining the Hardening Curve:

- a) Ludwik
- b) Swift/Krupkowski
- c) Ghosh
- d) Hockett-Sherby
- e) Combined Swift/Hockett-Sherby
- f) Yoshida-Uemori

Since during the Forming process, biaxial strain conditions may occur that are significantly higher than those measured in the Uniaxial Tensile test, the Hardening Curve should be extrapolated to a true strain value of at least  $\epsilon_{pl} = 1.0$ . This is

typically done by fitting the experimental data to a predefined equation (for example Swift).

### **Ludwik**

The hardening curve is determined by an approximation using the Ludwik formula:

$$\sigma = K \varepsilon^n$$

$$\sigma(\varepsilon_{pl} = 0) = \sigma_0$$

In the Ludwik formula  $\sigma$  is the true stress,  $K$  is the strength coefficient,  $n$  is the strain hardening exponent,  $\varepsilon$  is the total logarithmic strain,  $\varepsilon_{pl}$  is the plastic part of the total strain,  $\sigma_0$  is the yield stress. Within the Material Generator, the user may also use  $R_m$  (Ultimate Tensile Strength) in place of  $K$ .

### **Swift**

By using the Swift formula, the hardening curve is determined by:

$$\sigma = C(\varepsilon_{pl} + \varepsilon_0)^m$$

Where  $\varepsilon_{pl}$  is the true effective plastic strain, and  $\varepsilon_0$  is the elastic strain at the initial yield point.

### **Ghosh**

By using the Ghosh formula, the hardening curve is determined by:

$$\sigma = C(\varepsilon_{pl} + \varepsilon_0)^m - D$$

Where D is a material constant.

### **Hockett-Sherby**

By using the Hockett-Sherby formula, the hardening curve is determined by:

$$\sigma = \sigma_{sat} - (\sigma_{sat} - \sigma_i)e^{-\alpha\varepsilon_{pl}^p}$$

Where  $\sigma_{sat}$ ,  $\sigma_i$ ,  $\alpha$ , and  $p$  are material constants.

### **Swift/Hockett-Sherby**

By using the Swift/Hockett-Sherby formula, the hardening curve is defined using a combination of the Swift and Hockett-Sherby approximation. The combination factor  $\alpha$ , determines the weighting of the functions:

$$\sigma = (1 - \alpha)\{C(\varepsilon_{pl} + \varepsilon_0)^m\} + \alpha\{\sigma_{sat} - (\sigma_{sat} - \sigma_i)e^{-\alpha\varepsilon_{pl}^p}\}$$

### **Yoshida-Uemori**

The Yoshida-Uemori Kinematic Hardening model is defined using a combination of the Voce and Swift approximations. The combination factor  $\mu$ , determines the weighting of the functions:

$$\sigma = (1 - \mu)\{Y + R_{sat}(1 - e^{(-m\varepsilon_{pl})})\} + \mu\{C(\varepsilon_{pl} + \varepsilon_0)^n\}$$

The parameters are described as follows:

$Y$ : Initial yield stress (initial size of the yield surface)

$R_{sat}$ : Saturated size of the bounding surface

$m$ : Rate of evolution of the bounding surface

$C$ : Parameter for Swift hardening curve

$n$ : Parameter for Swift hardening curve

$\varepsilon_0$ : Parameter for Swift hardening curve

$\mu$ : Mixing factor between Swift and Yoshida hardening curves for tensile curve

$E_\alpha$ : Saturated Young's modulus

$\zeta$ : Rate of Young's modulus reduction

$\alpha_0$ : Initial distance between the yield and bounding surfaces

$C$ : Rate of translation of the yield surface

$b_{sat}$ : Saturated amount of translation of the bounding surface

$h$ : Rate of evolution of the stagnation surface

$r_0$ : Initial size of the stagnation surface

## 4.4 Yield Surface available in AutoForm

### Quadratic Hill Yield Criterion

In 1948, Hill developed a yield criterion that considers orthotropic anisotropy states, i.e., their properties depend on the direction in which they are measured, and its mechanical or thermal properties are unique and independent in three mutually perpendicular directions. For an arbitrary anisotropy state where the principal

anisotropy and global axis coincide, the Hill criterion is represented by the following equation (23):

$$F(\sigma_y - \sigma_z)^2 + G(\sigma_z - \sigma_x)^2 + H(\sigma_x - \sigma_y)^2 + 2L\tau_{yz}^2 + 2M\tau_{zx}^2 + 2N\tau_{xy}^2 = 1$$

Where F, G, H, L, M and N are constants that characterize the anisotropy state.

The sheet anisotropy state can be characterized through uniaxial tensile tests, with the specimens withdrawn from different directions in the sheet plane.

For instance, with the specimen represented in Figure 42, it is possible to obtain the anisotropy coefficient ( $r$ ), also known as **Lankford coefficient**,  **$r$ -value** or **plastic strain ratio**. This coefficient is obtained by the quotient between specimen width ( $\varepsilon_w$ ) and thickness ( $\varepsilon_h$ ) true strains:

$$r = \frac{\ln\left(\frac{w}{w_0}\right)}{\ln\left(\frac{h}{h_0}\right)} = \frac{\varepsilon_w}{\varepsilon_h}$$

Where  $h_0$ ,  $w_0$ ,  $h$ ,  $w$  [mm] are, respectively, the initial thickness and width, the instantaneous thickness and width.

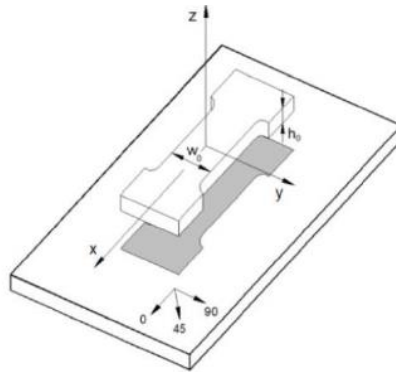


Figure 42: Sheet withdrawn specimen in the rolling direction.

If the Lankford coefficients in the 3 directions are known ( $r_0$ ,  $r_{45}$  and  $r_{90}$ ) one can determine the Hill's yield criterion constants:

$$H = \frac{r_0}{1 + r_0}; \quad F = \frac{r_0}{(1 + r_0)r_{90}}; \quad N = \frac{(r_0 + r_{90})(2r_{45} + 1)}{2(1 + r_0)r_{90}}; \quad G = 1 - H$$

The **normal  $r$ -value** (normal anisotropy coefficient):  $R$  is taken to be the average.

$$R = \frac{r_0 + r_{90} + 2r_{45}}{4}$$

In stamping application, materials having a high **normal  $r$ -value** are appreciated since present a higher resistance to thickness reduction and, therefore, a higher strength in biaxial stress states which is the stress state where fracture typically occurs, e.g., the areas in contact with the bottom and the edge of the punch (23).

Figure 43 shows the influence of this coefficient on the shape of the yield function.

The higher the normal  $r$ -value, the more elliptical the shape of the yield function.

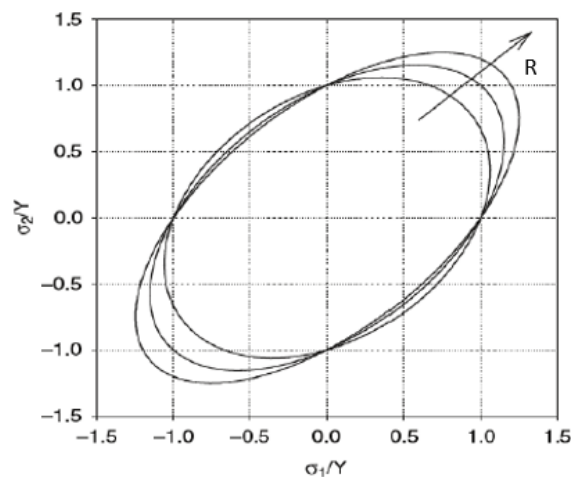


Figure 43: Influence of the normal anisotropy coefficient.

The **planar anisotropy coefficient** ( $\Delta r$ ) or **planar  $r$ -value** is a measure of  $r$ -value with angle from the rolling direction. It quantifies the difference between the sheet properties in every 45 degrees direction. For instance, if  $\Delta r = 0$  the sheet has the same  $r$ -value in every direction (23). This coefficient can be calculated by the following expression:

$$\Delta r = \frac{r_0 + r_{90} - 2r_{45}}{2}$$

### **Hill 48 vs Hill 90**

The Hill 48 Model is not suitable for the modelling of a Yield Surface defined with  $r$ -value  $< 1$ . The Hill 90 formulation was in response to the known issue of poor agreement between the experimentally measured biaxial points and the predicted yield surface for materials where  $r < 1$ .

The biaxial stress factor,  $Biax = \frac{b}{a}$ , allows the yield surface to be expanded or contracted at the equi-biaxial stress points, Figure 44.

Meaningful values of the biaxial stress factor range from 0.8 to 1.2. If the biaxial stress factor is set equal to 1.0, then classical Hill '48 model is used. If a biaxial stress factor is chosen to be less or more than 1.0, model like Hill '90 is used.

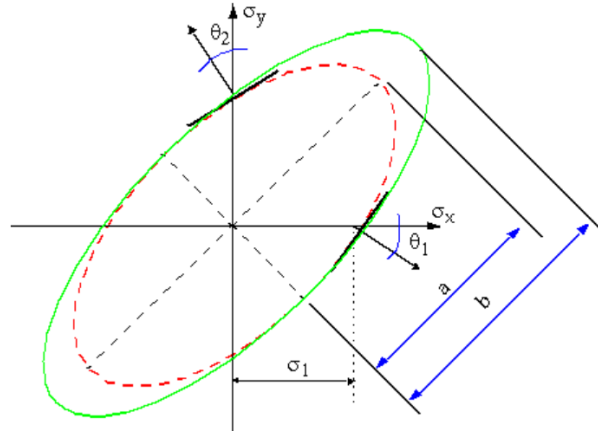


Figure 44: Hill model using the biaxial stress factor.

### Barlat and Lian Yield Criterion

Barlat and Lian, in 1989, proposed a yield function that describe the orthotropic behaviour of sheet metals under full plane stress state. In addition, it gives an approximate representation of polycrystalline yield surfaces (34).

The yield function is given by:

$$a|k_1 + k_2|^M + a|k_1 - k_2|^M + c|2k_2|^M = 2\sigma_e^M$$

$$k_1 = \frac{\sigma_{xx} + h\sigma_{yy}}{2}; \quad k_2 = \sqrt{\left(\frac{\sigma_{xx} - h\sigma_{yy}}{2}\right)^2 + p^2\tau_{xy}^2}$$

Where  $a$ ,  $c$ ,  $h$  and  $p$  are material constants that can be obtained through the Lankford coefficients, like in Quadratic Hill yield criterion:

$$c = 2 \sqrt{\frac{r_0}{(1+r_0)} \cdot \frac{r_{90}}{(1+r_{90})}}; \quad a = 2 - c; \quad h = \sqrt{\frac{r_0}{(1+r_0)} \cdot \frac{1+r_{90}}{r_{90}}}$$

The  $M$  parameter is a constant that depends in the crystallographic structure. For instance, a BCC (body-centered cubic) material, such as a Ferritic-Martensitic steel

(DP steels),  $M$  takes the value of 6, according to the article referenced as (34).

The Barlat model was originally developed for the description of Aluminium alloys.

The default  $M$  value of 8 typically gives a good representation of the behaviour of Aluminium.

### **BBC (2005) Model**

The yield surface according to Banabic et. al. is more flexible than the previous models according to Hill or Barlat, which gives the surface a greater ability to describe the onset of yielding. However, consequently, the equation requires 9 experimentally determined input parameters in order to fully capture the surface.

The yield surface is defined using  $r$ -value in  $0^\circ$ ,  $45^\circ$ ,  $90^\circ$  alignment with respect to rolling direction,  $(r_0, r_{45}, r_{90})$ , and the three initial yield stresses  $\sigma_0$ ,  $\sigma_{45}$  and  $\sigma_{90}$ . These values are generally available since they can be attained from the standard uniaxial tensile tests when performed in the three directions to rolling. Additionally, two other parameters may be defined: the bi-axial yield stress point  $\sigma_b$  and the bi-axial  $r$ -value  $r_b$ .

It is strongly recommended to only use these additional parameters (bi-axial yield stress point  $\sigma_b$  and the bi-axial  $r$ -value  $r_b$ ) if reliable experimental data are available.

If Biaxial data is not available, the user may elect to allow the software to compute values for  $\sigma_b$  and the bi-axial  $r$ -value  $r_b$  from either the Hill or Barlat Yield Surface approximation.

## Vegter Model

The Vegter yield function is based on reference points that are determined from well-defined experiments, i.e., shear test ( $\sigma_{SH}$ ), the uniaxial test ( $\sigma_{UN}$ ), the plane strain test ( $\sigma_{PS}$ ) and the equibiaxial ( $\sigma_{BI}$ ) test. Reference points of the Vegter yield surface are shown in Figure 45:

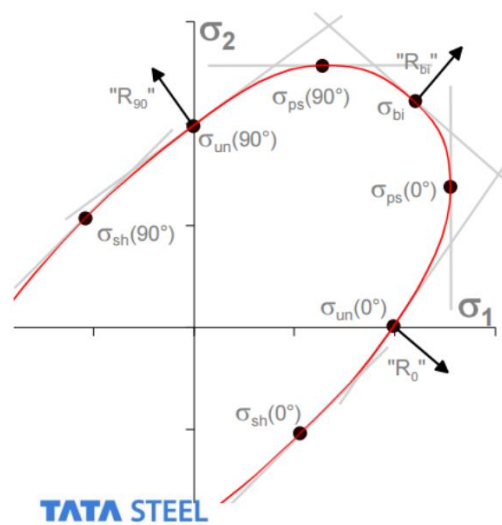


Figure 45: Vegter yield surface.

The Vegter model is formulated in normalized stress space, i.e., each stress value is normalized to the uniaxial stress in the longitudinal direction. The model accurately describes all stress points, i.e., uniaxial ( $\sigma_{UN}$ ), plane strain ( $\sigma_{PS}$ ), shear ( $\sigma_{SH}$ ) and biaxial ( $\sigma_{BI}$ ). The description of all the stress points makes the model flexible and suitable for material variation studies.

A new approach was developed by TATA Steel in which the 17 Vegter parameters are defined based on correlation functions, which only require tensile test data in the  $0^\circ$ ,  $45^\circ$  and  $90^\circ$  directions.

This new formulation allows advantages for the user (compared to Hill 48):

The Vegter model is much more flexible and accurate than Hill 48. The total simulation quality regarding material flow, tool force, springback is expected to be significantly improved. No additional test data is required, compared to what is already typically measured and documented.

#### **4.5 Forming Limit Curve available in AutoForm**

The Forming Limit Curve (FLC) is commonly used in sheet metal forming simulations to predict the onset of material failure. The curve represents the maximum values of the major strains  $\varepsilon_1$  and  $\varepsilon_2$  measured at the onset of material failure. The test procedure should include deforming the material in different strain states (equi-biaxial, biaxial, plane strain, uniaxial etc.) to obtain the strain values at the onset of material failure. In general, if during the simulation the strain state of a particular element is equal to, or above the forming limit curve – failure of the material is taking place. Different methods can be followed to validate whether material failure will occur. Various models are available to define the FLC of a material:

- a) Keeler
- b) Arcelor V9
- c) Arcelor V9 Alu
- d) Tata Steel

### **Keeler**

The Keeler model is valid only for low carbon steels (mild and HSLA, but not DP nor IF).

### **Arcelor V9**

The Arcelor V9 model is used for steels with tensile strength ( $R_{m,90}$ ) equal from 260 MPa to 1500 MPa, sheet thickness from 0.5 mm to 3.5 mm and  $r_{90}$  value from 0.6 to 3. Additional inputs required are uniform elongation w.r.t. 90° rolling direction  $A_{g,90}$ , and tensile strength w.r.t. 90° rolling direction  $R_{m,90}$ .

### **Arcelor V9 Alu**

The Arcelor V9 Alu is a modified Arcelor V9 model used for aluminum material with sheet thickness from 0.5 mm to 3.5 mm.

### **Tata Steel**

The Tata Steel FLC (developed by Abspoel & Schilting) is determined using the total elongation (A) for 80 mm gauge length tensile bar ( $A_{80}$ ), the plastic strain ratio (r-value) and material thickness. The total elongation is determined according to ISO 6892-1 and the plastic strain ratio according to ISO 10113. It is advised to have tensile test results in transverse, diagonal, and longitudinal direction to determine the correct biaxial FLC point because the biaxial point is equal for all directions and the necking will occur for the lowest value.

## CHAPTER 5: EXPERIMENTAL ACTIVITY – MATERIAL CHARACTERIZATION OF DUAL PHASE 1000

The main goal of this study is to study and predict springback in advanced high strength steel as DP1000 – thickness 1.2 mm. The U-shaped bend test is commonly used to study the springback phenomenon.

To better understand DP1000 material, a series of characterization tests are conducted. The data obtained will support the present dissertation in material parameters identification and material model validation.

### 5.1 Material Composition

Our material under investigation is a Dual Phase Steel 1000 with the following designation CR550Y980T-DP and thickness 1.2 mm. Since it was not possible to perform a chemical composition investigation, our study relies on the Voestalpine Steel Division, Table 4.

Steel grade	C max	Si max	Mn max	P max	S max	Al	Cr + Mo max	Ti + Nb max	B max	Cu max
CR550Y980T- DP	0.20	1.00	2.90	0.050	0.010	0.015 – 1.0	1.40	0.15	0.005	0.20

Table 4: DP1000 Material Composition.

### 5.2 Uniaxial Tensile Test

The starting point of experimental work is the uniaxial tensile test. Being one of the most common and universal tests, the uniaxial tensile test allows to observe certain

phenomena and quantify certain mechanical properties, like yield, ultimate tensile strength, Young's modulus, plastic strain ratio ( $r$ -value).

The normative according to the tests were performed is EN ISO 6892-1-2019, method of tests at room temperature. The machine on which the tests were performed is the 8801 Instron - Servohydraulic Testing machine with 100kN load cell capacity.

### **Test results, accuracy of testing apparatus**

According to the specifications reported in the 8801 Servohydraulic Testing handbook, the load weighing accuracy of the machine is  $\pm 0.5\%$  of indicated load or  $\pm 0.005\%$  of load cell capacity, whichever is greater. It means that we have an error of at minimum  $\pm 5\text{N}$  and at maximum which is variable. Here reported as an example, for the uniaxial tensile test conducted in our study (DP1000, 12.5 mm gauge length), the maximum load measured was 16772N. The correct reading of this value is  $16772\text{N} \pm 84\text{N}$ .

Dynamic Extensometer for direct strain measurement and closed loop strain control; suitable for tensile, compressive & fatigue testing, the extensometer has a 12.5mm gauge length with a travel of  $\pm 2.5\text{mm}$  giving  $\pm 20\%$  strain (accuracy of measurement can be  $\pm 2\ \mu\text{m}$ ).

### **Test pieces, shape, and dimensions**

The test pieces were obtained by laser cutting samples from the blank – thickness

1,2 mm. The alignments with respect to rolling direction were 0° - 45° - 90°. The cross-section of the test pieces is rectangular with a gauge width of 12,5 mm according to the Standard. Machined test pieces have a transition radius between the gripped ends and the parallel length of about 21 mm. Figure 46 shows the dimensions of the tensile specimen.

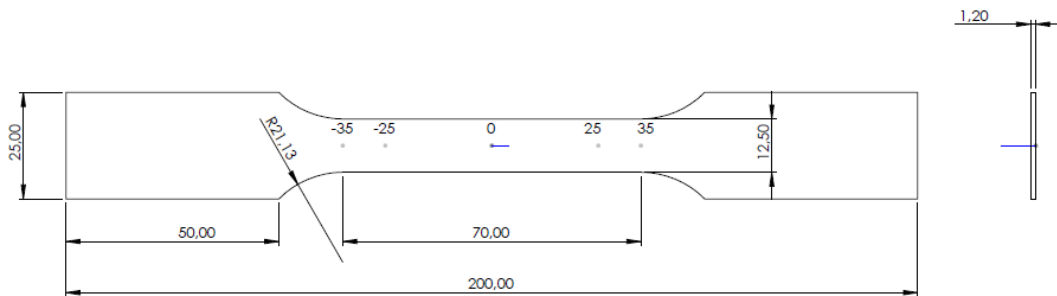


Figure 46: Uniaxial tensile test specimen - DP1000.

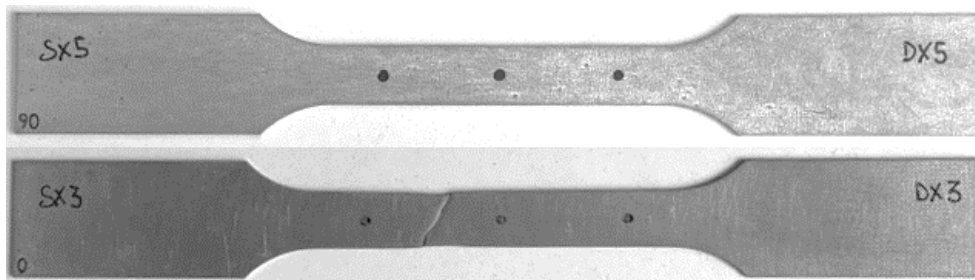


Figure 47: Schematic of tensile specimens at 0°, 90° w.r.t. RD - DP1000, 1,2 mm thickness.

$a_0 = 1,20 \text{ mm}$	Original thickness of a flat test piece or wall thickness of a tube
$b_0 = 12,50 \text{ mm}$	Original width of the parallel length of a flat test piece
$L_c = 70 \text{ mm}$	Parallel length
$L_o = 50 \text{ mm}$	Original gauge length
$L_t = 200 \text{ mm}$	Total length of test piece
$S_o = 15 \text{ mm}^2$	Original cross-sectional area of the parallel length

Table 5: Tensile test specimen dimensions.

Engineering stress-strain curve DP1000 – 0° alignment w.r.t. rolling direction

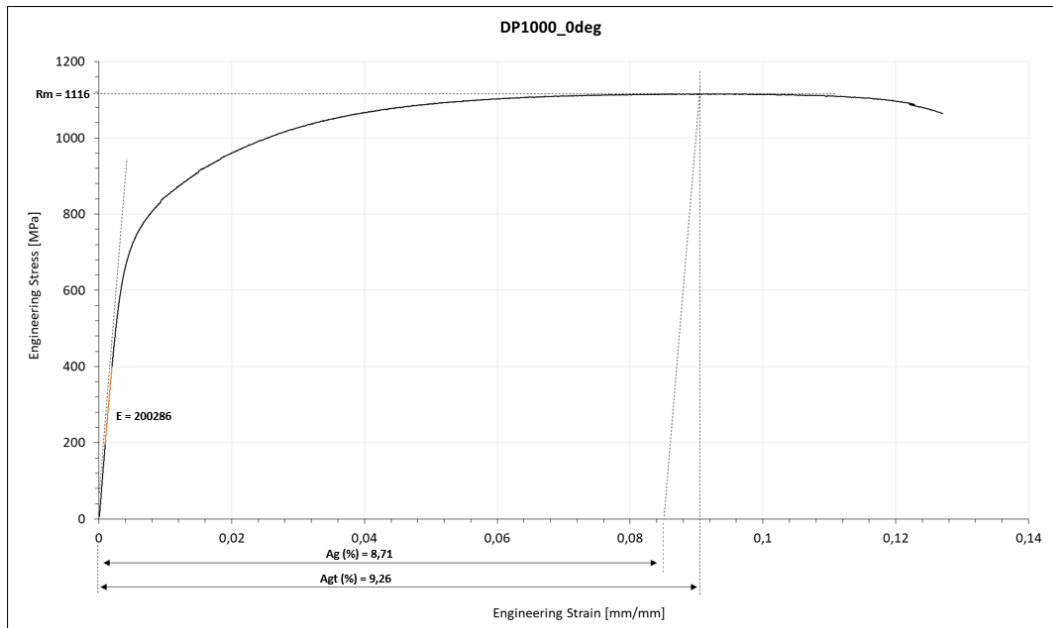


Figure 48: Engineering stress-strain curve for DP1000 – 0° alignment w.r.t. rolling direction.

To characterize the anisotropic behaviour of Dual Phase 1000 DP, the Lankford coefficients were obtained with tensile testing with specimen withdrawn in 0°, 45°, 90° from the rolling direction. The data obtained by these tests are shown in Table 6. The results indicate that DP possess anisotropic behaviour through thickness, which is good for stamping applications.

<i>Material</i>	<i>Lankford coefficients</i>	<i>Normal anisotropy coefficient</i>	<i>Planar anisotropy coefficient</i>
<i>DP1000</i>	$r_0 = 0.246$	$R = 0.282$	$\Delta r = -0.042$
	$r_{45} = 0.303$		
	$r_{90} = 0.277$		

Table 6: Anisotropy coefficients for DP 1000.

Lankford coefficients (*r*-value) was determined according to EN ISO 10113:2020 – for sheet and strip made of metallic materials following method with width and

length extensometer (automatic method). Plastic strain ratio ( $r$ -value) is the ratio of the true plastic width strain to the true plastic thickness strain in a test piece that has been subjected to uniaxial tensile stress calculated using the following formula:

$$r = \frac{\varepsilon_{p_b}}{\varepsilon_{p_a}} = \frac{\ln\left(\frac{b_1}{b_0}\right)}{\ln\left(\frac{L_0 b_0}{L_1 b_1}\right)}$$

Where  $\varepsilon_{p_b}$  is the true plastic width strain and  $\varepsilon_{p_a}$  is the true plastic thickness strain.

The evaluation of  $r$ -values was calculated according to the evaluation for materials without yield point phenomena, starting from plastic deformation until  $R_m$  has been achieved. The instantaneous  $r$ -values were averaged between the 2-6% plastic engineering strain.

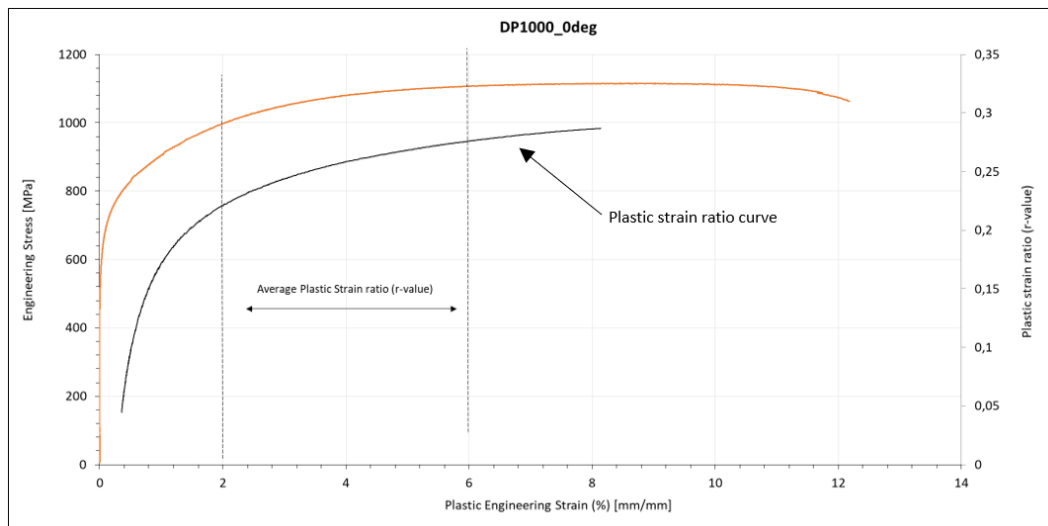


Figure 49: Schematic illustrating plastic strain ratio and plastic engineering strain-stress curve for DP1000 – 0° alignment w.r.t. rolling direction.

Table 7 summarizes the mechanical properties calculated from uniaxial tensile tests for the DP1000 – 1.2 mm thickness:

<i>Specimen</i>	<i>Young's Modulus, E (MPa)</i>	<i>Uniform Elongation, Ag (%)</i>	<i>Yield Strength, Rp0,2 (MPa)</i>	<i>Tensile Strength, Rm (MPa)</i>
DP1000 – 0° RD	202000	8,57	797	1114
DP1000 – 45° RD	188121	8,48	784	1082
DP1000 – 90° RD	197954	8,13	809	1118

Table 7: Mechanical properties DP1000 w.r.t. different Rolling Direction (RD).

### 5.3 Cyclic Loading-Unloading Tensile Test

To observe and evaluate the Young's modulus degradation, uniaxial loading-unloading tensile test were carried out. The Young's modulus can be obtained after every cycle through the engineering stress-strain curve, Figure 50.

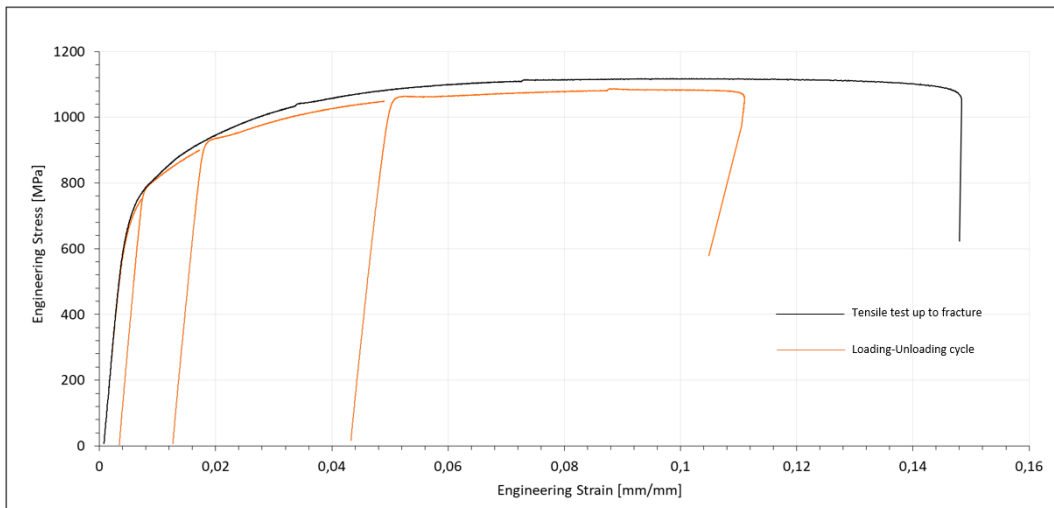


Figure 50: Engineering stress-strain curve for cyclic loading-unloading test - DP1000 - 1,2 mm thickness.

The methodology used to obtain the loading-unloading cycle was the following:

Load step up to 750 MPa → unload.

Load step up to 900 MPa → unload.

Load step up to 1050 MPa → unload.

Reload up to fracture.

Table 8 summarizes the results obtained from the tests and Figure 51 puts in evidence the degradation of the Young's modulus with increasing the pre-strain deformation.

<i>Specimen</i>	<i>Virgin Young's Modulus, E (MPa)</i>	<i>Young's Modulus with pre-strain 0,4%</i>	<i>Young's Modulus with pre-strain 1,2%</i>	<i>Young's Modulus with pre-strain 4,4%</i>
DP1000 – 0° RD	202000	198097	182786	163495
DP1000 – 45° RD	188121	187001	173931	158652
DP1000 – 90° RD	197954	196839	185199	173938

Table 8: Young's modulus degradation - DP1000.

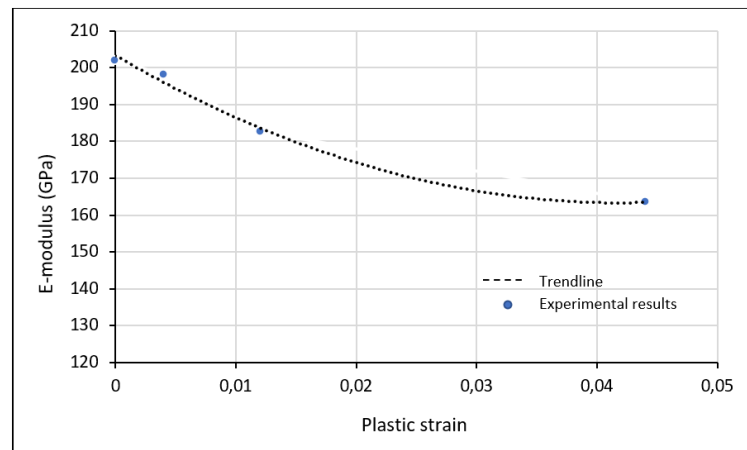


Figure 51: Representation Young's modulus degradation - DP1000 – 0° alignment w.r.t. RD.

### Variation of unloading elastic modulus with plastic strain

The reduction of the unloading elastic modulus with plastic strain can be determined through the loading-unloading tensile test. For many types of steel, the unloading elastic modulus decreases rapidly with increasing the plastic strain, though this effect tends to saturate at a strain value of about 0,2 (Lee et al., 2012). As shown in Figure 46, when unloading at about 0,044 plastic strain, the elastic

modulus of the DP1000 material is about 163 GPa. This is about 20% less than the original value (202 GPa) and could potentially produce more springback compared to using the standard  $E$ -modulus of 202 GPa. For practical modelling, it is easier to define the elastic portion of the deformation using a constant  $E$ -modulus. Yoshida et al. (2002) suggested to use an average  $E$ -modulus,  $E_{av}$ . They introduced the following equation to express the variation of  $E$ -modulus with plastic strain.

$$E_{av} = E_0 - (E_0 - E_a) \left[ 1 - e^{-\xi \varepsilon_0^p} \right]$$

Where  $E_0$  and  $E_a$  are the  $E$ -modulus for virgin and approximately large pre-strained materials, respectively, and  $\xi$  is a material constant.

In our case study: DP1000, the values for the  $E$ -modulus are listed in Table 9

$E_0 = 202 \text{ GPa}$	<i>Virgin Young's modulus</i>
$E_a = 160 \text{ GPa}$	<i>Young's modulus for approximately large pre-strain</i>
$\varepsilon_0^p = 0.007$	<i>Initial true plastic strain</i>
$\xi = 40$	<i>Young's reduction rate</i>
$E_{av} = 191743 \text{ MPa}$	<i>Average Young's modulus</i>

Table 9: Young's modulus degradation data for DP1000 - thickness 1,2 mm - 0° alignment w.r.t. RD.

## 5.4 Nakajima Test

The set of tests that involves the Nakajima were planned for the conception of a Forming Limit Diagram. An FLD is a diagram containing measured major/minor strain points on a formed part. An FLD can distinguish between safe and necked, or failed, points. The transition from safe to failed points is defined by the forming-limit curve (FLC).

The evaluation and the determination of the forming limit curve is carried out at the press shop considering the EN ISO 12004-2 normative.

A deterministic grid of precise dimensions is applied to the flat and undeformed surface of a blank. The forming limits are determined for several strain paths (different ratios between  $\varepsilon_1$  and  $\varepsilon_2$ ). The determined strain paths range from uniaxial tension to biaxial tension (stretch drawing). The collection of the individual forming limits in different strain states is plotted as the forming-limit curve. The curve is expressed as a function of the two true strains  $\varepsilon_1$  and  $\varepsilon_2$  on the sheet surface and plotted in a diagram, the forming-limit diagram. The minor true strains  $\varepsilon_2$  are plotted on the X-axis and the major principal true strains  $\varepsilon_1$  on the Y-axis.

The test piece is formed until fracture, and the percent change in the gauge length (circle dimensions) in the major direction and in the minor strain direction at  $90^\circ$  to this is measured to determine the forming-limit under the imposed strain conditions, Figure 52.

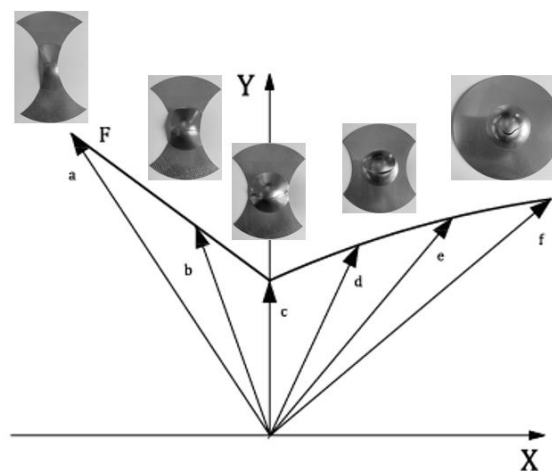


Figure 52: Forming Limit Curve.

X	Minor true strain, $\epsilon_2$
Y	Major true strain, $\epsilon_1$
F	FLC
a	Uniaxial tension, $\epsilon_2 = -[r/(r+1)] \epsilon_1$
b	Intermediate tensile strain
c	Plane strain
d	Intermediate stretching strain state
e	Intermediate stretching strain state
f	Equi-biaxial tension (=stretching strain state) $\epsilon_2 = \epsilon_1$

Table 10: Forming Limit diagram parameters.

Test pieces were prepared by laser cutting with the following geometries. Figure 53 shows the grid pattern which was superficially imprinted by laser engraving: circles' diameter of 5 mm. A schematic of the different specimen dimensions is illustrated in Figure 54.

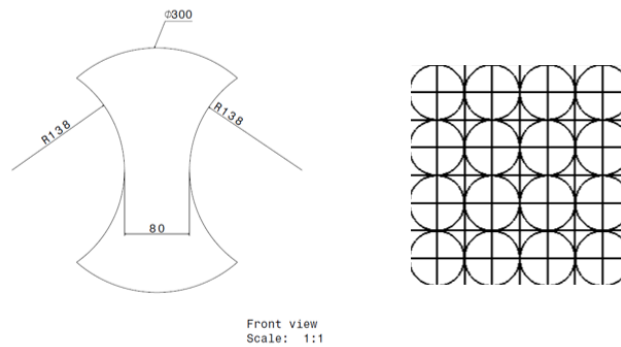


Figure 53: Nakajima specimen dimensions; Grid pattern.

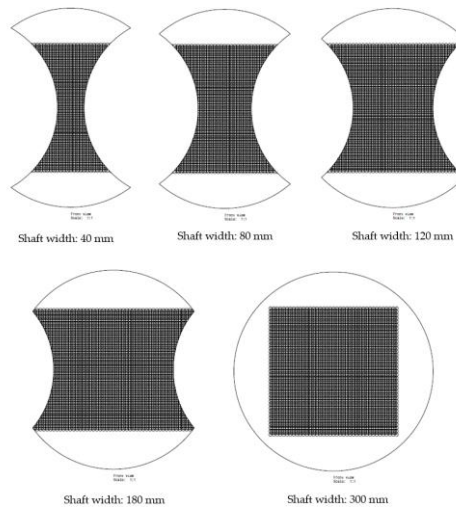


Figure 54: Different types of Nakajima specimens to obtain Forming Limit Curve.

The dimensions of the Nakazima tests are presented in Table 11.

Specimen	1	2	3	4	5
Shaft width (mm)	40	80	120	180	300
Diameter (mm)	300				
Radius (mm)	138				

Table 11: Specimen dimensions of the Nakazima tests.

As mentioned before, the Nakazima test allows the study of a certain material under different deformation paths. The results of this test are shown in the principal strain space, where the major and minor strains are referred to the first ( $\varepsilon_1$ ) and second ( $\varepsilon_2$ ) principal strains, respectively.

Since the specimen with the largest width is 300 mm, the loading path exhibited by the largest specimen is theoretically the same as the elementary biaxial tension ( $\varepsilon_1 = \varepsilon_2$ ). While for the specimen with the thinner width, the deformation should be closer to the uniaxial tensile test ( $\varepsilon_1 = -\varepsilon_2$ ).

The results of the Nakazima test for DP1000 steel are presented in Figure 55 and table 12.

Specimen	1	2	3	4	5
Major Strain	0.174	0.118	0.133	0.178	0.223
Minor Strain	-0.051	0	0.039	0.095	0.182

Table 12: Nakazima test results for DP 1000 steel – Sheet thickness 1,2 mm

The representation in the chart of the results of the Nakazima test for DP1000 steel are presented in Figure 55.

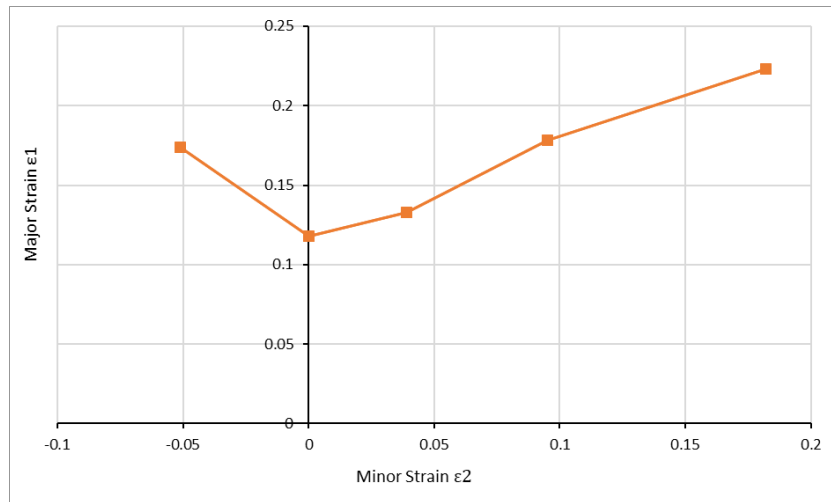


Figure 55: Nakazima Test Results - DP 1000, Sheet Thickness 1.2 mm

A schematic of the different specimen after fracture is illustrated in Figure 56.

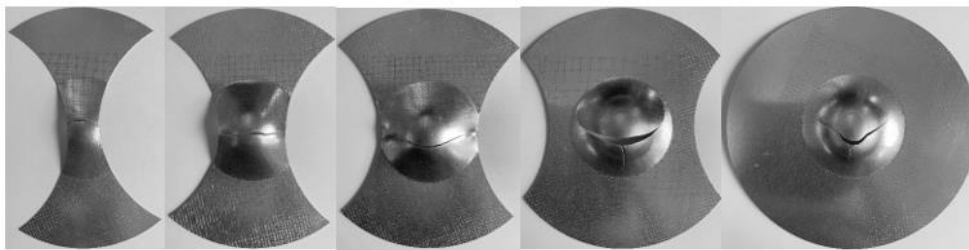


Figure 56: Nakazima Test specimens after fracture.

## 5.4 Tension - Compression Test

To perform an accurate simulation of sheet metal forming process, it is necessary to have an appropriate constitutive model, which can consider the phenomenon that occur during cyclic loading, such as the Bauschinger effect, the transient behaviour, the permanent softening, and the work hardening stagnation.

The simplest and straight-forward test is a tensile/compression test of a sheet strip.

The specimen is clamped in a specimen holder that is used to prevent buckling of the strip during the test. The holder has a peek hole that is used for measurements

of the strains. The specimen is painted with a randomized dot pattern, which is used for the measurements of strains through Digital Image Correlation (DIC) camera. A reinforced Teflon film is put between the specimen and the holder in order to eliminate the influence of friction forces. The silicon pieces are used to prevent the specimen to buckle between the specimen holding texture and the chucks.

Figure 57 shows the experimental test equipment used during the tension/compression test.



Figure 57: Schematic of test equipment during the Tension-Compression test (on the left) and test samples (on the right)

Two sets of experiments were performed in this study, in which the specimen was loaded up to 2.5% in tension, and then reloaded to the corresponding strain levels in compression. One entire cycle and two whole cycles were analysed.

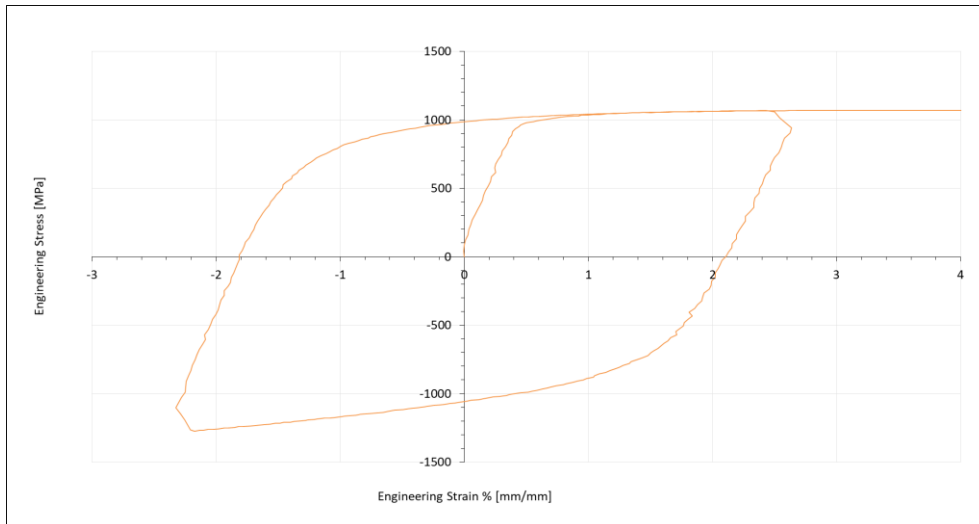


Figure 58: One entire cycle based on the 2.5% tension/compression test – DP1000, 1.2 mm thickness.

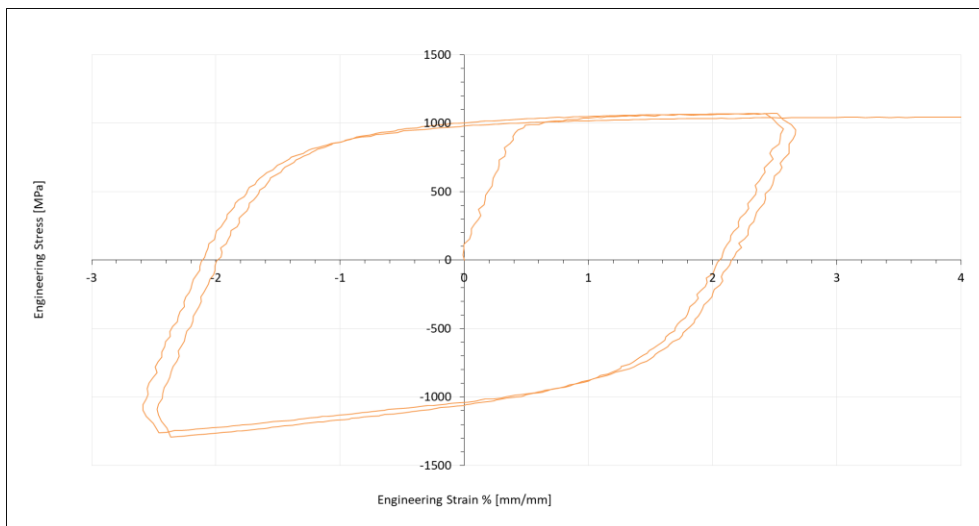


Figure 59: Two whole cycles based on the 2.5 % tension/compression test – DP1000, 1.2 mm thickness.

Further two sets of experiments were carried out in this study, in which the specimen was loaded up to 5.5% and, 6.5% in tension respectively, and then reloaded until the residual strain level reached 1% roughly in tension.

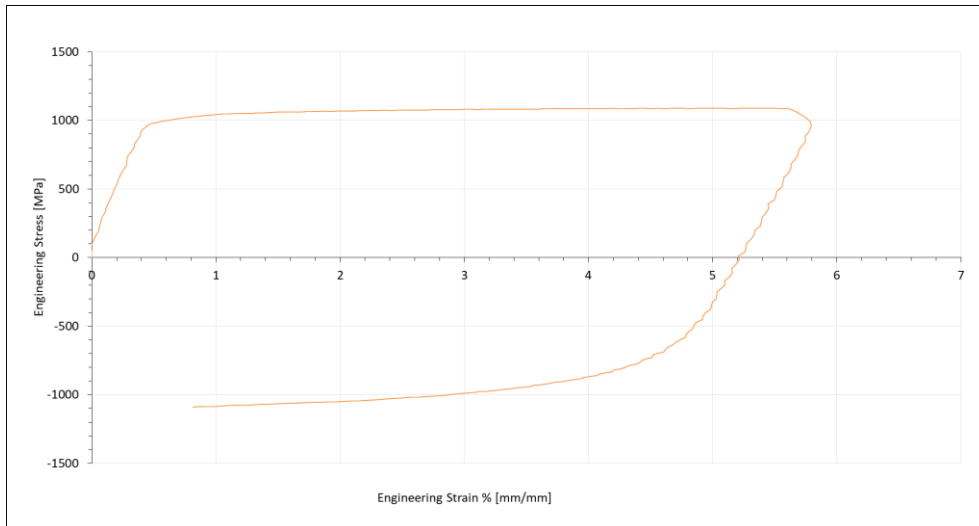


Figure 60: One half cycle based on the 5.5% tension/compression test.

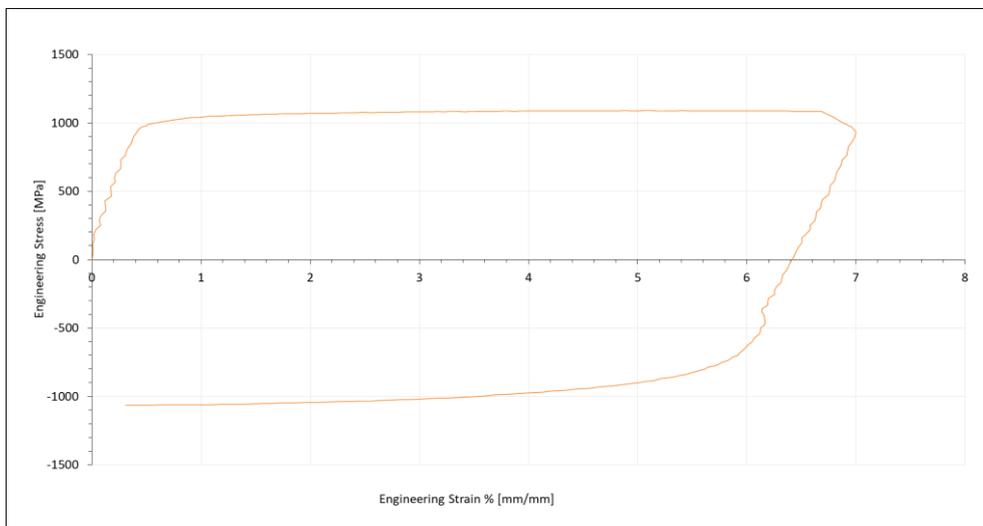


Figure 61: One half cycle based on the 6.5% tension/compression test.

## **CHAPTER 6:**

### **EXPERIMENTAL ACTIVITY – FEA OF U-SHAPED BEND TEST ON DUAL PHASE 1000**

The usual practice is to simulate the forming operation using a Finite Element (FE) technique, then using the simulation result to modify the initial die design for springback compensation. The die is then manufactured, and the final modification of the tool geometry is performed through successive trials. These additional trials lead to an increase in development cost and time. For this reason, accurate springback prediction through FE simulation is necessary.

Materials models play an important role in simulating sheet metal stamping and springback. AHSS exhibit Bauschinger effect, transient behaviour, work hardening stagnation, and permanent softening when they are formed under reverse loading condition as already explained in Chapter 4. Therefore, the conventional isotropic hardening model may not accurately predict such phenomena. Regarding the material model, parameters which significantly affect the springback are:

1. Flow stress data, which relates the stress state of each element in the formed part to its strain value.
2. E-modulus, which determines the proportion of elastic and plastic deformation and amount of elastic recovery.
3. Hardening rule, which represents complex behaviours of material such as

Bauschinger effect, transient behaviour, work hardening stagnation, and permanent softening.

In this study paper, the evaluation of the springback in AHSS is carried out through the U-shaped bend test because it is the simplest and the easiest to quantify springback parameters such as sidewall curl.

## 6.1 CAD Design by CATIA V5

The U-shaped Bend test consists in applying a certain displacement in the punch, bending the specimen until the cross section shows a U-shaped geometry. A schematic of this test and a representation of the U-shaped geometry is shown in Figure 62. After this test, the sheet will exhibit springback, and as previously mentioned, stronger DP steels tend to have higher springback effects. This test also allows to study the influence of stamping parameters in springback, such as blank holder load, punch radius, etc.

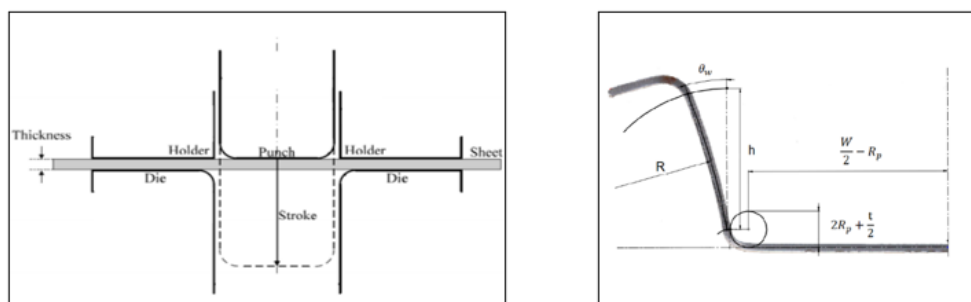


Figure 62: Schematic of a U-shaped bend test and measurement methodology for springback quantification

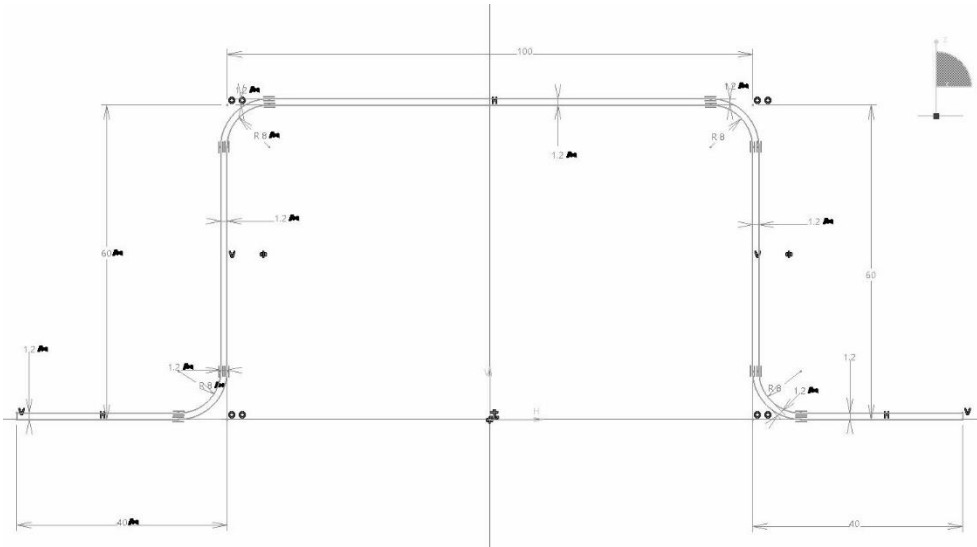


Figure 63: U-shaped geometry details

After the forming process ends, the next step is springback evaluation. To quantify springback, a path line is considered. One section cut will be applied per the corresponding path line. Afterward, along this section cut, “before springback” and “after springback” states will be plotted. Thus, the actual displacement difference between them will be investigated.

The evaluation of springback will be developed under different point of views:

1. First, we evaluate the simulation results, and we compare it with the actual measured values of springback after the stamping process. This analysis highlights the results differences caused by simulating the stamping operation with a proper material characterization and different yield models. Furthermore, the effects of Young’s modulus degradation is evaluated. Figure 64 shows the simple U-shaped geometry used to conduct the evaluation.

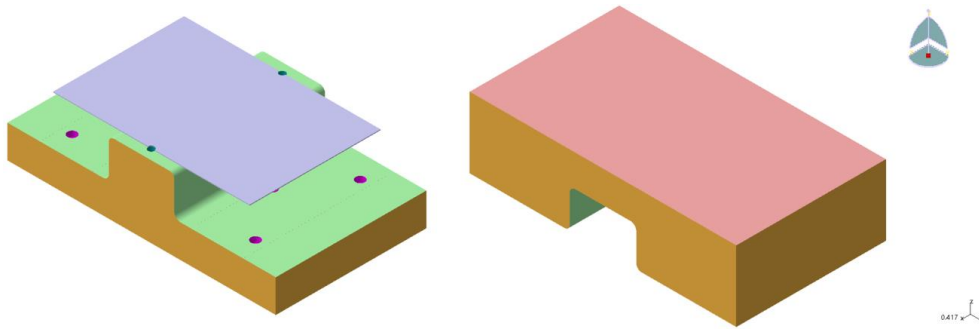


Figure 64: Schematic of the punch, die, and the sheet metal blanket.

2. Secondly, the paper evaluates how to reduce springback phenomenon by applying practical techniques such as forming with the implementation of lock beads at the end of the punch stroke, Figure 65 and Figure 66.

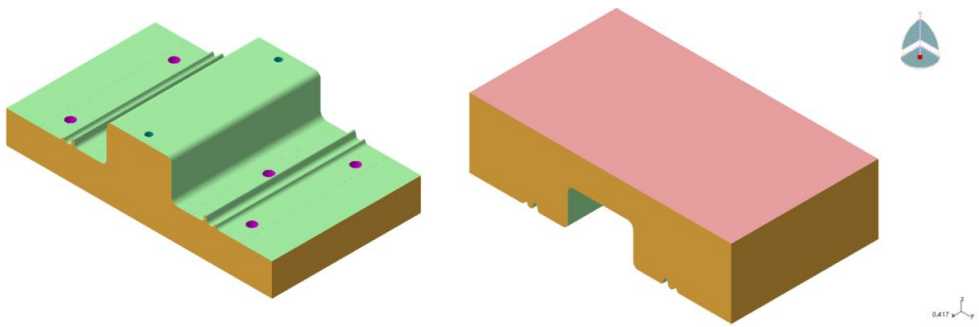


Figure 65: Schematic of the punch, die with the presence of lock beads.

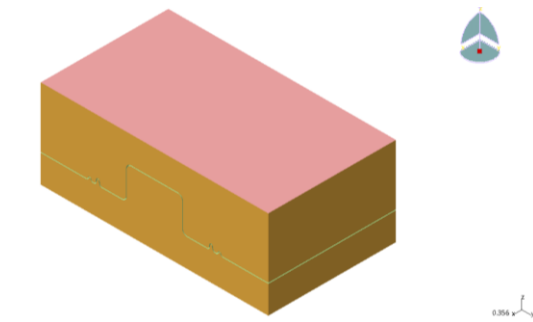


Figure 66: Schematic of the complete stamp for case analysis n.2

## 6.2 Simulation Setup and Evaluation of Forming Process

The U-drawing test is performed using a 400-ton servo press. The machine offers 4 000 000 N of press force. When the material is released from the die, characteristic springback occurs. Figure 67 shows a schematic representation of the U-drawing test set-up used in this study.

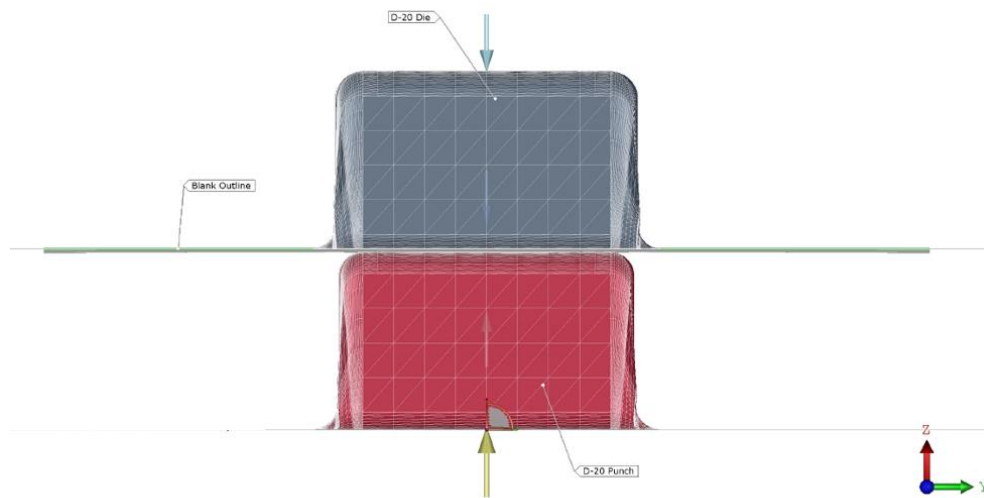


Figure 67: U-drawing test schematic

During the test, a strip of DP1000 (blank element) 375 mm long and 200 mm wide with thickness 1.2 mm was backed at the top of the punch and the die (radius of 8 mm and opening of 102.4 mm) then drawn on the punch (radius of 8 mm and opening of 100 mm). Details of the test set-up are shown in Table 13.

Punch Wide (mm)	Punch Radius (mm)	Die Radius (mm)	Die Wide (mm)	Blank Length (mm x mm)	Stroke (mm)
100	8	8	102.4	300x200	60

Table 13: Parameters of the U-drawing experimental test.

3-D FE simulation of the U-channel drawing process was developed using the AutoForm software package. A preliminary evaluation by using the FE simulation

was carried out to understand which forming operation is better between deep drawing without blank holder and deep drawing with blank holder.

No blank holder was chosen to continue the investigation since the simulation results by using the blank holder have shown greater springback angles with respect to the crash forming without blank holder.

Indeed, in case of using the blank holder, the sidewall curl angle reaches 15 mm of normal deviation from reference geometry, whereas in case of simple crash forming without blank holder, the sidewall curl angle reaches 8 mm roughly, Figure 68.

### BBC Yield Surface Results with Blank Holder and without Blank holder

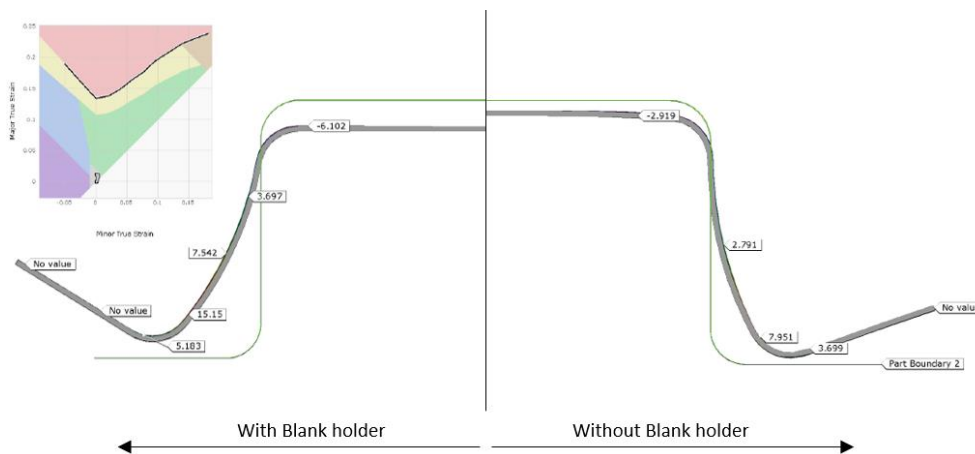


Figure 68: Simulation of springback, deep drawing with blank holder – BBC Yield Surface

### 6.3 Simulation Results of Different Constitutive Models

The material card was filled with the results from experimental tests (uniaxial tensile test, tension/compression test, Nakazima test). The Swift/Hockett-Sherby model has been used for the approximation of the hardening curve in addition to the tensile/compression curves that were added for considering the Bauschinger

effect. Also, kinematic hardening model was used to simulate the effect of transient softening and work hardening stagnation. Two additional parameters known as transient softening rate ( $K$ ) and stagnation ratio ( $\xi$ ) were added to the material model. As far as concern the yield surface, different models will be analysed using the FE simulations. Data obtained from the Nakazima test represents the forming limit curve of the material for the reference thickness of 0.8 mm. Figure 69 summarizes the material card of Dual Phase 1000 DP, sheet thickness 1.2 mm.

No blank holder was used during the simulation process.

For each figure is displayed the forming limit diagram on the upper left corner. It is important to understand that the insufficient stretch is the cause for having high values of springback in the sidewall region. To eliminate the springback defects on the side of the part, the state of stress should pass from insufficient stretch to safe forming region. This latest state of stress is reached by implementing lock beads at the end of the punch stroke (post stretching operation). Chapter 6.5 will explain this analysis in detail.

The resulting U-shaped samples after stamping operation were measured at the workshop by using a coordinate-measuring machine to obtain the final post-springback profile. The measured contact points on the surface of the part are displayed in the following charts with blue dots.

Material Card Editor for HCT980X (Dual Phase 1000, Sheet thickness 1.2 mm)

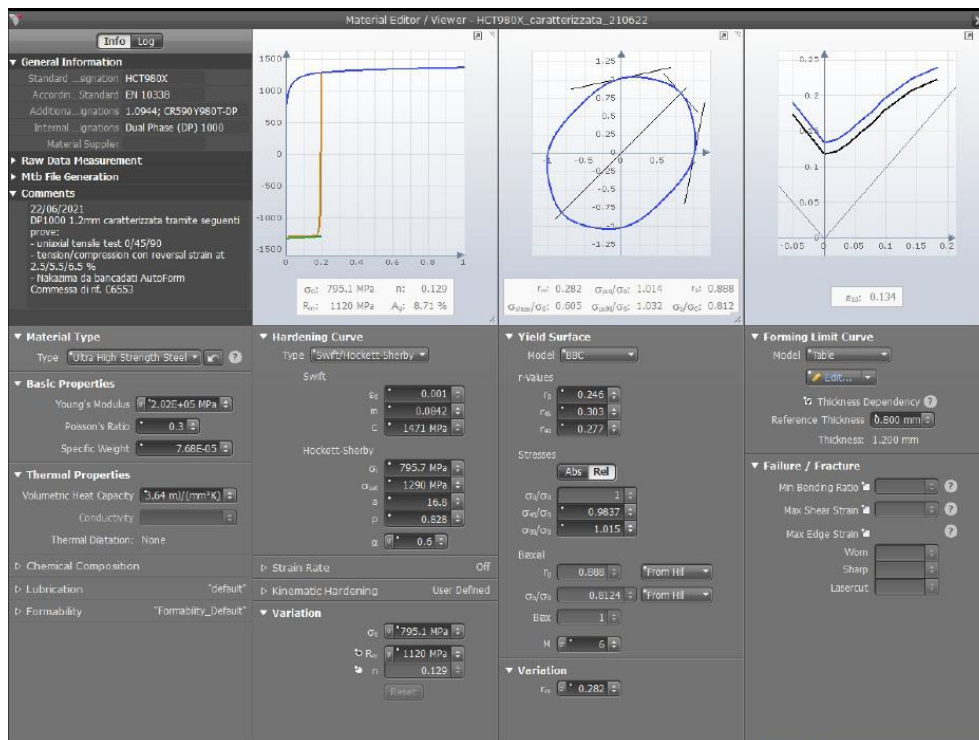


Figure 69: Material card generation DP1000, BBC Yield Surface

The following charts will display the results from the evaluation of the different Yield surface constitutive models:

- a) BBC (2005) Model
- b) Barlat and Lian Yield Model
- c) Quadratic Hill Yield Model
- d) Vegter Model

## BBC Yield Surface Model Results

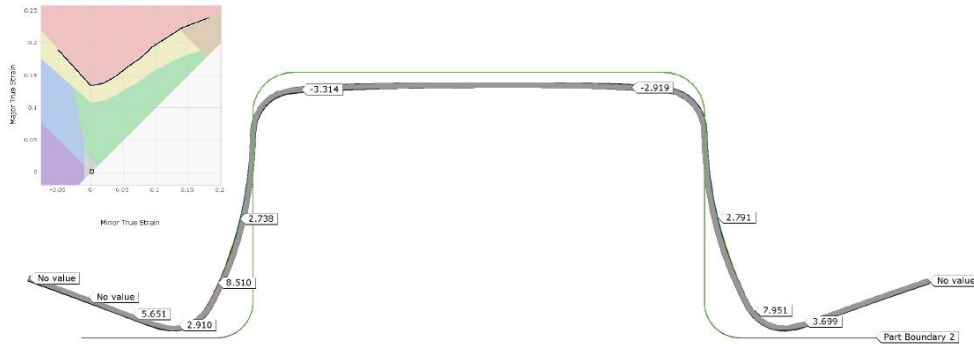


Figure 70: Simulation of springback, drawing without blank holder – BBC Yield Surface. Comparison between nominal geometry and predicted results

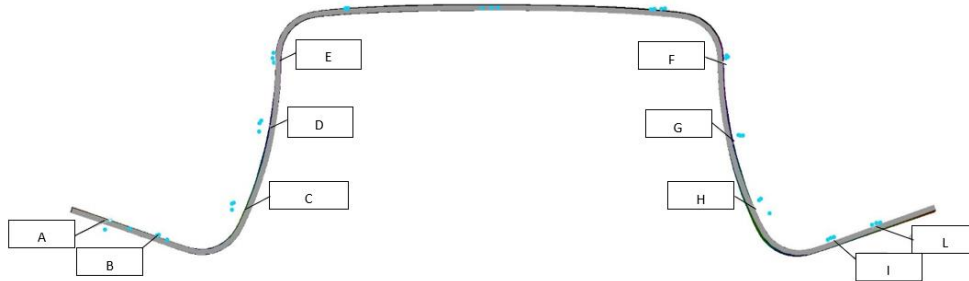


Figure 71: Schematic of comparison between actual springback measured points (blue dots) and simulated springback prediction, BBC Model

Point	Springback predicted by simulation (mm)	Actual springback measured on the part (mm)	Deviation
A	8.94	10.76	1.82
B	5.96	7.35	1.39
C	8.14	9.28	1.14
D	2.51	4.07	1.56
E	0.43	0.94	0.51
F	0.29	1.03	0.74
G	2.69	4.13	1.44
H	7.51	10.44	2.93
I	5.03	7.71	2.68
L	9.05	10.87	1.82

Table 14: Results of comparison between actual springback measured points and simulated springback prediction, BBC Model

## Barlat Yield Surface Model Result

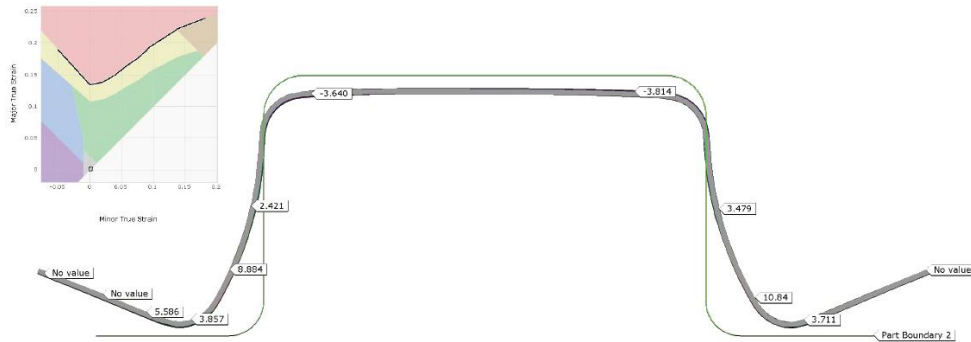


Figure 72: Simulation of springback, drawing without blank holder – Barlat Yield Surface. Comparison between nominal geometry and predicted results

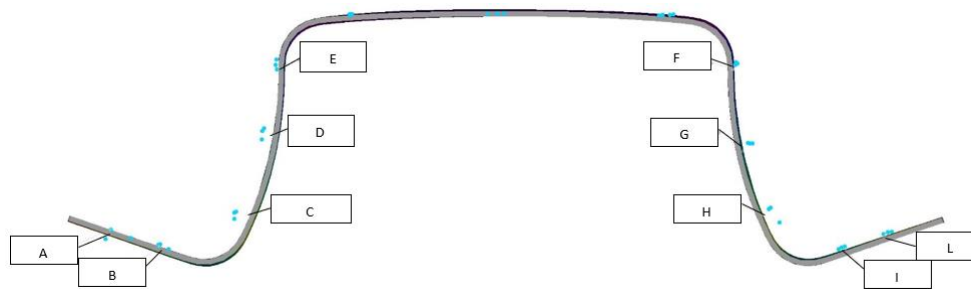


Figure 73: Schematic of comparison between actual springback measured points (blue dots) and simulated springback prediction, Barlat Model

Point	Springback predicted by simulation (mm)	Actual springback measured on the part (mm)	Deviation
A	9.05	10.76	1.71
B	7.09	7.35	0.26
C	8.06	9.28	1.22
D	1.28	4.07	2.79
E	0.31	0.94	0.63
F	0.32	1.03	0.71
G	2.40	4.13	1.73
H	8.09	10.44	2.35
I	4.96	7.71	2.75
L	8.81	10.87	2.06

Table 15: Results of comparison between actual springback measured points and simulated springback prediction, Barlat Model

## Hill Yield Surface Model Results

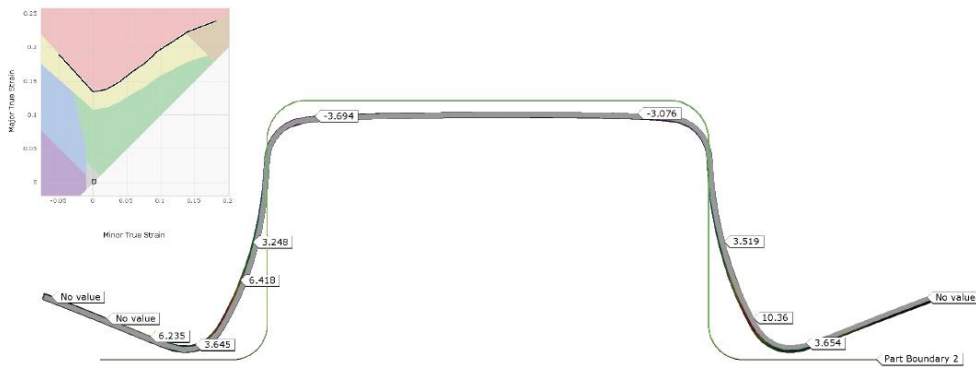


Figure 74: Simulation of springback, drawing without blank holder – Hill Yield Surface. Comparison between nominal geometry and predicted results

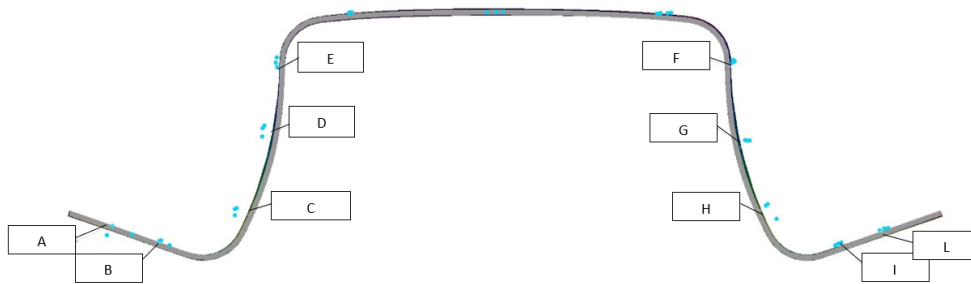


Figure 75: Schematic of comparison between actual springback measured points (blue dots) and simulated springback prediction, Hill Model

Point	Springback predicted by simulation (mm)	Actual springback measured on the part (mm)	Deviation
A	9.31	10.76	1.45
B	6.28	7.35	1.07
C	8.58	9.28	0.7
D	1.56	4.07	2.51
E	0.38	0.94	0.56
F	0.34	1.03	0.69
G	2.75	4.13	1.38
H	7.60	10.44	2.84
I	5.20	7.71	2.51
L	9.24	10.87	1.63

Table 16: Results of comparison between actual springback measured points and simulated springback prediction, Hill Model

## Vegter 2017 Yield Surface Model Results

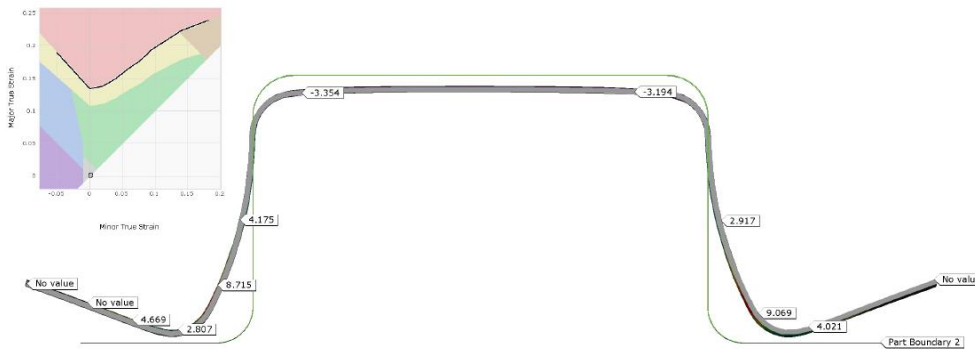


Figure 76: Simulation of springback, drawing without blank holder – Vegter 2017 Yield Surface. Comparison between nominal geometry and predicted results

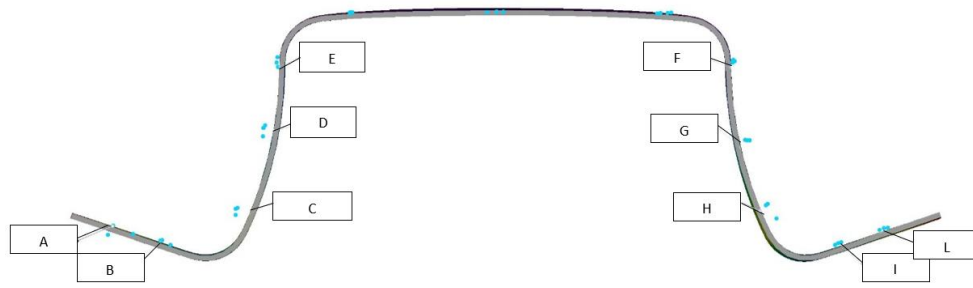


Figure 77: Schematic of comparison between actual springback measured points (blue dots) and simulated springback prediction, Vegter Model

Point	Springback predicted by simulation (mm)	Actual springback measured on the part (mm)	Deviation
A	8.90	10.76	1.86
B	6.00	7.35	1.35
C	8.17	9.28	1.11
D	1.45	4.07	2.62
E	0.42	0.94	0.52
F	0.25	1.03	0.78
G	2.56	4.13	1.57
H	7.28	10.44	3.16
I	5.00	7.71	2.71
L	8.92	10.87	1.95

Table 17: Results of comparison between actual springback measured points and simulated springback prediction, Vegter Model

The FE simulation results very well show the high tendency of the sheet material, DP 1000 with sheet thickness 1.2 mm, to show springback defects in the sidewall region. Indeed, for each simulation that evaluates the different yield surface model, sidewall curl defect ranges from 8 mm up to 10 mm of normal deviation from reference geometry.

Furthermore, no marked difference is visible between the different Yield surface constitutive models. However, it is worth to note that FE simulation results underestimate the actual springback defects which is present at the sidewall of the real U-shaped stamped sample.

## 6.4 Simulation Results considering Young's Modulus Reduction.

In this study, the effect of Young's modulus degradation is carried out. I.e., the reduction of the unloading elastic modulus with plastic strain can be determined through the loading-unloading tensile test. Yoshida et al. (2002) suggested to use and average  $E$ -modulus,  $E_{av}$ . They introduced the following equation to express the variation of  $E$ -modulus with plastic strain:

$$E_{av} = E_0 - (E_0 - E_a) \left[ 1 - e^{-\xi \epsilon_0^P} \right]$$

Two FE simulations are conducted: in the first simulation the average E-modulus ( $E_{av}$ ) is set up to simulate the U-shaped bend test, and in the second simulation Virgin E-modulus is set up to make a comparison and understand the influence of the elastic modulus.

**Average Young's Modulus, (DP1000,  $E_{av} = 191743 \text{ MPa}$ )**

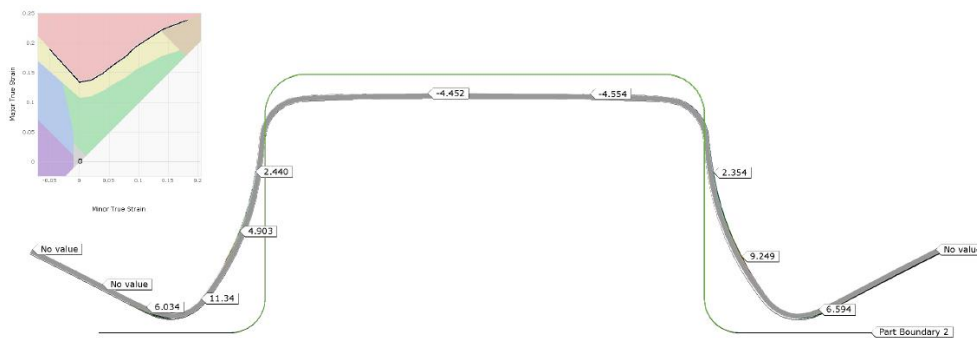


Figure 78: Simulation of springback, deep drawing without blank holder. Influence of average Young's modulus. Comparison between nominal geometry and predicted results



Figure 79: Schematic of comparison between actual springback measured points (blue dots) and simulated springback prediction, Average Young's Modulus

Point	Springback predicted by simulation (mm)	Actual springback measured on the part (mm)	Deviation
A	10.26	10.76	0.5
B	5.82	7.35	1.53
C	9.50	9.28	-0.22
D	1.97	4.07	2.1
E	0.40	0.94	0.54
F	0.59	1.03	0.44
G	3.12	4.13	1.01
H	8.27	10.44	2.17
I	5.74	7.71	1.97
L	10.27	10.87	0.6

Table 18: Results of comparison between actual springback measured points and simulated springback prediction, Average Young's Modulus

### Virgin Young's Modulus, (DP1000, E=202000 MPa)

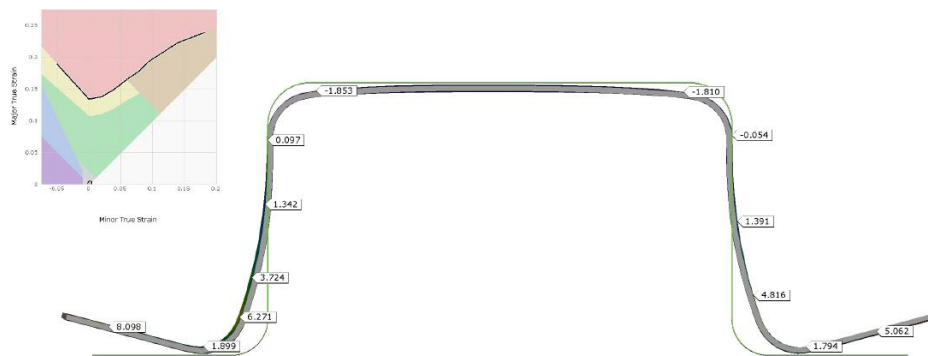


Figure 80: Simulation of springback, drawing without blank holder. Virgin Young's modulus. Comparison between nominal geometry and predicted results.

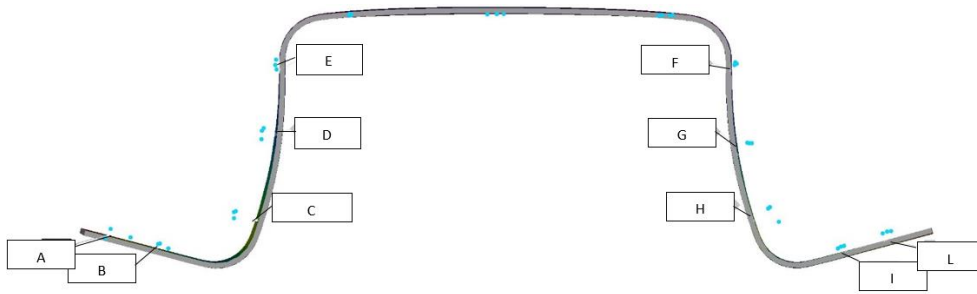


Figure 81: Schematic of comparison between actual springback measured points (blue dots) and simulated springback prediction, Virgin Young's Modulus

Point	Springback predicted by simulation (mm)	Actual springback measured on the part (mm)	Deviation
A	7.56	10.76	3.2
B	5.02	7.35	2.33
C	5.54	9.28	3.74
D	1.33	4.07	2.74
E	0.09	0.94	0.85
F	0.07	1.03	0.96
G	1.39	4.13	2.74
H	5.69	10.44	4.75
I	4.30	7.71	3.41
L	6.61	10.87	4.26

Table 19: Results of comparison between actual springback measured points and simulated springback prediction, Virgin Young's Modulus

As it can be seen from the results of the two FE simulations, the use of an Average Young's modulus better approximate what really happens in real stamping operation. The deviation between the predicted springback and the actual measured is lower in the first case. This can be explained because in general, by increasing the punch stroke the apparent E-modulus decreases and reaches a saturation value. The reduction of Young's modulus by increasing the punch stroke is due to increase of plastic strain. Hence, by using an average E-modulus which takes in consideration the plastic strain instead of using a constant virgin elastic modulus is beneficial and gives more reliable results.

## **6.5 Simulation Results with Post Stretching Method (Lock Beads)**

Regarding control and reduction of springback, in general, there are two practical ways (36).

1. Obtain the final part within geometric tolerances after compensating for springback by altering the geometry of tooling.
2. Applying additional stretch/tension forces to the part during the forming operation (post stretch method).

The first way: tooling geometry compensation is based on simulated prediction of springback as well as trial and error.

The second way: for the post stretch method, the sheet material undergoes extra stretching toward the end of forming process. This extra tension reduces the heterogeneous distribution of stresses through the sheet thickness at the wall area and consequently reduces springback and residual stresses.

### **Reversal Loading in Sheet Metal Forming Processes**

In a typical sheet metal forming process a considerable amount of material undergoes non-proportional loading. Passing over a tool radius the material is subjected to the multiple bending-unbending, which means reverse tension-compression loading over the sheet thickness. Figure 82 shows the stress distribution and the Bauschinger effect responsible for the change of mechanical properties during a non-proportional loading.

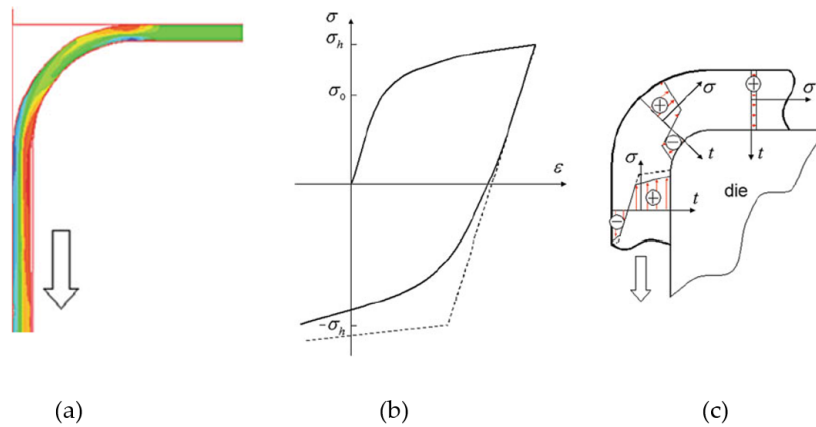


Figure 82: (a) reversal tension/compression loading (red for the tension stress) during passing over a tool radius, arrow shows the direction of drawing. (b) schematic of the Bauschinger effect and (c) Bauschinger influence on the stress evolution during passing over a die radius.

First, material hardens in tension to the stress  $\sigma_h$  and then loaded in compression to  $-\sigma_h$ . Plastic deformation occurs before negative yield strength (dashed line presents material behaviour without the Bauschinger effect). Similar reversal stress-strain history occurs when material passes over a die radius. During the first bending there is a tension on the outer side of a sheet and a compression inside. During the second unbending the stress state over the sheets thickness reverses and is influenced directly by the Bauschinger effect.

### Post Stretching Method

The post stretching method has demonstrated improvements in reducing springback.

There are two methods:

1. Post stretching with Servo Hydraulic Cushion (SHC).
2. Post stretching with ending lock beads.

For completeness here is explained the post stretching with servo hydraulic cushion even though there was no chance to perform the test because of the non-availability of the variable blank holder force of the press at the mechanical workshop of the firm.

### Servo Hydraulic Cushion

The sidewall curl is significantly reduced with the variable blank holder force. On the contrary constant BHF (Blank Holder Force) shows very poor results in springback prevention. Thanks to the variable BHF, the compression stresses on the wall, which are created because of unbending of the sheet material when it passes the die corner radius, are converted to tension stresses. By applying the additional stretch force, first the elastic deformation happens in those elements which were in compression stress state leading them to reduced compression state or even at plastic tension state; then plastic deformation happens in those elements which were in tension stress state leading them to increased plastic tension state.

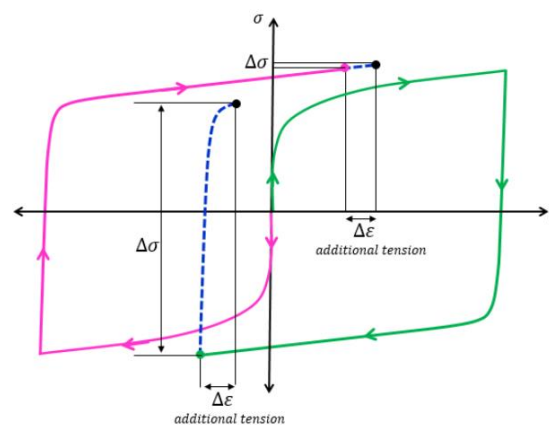


Figure 83: Stress state of elements which undergo reverse loading condition when they pass the die corner radius and enter the die cavity.

Results showed that the residual stresses through the sheet thickness at the wall are significantly reduced by applying post stretching with SHC because it provides the capability to control the BHF through the die stroke. Therefore, it allows accurately controlling and increasing the BHF toward the end of deformation and significantly reducing springback. By applying the post stretching method, the additional tension force converts the tension-compression stress distribution to only tension which cause reduction of springback. Although the result of this strategy shows that by using a SHC it is possible to apply the post stretching method and significantly reduce the springback, some limitation should be considered when this technique is applied in real stamping operation of large 3D components because a significantly large force is required. Therefore, this limitation can reduce the practicality of this method in real stamping operation.

### **Single Lock Bead**

The other conventional method for post stretching is to design the tools (die and punch) with lock beads which can be activated towards the end of the deformation. In this method there is no need for SHC. However, it is not that easy to lock the draw-in of strong materials such as AHSS and the lock beads need to be designed with sharp edges and fillet radii. Therefore, design of the lock bead adds more complexity to tool design and sometimes failure of the material at the lock bead area is difficult issue to solve. Indeed, also in our case study, at the end of the punch stroke, out of shape material fails due to sharp edges and fillet radii. However, this

is not a big issue since material fails in the are out of shape designed. Laser trim is necessary at the following stage to delimit the designed part.

### Simulation Results of Post Stretch Method with Single Lock Bead

Figure 84 shows the post-stretching using locking-type beads approaching the end of the stroke (2 mm to the end of the stroke). It is worth to note the stress state diagram on the upper left corner which explain that most of the material is undergoing safe forming state (green region), only very marginal part is under compression state (blue region) and insufficient stretch (grey region). A very small region of the material is subjected to excess of thinning (yellow region). This state of stress is originated by the implementation of the lock beads. Without them, insufficient stretch state will result for the whole part causing very large springback angles at the sidewall (as previously seen).

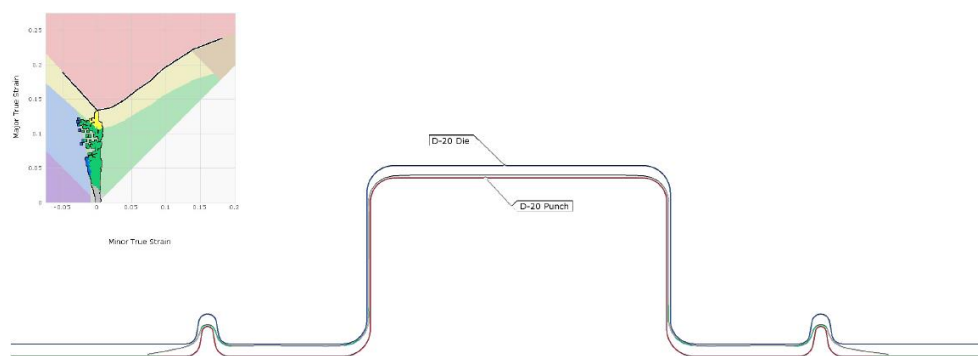


Figure 84: Schematic of post-stretching using locking-type beads approaching the end of the stroke (2 mm to the end of the stroke), no blank holder used.

Figure 85 shows the end of the forming process when the die was removed from the punch and the sheet is completely released experiencing springback and residual stresses.

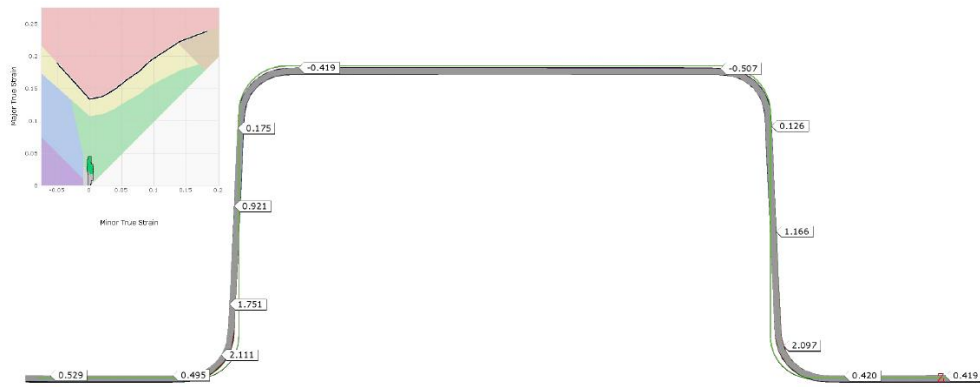


Figure 85: End of the forming process. Springback evaluation with post stretch method, one single lock bead.

This method was observed to provide a stretch of 2% which is effective in reducing the springback. In fact, sidewall curl is at a maximum of 2 mm of normal deviation from reference geometry. A significantly decrement with respect to the case of stamping without ending lock beads (springback defect of 15 mm).

Hence, the alternative way to generate post-stretching through the whole thickness of the part is by designing the die and the punch with very sharp edges and fillet radii (lock beads).

### **Mechanism of Work**

Lock beads work in such a way that the beads penetrate in the part towards the end of the forming stroke which causes locking of the material, restricting its flow and thereby generating a stretch force in the side wall of the part. This additional stretch or tensile force reduces the heterogeneous stress distribution in the part and consequently the unbending moment is reduced leading to a reduced springback.

Lock beads should not be confused with the drawbeads which are engaged

throughout the forming stroke and allow controlled flow of the material.

Figure 86 shows a schematic depicting the different stages in the forming of a hat-shaped part. The initial position (A) represents the tool setup at the start of the deformation. The upper die moves down, drawing and bending the material until a point when the bead starts to touch the material (B). As the die continues to move downwards, the material forms around the bead (C) which increasingly restricts the material flow and provides a stretch force in the side wall. Position (D) indicates the end of the forming operation.

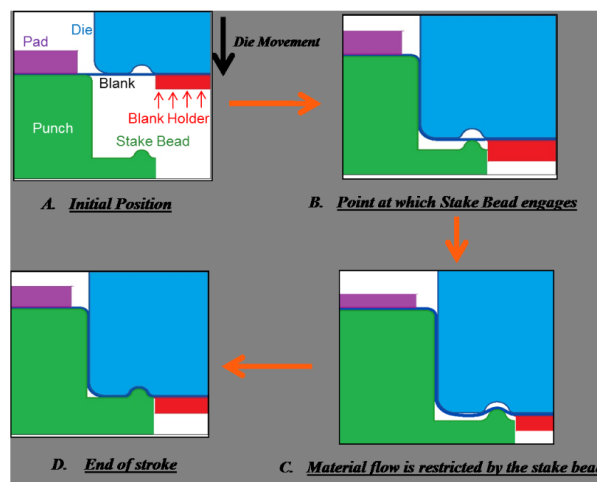


Figure 86: schematic showing different stages in hat-bending when stake bead is used.

### Double Lock Beads

After having proved the beneficial effect of using lock beads at the end of the punch stroke during the forming process to reduce springback defects in the sidewall region of the part, it worth time to study and investigate the geometry of the lock beads in further reducing springback in AHSS.

Different bead design and geometries could be considered for the analysis. In our study it is evaluated the effectiveness of using two circular beads designed by different size of height.

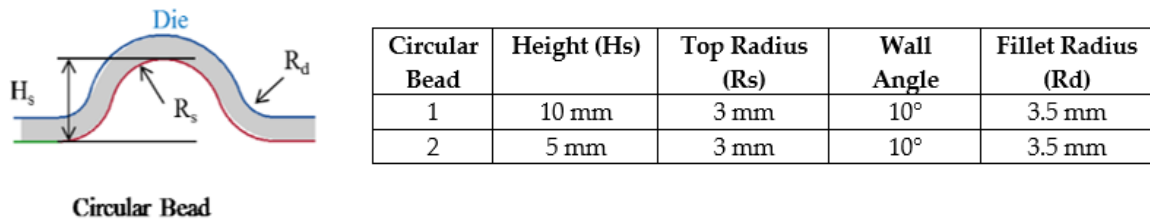


Figure 87: Circular bead geometry with relative dimensions

Figure 87 illustrates the parameters in detail. The stake bead radius ( $R_s$ ), the die groove radius ( $R_d$ ), and the bead penetration ( $H_s$ ) are the significant dimensions that determine the “locking” capacity of the bead design.

For the lock bead concept to be successful, the die needs to be designed so that:

- a) The stake bead will not break or wear out easily and should be within the manufacturing capabilities.
- b) Stretching of the material in the bead itself does not cause local fracture in the material.
- c) The stake bead design provides adequate stretch force in the side wall to reduce springback.

Thus, a careful analysis and evaluation must be carried out at the design stage of the lock beads.

## Simulation Results (Two lock beads investigation)

Figure 88 shows the post-stretching using two locking-type beads with different size of height approaching the end of the stroke (8 mm to the end of the stroke). The stress state diagram, on the upper left corner, points out that a region of the part is in failure (red area). This is caused by the implementation of the double lock beads. However, the highlighted red area in the forming limit diagram engages a delimited region around the beads of the part. By design those areas are out of shape and the following trim step will cut them getting a sample free from cracks, areas with risks of split and defects.

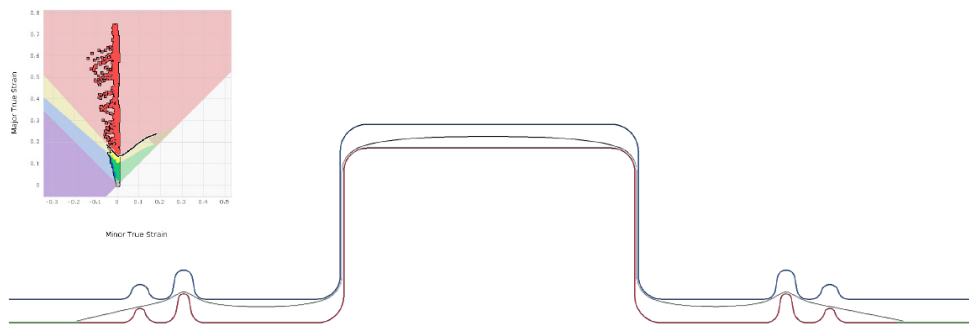


Figure 88: Schematic of post-stretching using two locking-type beads with different size of height approaching the end of the stroke (8 mm to the end of the stroke).

Figure 89 shows the end of the forming process when the die was removed from the punch and the sheet is completely released experiencing springback and residual stresses. As it can be seen from the forming limit diagram, the whole part is in safe forming region (green area).

Results of the springback simulation put in evidence the effectiveness of design correctly two lock beads and the improvement reached in terms of springback

angles on the sidewall region with the latest method in comparison with respect to the simulation performed with only one lock bead.

Sidewall curl angles further decreased and reached values below 2 mm normal deviation from reference geometry.

It is worth to note how good is the approximation of the simulation results with the experimental points measured on the surface of the part in the laboratory. By using the correct characterization of the material properties, with the data obtained from the experimental tests (tensile test, tension-compression test, average elastic modulus) and hence enabling the kinematic hardening which capture the characteristic behaviours as Bauschinger effect and transient softening, every yield surface model (in this case was used BBC 2005) provides good simulation results of springback that very accurately describe the real stamping operation.



Figure 89: End of the forming process. Springback evaluation with post stretch method, Double lock beads

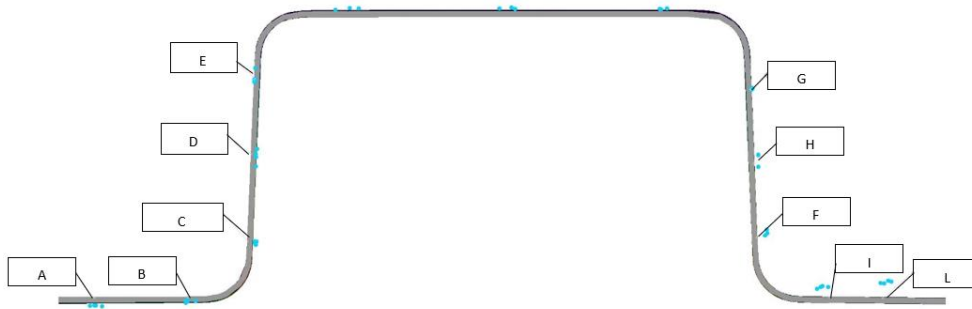


Figure 90: Schematic of comparison between actual springback measured points (blue dots) and simulated springback prediction, Double lock beads

Point	Springback predicted by simulation (mm)	Actual springback measured on the part (mm)	Deviation
A	0.22	-1.39	-1.61
B	0.37	-0.47	-0.84
C	1.64	-0.13	-1.77
D	0.81	-0.16	-0.97
E	0.02	0.09	0.07
F	0.14	0.39	0.25
G	0.90	1.73	0.83
H	1.56	3.38	1.82
I	0.38	2.43	2.05
L	0.26	3.5	3.24

Table 20: Results of comparison between actual springback measured points and simulated springback prediction, Double lock beads

Figure 91 and Figure 92 show the pictures of the two samples stamped with different methodology. Figure 91 highlights the sidewall of the part pointing out the large difference in springback defect.

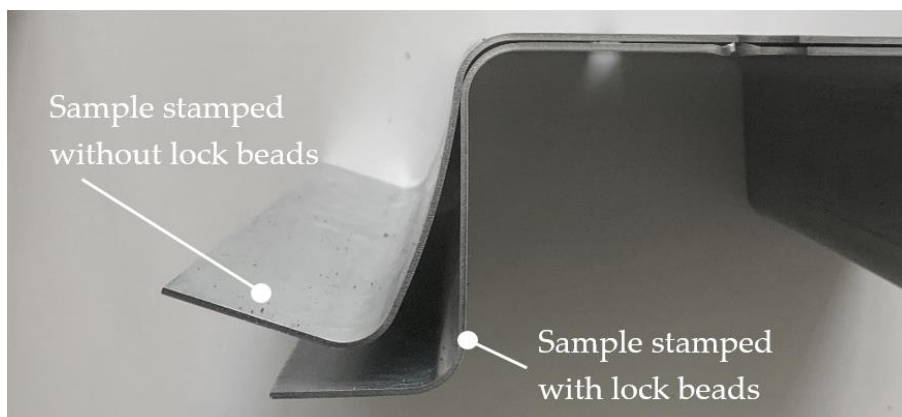


Figure 91: Picture of the stamped samples: to the top the sample stamped without lock beads, to the bottom the sample stamped with double lock beads



Figure 92: Picture of the stamped samples: to the top the sample stamped without lock beads, to the bottom the sample stamped with double lock beads

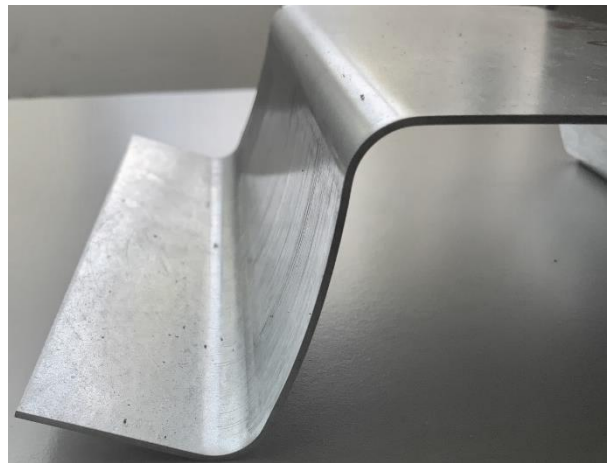


Figure 93: Picture depicting the sidewall of the stamped part without lock beads, very large springback defect



Figure 94: Picture depicting the sidewall of the stamped part with lock beads, almost null springback defect

## CHAPTER 7:

### CASE STUDY OF A JOB ORDER IN DUAL PHASE 1000

The aim of this chapter is to prove that the precautions studied and evaluated throughout the thesis have a reliable application in a case study of a job order and provide positive results in solving the issue of the springback in AHSS.

The case study is carried out by using AutoForm integrated solver. The assembly configuration consists of the rigid forming tools (punch and die) and a deformable blank, as shown in Figures 95.

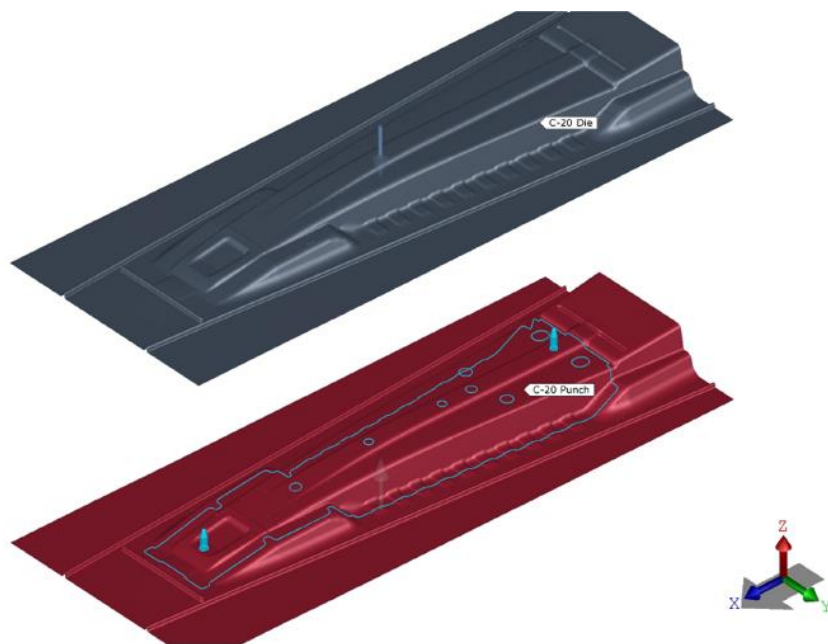


Figure 95: Geometrical assembly configuration of the forming process. In red is displayed the punch, in grey is displayed the die and the blue line delimitates the designed part to be stamped.

The part is designed in Dual Phase 1000 with sheet thickness 1.2 mm. The required geometry from a AHSS such as Dual Phase 1000 is complex and the sidewall of the part sizes almost 60 mm in height.

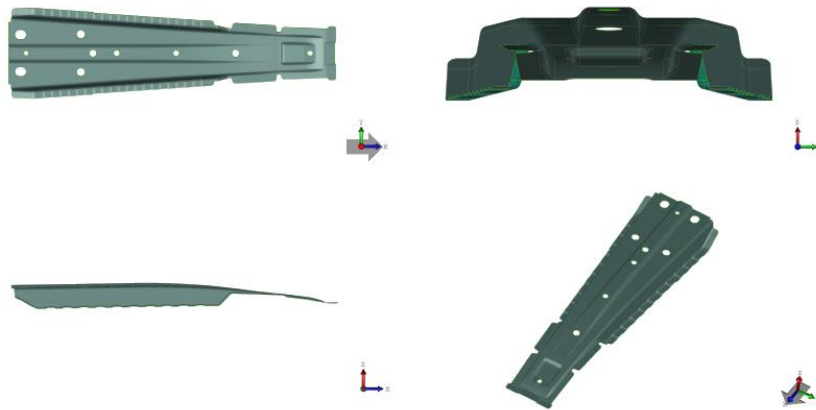


Figure 96: Drawing views of the designed part to be stamped.

To obtain this part two stamping operations are needed. Only the first drawing presents the implementation of the lock beads. The blank specimen is leaned on the punch and the die moves downwards approaching the punch and bending the sheet until the end of the stroke. The first forming operation presents larger die radius and details on the punch which allow a smooth process without the occurrence of any crack or failure. Subsequently, the tools are removed, the part is released, and it is free from any external load. The trim operation can get the pre-geometry of the part delimitating the out of shape (lock beads area). Afterwards, the second stamping operation with the designed radii and removed the details on the punch can get the nominal geometry. As before, the pre-formed part is leaned on the punch and the die is approaching closing the stamp. At the end of the process, the specimen is unloaded and released, and the geometry of the metal specimen is investigated before and after springback.

## 7.1 Simulation Forming Process

The following images show the forming process from the start to the end of the stroke in different steps. It is displayed the formability that explain the stress state of the material during the working process. Green areas represent safe forming state, grey areas mean insufficient stretch, blue areas mean compression state, purple areas mean thickening due to excessive compression, yellow areas mean risk of split, orange areas mean excess of thinning and red areas mean failure of material.

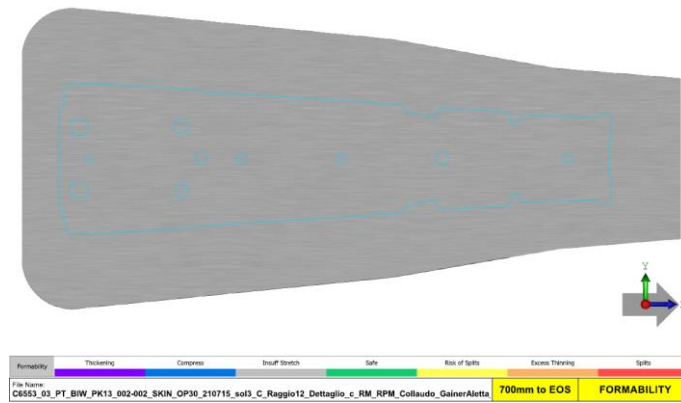


Figure 97: First Crash Forming, 700 mm to the End Of Stroke

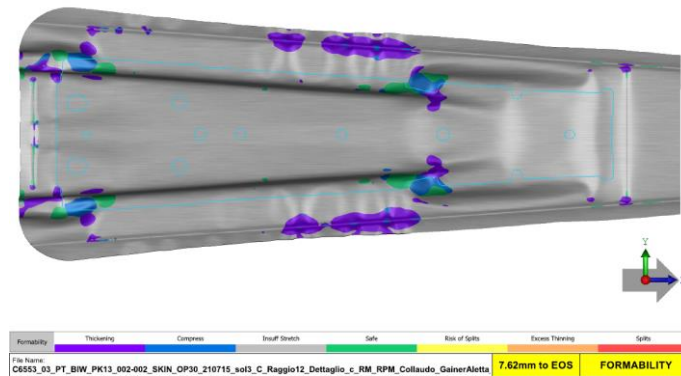


Figure 98: First Crash Forming, 7.62 mm to the End Of Stroke

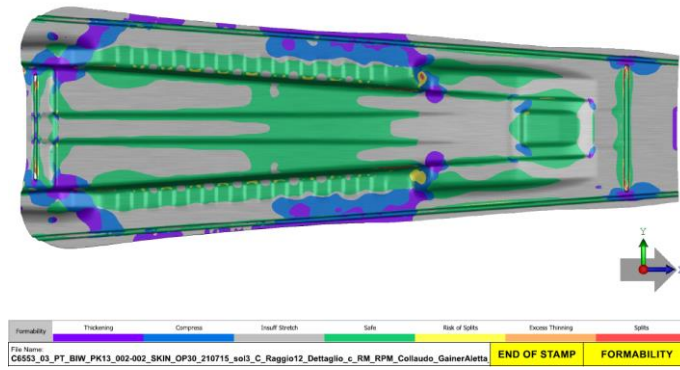


Figure 99: First Crash Forming, End Of Stroke

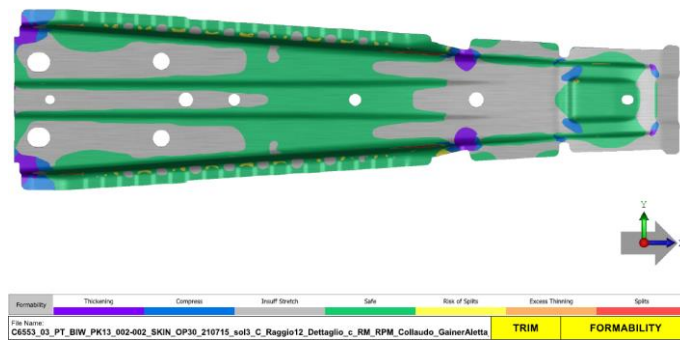


Figure 100: Trim Operation

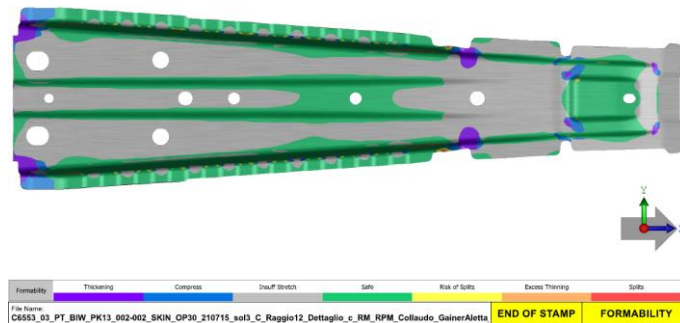


Figure 101: Second Crash Forming, End of Stroke

## 7.2 Analysis Results

### HARDENING STRESS - Evaluation after springback

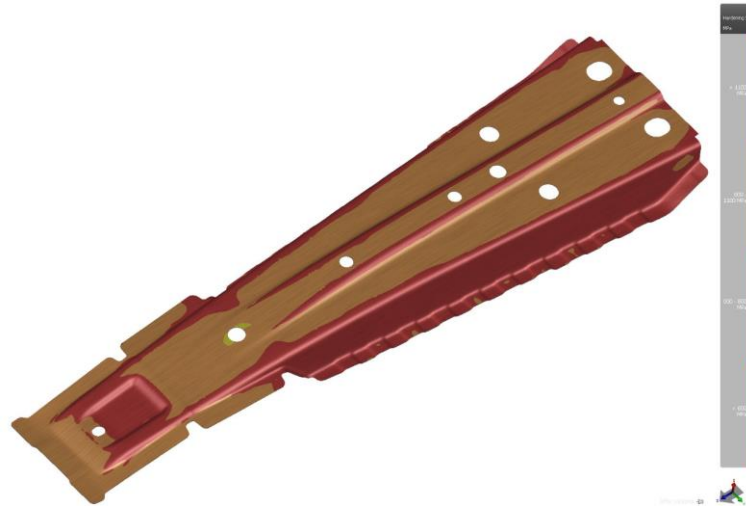


Figure 102: Hardening Stress plot after springback

To begin with, the first step in evaluating the results contains the effective stresses of the model after springback. By looking into Figure 102, the maximum effective stress is 1300 MPa and it is reached in the side area. This is higher than the material Ultimate Tensile Strength (UTS), which is 1120 MPa, which means that there are possibilities of necking or even crack failures. However, it is worth to note that stamping operation is not a uniaxial deformation, thus a straight comparison with UTS from tensile test could be misleading. Furthermore, orange areas and red areas mean hardening stress greater than 800 MPa which is the yield point, thus the whole part is undergoing plastic strain.

## PLASTIC STRAIN - Evaluation after springback

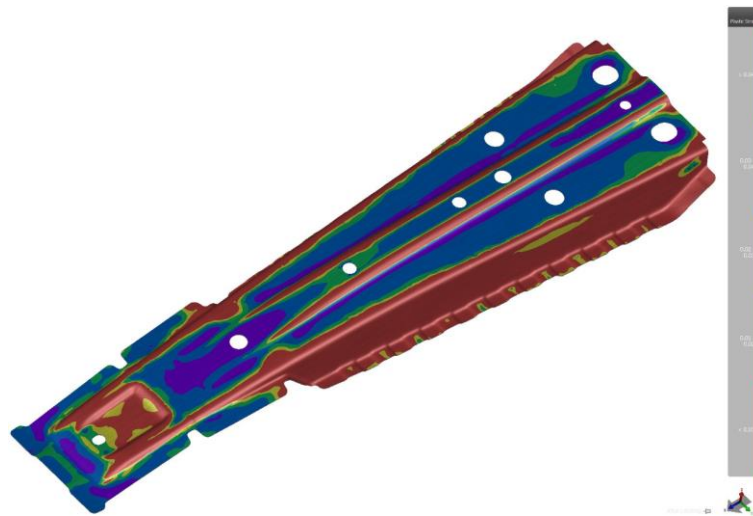


Figure 103: Plastic Strain plot after springback

After having evaluated the effective stresses of the part, one should proceed in investigating the plastic strain. Conventionally, a minimum 3% of plastic strain should be reached. However, it is very difficult to obtain such requirement for the whole geometry of the part.

As observed in Figure 103, a maximum plastic strain of 4% is reached mostly in proximity of the side area where the largest hardening stress occurred. Considering that the main problem to obtain this part is the springback on the sidewall, it is sufficient to guarantee 4% plastic strain in the critical region which is the sidewall.

## MAX FAILURE - Evaluation after springback

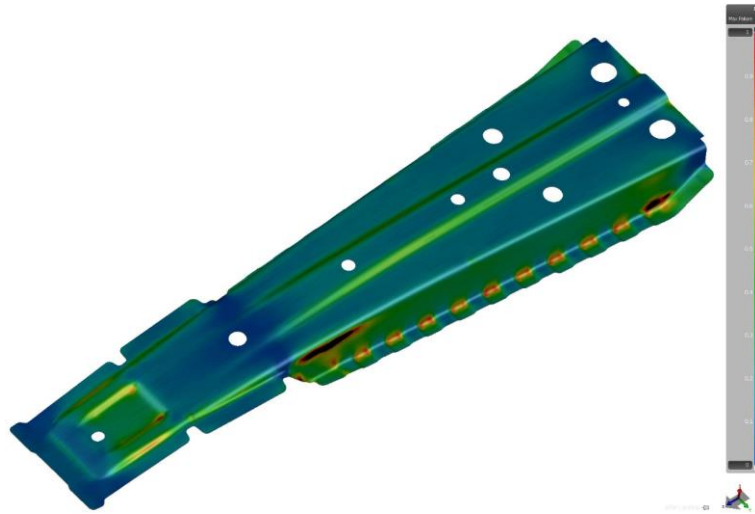


Figure 104: Max Failure Plot

By considering the Max Failure plot, one can immediately notice the critical areas for potential excessive thinning, porosity, or cracks (black areas where max failure is greater than 1).

To evaluate the material failure of the blank, one should also refer to the thickness reduction plot as well as to the Forming Limit Diagram (FLD)/ Strain distribution diagram. Through all of them, a good estimation can be made regarding the load that the specimen can withstand until some cracks appear.

In fact, by looking at the thickness reduction plot, one can observe that the thinning is within a range of 0.1 (meaning thickening 10%) and -0.25 (meaning thinning 25%).

## THINNING - Evaluation after springback

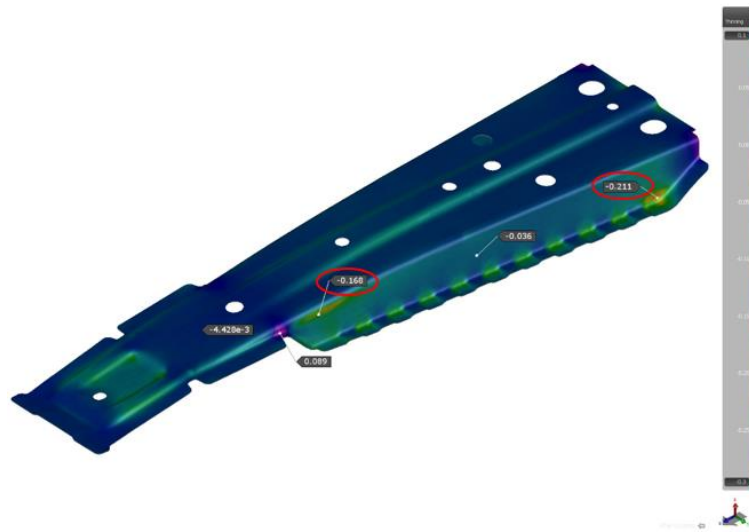


Figure 105: Thinning Plot

The material thinning of 17% and 21% in the highlighted areas could be that high to provoke cracks on the metal workpiece. To confirm that this prediction is correct, the FLD plot, as well as the formability map should be studied.

By looking at formability map, Figure 105, one can get an idea about the amount of thickness reduction the material can withstand before any cracks occur. As can be observed from the map, there is indication for cracks (risk of split) in the already previous warned areas where the hardening stress plot and the max failure plot pointed out. However, the part is undergoing safe formability for most of the regions of the part. Such results seem to be good enough.

## FORMABILITY - Evaluation after springback

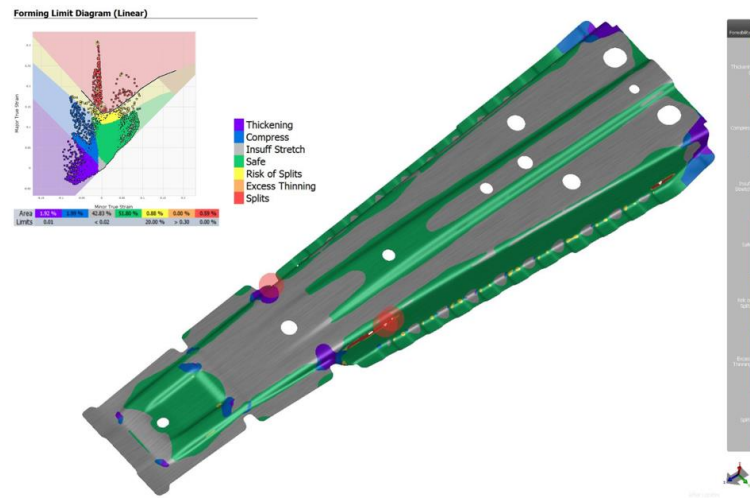


Figure 106: Formability plot

Apart from the thinning, important to notice is also the thickening of some regions of the specimen. There are low wrinkled areas. If one checks again the thickness reduction plot, it can be confirmed that the wrinkles occur where thickening is indicated, as depicted in both formability and FLD plots.

## SPRINGBACK PREDICTION - Evaluation after springback

After the forming process finishes, the next step is the springback evaluation. To quantify springback, three path lines are considered since the geometry of the part is quite long. One section cut will be applied per corresponding path line. Along these section cuts, “nominal geometry” and “after springback” states will be plotted. Furthermore, a comparison with the results obtained when the part was simulated without ending lock beads is carried out to be proved the effectiveness of this technique.

### *Section 1*

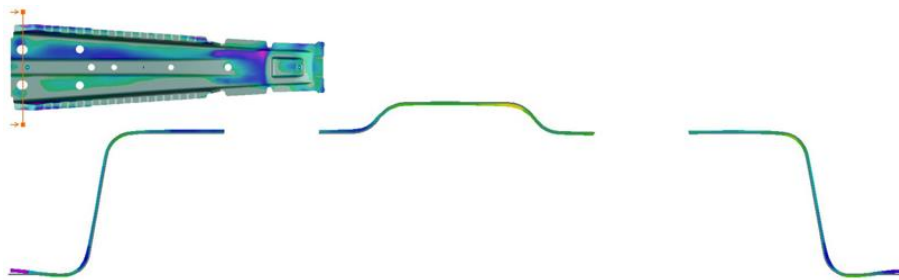


Figure 107: Simulation of the stamping operation with the implementation of ending lock beads

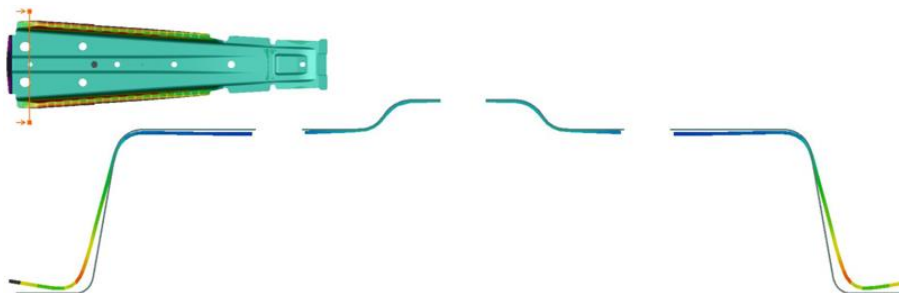


Figure 108: Simulation of the stamping operation without the implementation of the lock beads

## Section 2

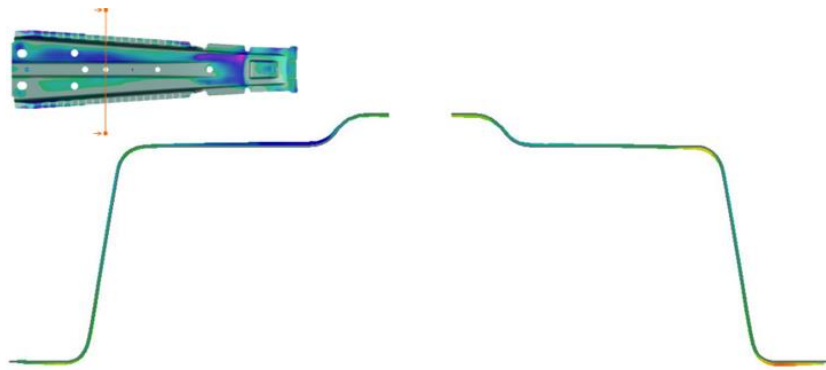


Figure 109: Simulation of the stamping operation with the implementation of ending lock beads



Figure 110: Simulation of the stamping operation without the implementation of the lock beads

## Section 3



Figure 111: Simulation of the stamping operation with the implementation of ending lock beads



Figure 112: Simulation of the stamping operation without the implementation of the lock beads

To start with the section 1, looking into Figure 107 and Figure 108, one can observe the geometry change of the specimen after unloading when the part is released and

springback occur. It is evident that the stamping operation with lock beads is almost perfect and no needs of any adjustment while the forming process without this technique requires further trials to adjust the die radius and manual hammering in the mechanical workshop in order to bring the sidewall under acceptable tolerance.

To give some springback values, in section 2 – case with LB, normal deviation from reference geometry (springback in mm) is about 1.67 mm. While in section 2 – case without LB, normal deviation is about 5.46 mm.

# References

1. (n.d.). Gau, J. T., and Kinzel, G. L. 2001. "A new model for springback prediction in which the Bauschinger effect is considered". International Journal of Mechanical Sciences.
10. (n.d.). AS/P 2009. "Advanced high strength steel (AHSS) application guidelines Version 4.1." The World Steel Association.
11. (n.d.). S. Mohtar, N. Baluch, C S Abdullah, 2015. "AHSS auto stamping challenges: Rectifying springback".
12. (n.d.). S Keeler, M Kimchi, P J Mooney, 2017. "Advanced High-Strength Steels Application Guidelines Version 6.0".
13. (n.d.). R. Kuziak, R. Kawalla, and S. Waengler, 2008. "Advanced high strength steels for automotive industry", Arch. Civ. Mech. Eng., vol. 8, no. 2.
14. (n.d.). J. Ha, J. Lee, J. H. Kim, M.-G. Lee, and F. Barlat, 2017. "Investigation of plastic strain rate under strain path changes in dual-phase steel using microstructure-based modeling", Int. J. Plast., vol. 93.
15. (n.d.). P. Tsipouridis, 2006. "Mechanical properties of Dual-Phase steels", Doctoral Dissertation, Technischen Universitat Munchen.
16. (n.d.). E. Billur and T. Altan, 2010. "Challenges in Forming Advanced High Strength Steels".
17. (n.d.). G. R. Speich, V. A. Demarest, and R. L. Miller, 1981. "Formation of Austenite During Intercritical Annealing of Dual-Phase Steels", Metall. Mater. Trans. A, vol. 12, no. 8.
18. (n.d.). H. Kim, C. Kim, F. Barlat, E. Pavlina, and M.-G. Lee, 2013. "Nonlinear elastic behaviors of low and high strength steels in unloading and reloading", Mater. Sci. Eng. A, vol. 562.
19. (n.d.). Lems W, 1963. "The change of Young's modulus after deformational low temperature and its recovery", Ph.D. Dissertation, Delft.
2. (n.d.). Geng, L. M., Shen, Y., and Wagoner, R. H. 2002. "Anisotropic hardening equations derived from reverse-bend testing". International Journal of Plasticity.
20. (n.d.). Hamad ul Hassan et al. 2015. "Springback prediction and reduction in deep drawing under influence of unloading modulus degradation".
21. (n.d.). Gutscher, G., Wu, H.C., Ngaile, G., Altan, T., 2004. "Determination of Flow Stress for Sheet Metal Forming Using the Viscous Pressure Bulge (VPB) Test". Journal of Materials Processing Technology.
22. (n.d.). Sigvant, M., Mattiasson, K., Vegter, H., Thilderkvist, P., 2009. "A viscous pressure bulge test for the determination of a plastic hardening curve and equibiaxial material data". International journal of Material forming.
23. (n.d.). J. Rodrigues, Tecnologia mecânica, 2005. Tecnologia da deformação plástica. Escolar Editora.
24. (n.d.). AutoForm Customers <https://www.autoform.com/en/company/customers/>.

25. (n.d.). A. Dwi Anggono and W. Adi Siswanto, 2014. "Finite Element Simulation of Deep Drawing of Steel Steel - Aluminum Tailor - Welded Blanks," presented at the 1st Conf. on Eng. Tech. and Ind. Application, Surakarta, Indonesia.
26. (n.d.). X. Gu, 2008. "Development and implementation of adaptive mesh refinement methods for numerical simulations of metal forming and machining", Ph.D. dissertation, Von der Fakultät Maschinenbau der Technischen Universität Dortmund.
27. (n.d.). Tisza, M. and Z.P. Kovács, 2012 "New methods for predicting the formability of sheet metals" *Journal of Production Processes and Systems*.
28. (n.d.). Kevin Nilsson 2019, "Material modeling in Sheet Metal Forming Simulations".
29. (n.d.). Kelly, 2012. *Solid Mechanics Part II: Engineering Solid Mechanics - small strain. Solid mechanics lecture notes*, University of Auckland. .
3. (n.d.). Yoshida, F., and Uemori, T. 2003. "A model of large-strain cyclic plasticity and its application to springback simulation". *International Journal of Mechanical Sciences*.
30. (n.d.). Krieg, R.D., 1975. "A practical two surface plasticity theory". *Journal of Applied Mechanics*.
31. (n.d.). Jiang, Y., Sehitoglu, H., 1996. "Modeling of cyclic ratchetting plasticity". Part I: Development of constitutive relations. *Journal of Applied Mechanics* .
32. (n.d.). Yoshida, F., Uemori, T., Fujiwara, K., 2002. "Elastic-plastic behavior of steel sheets under in plane cyclic tension-compression at large strain". *International journal of plasticity*.
33. (n.d.). Frederick, C.O., Armstrong, P.J., 2007. "A mathematical representation of the multiaxial Bauschinger effect". *Materials at High Temperatures*.
34. (n.d.). F. Barlat and K. Lian, 1989 "Plastic behavior and stretchability of sheet metals. Part I: A yield function for orthotropic sheets under plane stress conditions", *Int. J. Plast.*, vol. 5, no. 1.
35. (n.d.). Y. Granbom, 2010 "Structure and mechanical properties of dual phase steels An experimental and theoretical analysis", KTH, Stockholm.
36. (n.d.). Wagoner, R.H., Lim, H., Lee, M.G., 2013. *Advanced issues in springback. International journal of plasticity*.
37. (n.d.). R. Hill, *Proc. Roy. Sci. Lond.*, A193 (1948) 281, London.
38. (n.d.). R. Hill, *Theoretical plasticity of textured aggregates. Mathematical Proceedings of Cambridge Philosophical Society*.
4. (n.d.). F. Morestin and M. Boivin, 1996. "On the necessity of taking into account the variation in the Young modulus with plastic strain in elastic-plastic software", *Nuclear Engineering and Design*.
5. (n.d.). Demeri, M., 2013. "Advanced high-strength steels: science, technology, and applications".
6. (n.d.). N. Kardes, O.H. Mete, Y. Demiralp, C. Choi, T. Altan. "Springback Prediction in Bending of AHSS - DP780", submitted NAMCR 2012.

7. (n.d.). ACS REDDY, C BHASKAR REDDY and D V PALESWAR, "Review on Different Hardening Models for Computation of Deep Drawing Process Simulation".
8. (n.d.). Pourboghrat, F., Chu, E., 1995. "Springback in plane strain stretch/draw sheet forming. Int. J. Mech. Sci. 36.
9. (n.d.). Ali Fallahiarezoodar, 2018. "Prediction and Reduction of Defects in Sheet Metal Forming".